Development of a remotely-controlled electric vehicle with characterization of the ground grip

Marco Cecotti (2013)

Removed appendix - published paper

OXFORD BROOKES UNIVERSITY

Faculty of Technology, Design & Environment

Department of Mechanical Engineering and
Mathematical Sciences

Development of a Remotely-Controlled Electric Vehicle with Characterization of the Ground Grip

Marco Cecotti

A thesis submitted for the degree of *Doctor of Philosophy*

August 2013

Abstract

This thesis focuses on traction control techniques for electric vehicles with independently driven wheels. The aim is to maximise the grip of each wheel with the ground, improving the performance as well as the stability of the whole vehicle. Hence the estimation of the friction characteristic between tyres and ground is addressed. Accurate estimation is required not only to control the wheels at their best working condition, but also to predict their behaviour for future manoeuvres. This information could be used to calculate the braking distance or to evaluate the maximum attainable speed during cornering. A detailed knowledge of the friction characteristic would substantially improve the functionality of anti-lock braking system (ABS), anti-slip regulation (ASR), electronic stability control (ESC) and adaptive cruise control (ACC).

Estimation of ground characteristics and traction control for electric vehicles have been studied before, although previous research generally relies on driving manoeuvres at the limit of adhesion to obtain meaningful information about the maximum grip offered by the ground. This is not suitable during safe driving on public roads and the present thesis addresses the problem of constantly monitoring the road conditions, and forecasting the loss of adhesion instead of waiting for it. Furthermore, my approach is robust against external forces and can be applied to vehicles on tilted grounds. Hence my novel approach supersedes previous studies that assumed the vehicle on a flat surface, mostly neglecting the effects of rolling resistance and aerodynamic drag. I also propose a framework to take into consideration dynamic effects such as inertial forces and the distribution of the gravitational force. Taking these effects into account would lead to a more reliable estimation, particularly effective on steep or bumpy roads where adhesion loss is more likely to happen. Some of this work resulted in the publication of an IEEE conference paper.

My work belongs to a larger project aiming to develop an autonomous electric vehicle, whose main targets are economic and environmental sustainability. These targets led us to consider moving some of the computational requirements for the automatic guidance to a remote server, wirelessly communicating with the vehicle. Together with this investigation, original contributions of the project will include scene understanding solely based on stereo cameras and integration between the visual information and the vehicle dynamic response captured by the vehicle controller. My research is focused on this application, and a considerable amount of energy through my PhD went to the development of the system required to remotely control the vehicle. An extensive description of the development phase is included in this thesis.

Acknowledgements

I wish to thank various people for their contribution to this project. Most importantly my Director of Studies, Mr James Larminie, who inspired me with his passion for electric vehicles. He led me through some difficult times with the project, helping me to remain calm and focused on the problems I was facing. He understood whenever I deviated from my main objective in order to follow my interests and passions, but never forgot to remind me about the final aim of my study. He provided me with some invaluable feedback about my thesis and gave me the motivation to push it towards the end.

I would like to thank Prof. Khaled Hayatleh, who supported me both as a supervisor and a tutor. His contribution has been essential for my integration in Oxford Brookes University. He has always been the first one to consider our needs as research students and to offer support. I would like to give a special thank to Dr Neil Fellows, my second supervisor and the programme manager of the Intelligent Transport System Doctoral Training Programme. We both shared a great passion for the Intelligent Transport System project and he put his trust in me since the beginning. Together with Prof. Philip Torr, the programme director, they never missed a chance to acknowledge my contribution to the project. They allowed me to take charge of the project, often beyond my mere responsibility, granting me freedom over purchases and design decision. This opportunity greatly enriched my experience and made it worth every minute I dedicated to the project.

I am really grateful to all my supervisors, because they have always been friendly and honest with me, and never withheld useful advices.

I should not forget to thank my colleagues Mahesh and Sunando, for their frequent advice and the long conversations about the troubles of student life. Finally, I would like to acknowledge the moral support from my family and my friends, in particular dearest Kate and Nethra, who were always there when I needed them.

Table of Contents

List of Figures

List of Abbreviations

A_0 generic amplitude. 124–126

ABS Anti-lock Braking System. 1, 22, 26, 27, 33, 73, 111

ACC Adaptive Cruise Control. 1, 111

acc_x measurement of the accelerometer along the longitudinal direction of the vehicle. 73, 75, 76

acc_z measurement of the accelerometer along the vertical direction of the vehicle. 74, 75

α slip angle of the tyre. 44, 47, 52

ASR Anti-Slip Regulation. 1, 22, 26, 27, 111

a_z^w linear acceleration of the wheel along its z axis, referred to an inertial frame. 71, 72

BEV Battery Electric Vehicle. 17, 21–24, 26, 27, 33, 34, 38–40, 70, 73

CAN Controller Area Network. 85, 100, 101, 103, 107, 108

CG centre of gravity. 66

CompactRIO the device from National Instruments used on the quad bike to control all its functionalities. 83, 87, 97, 100, 103, 107, 159

$\Delta\theta$ error in the pitch angle. 75

e mathematical constant, also called Euler's number (≈ 2.71). 125

ESC Electronic Stability Control. 1, 22, 26, 27

η derivative of the longitudinal coefficient of friction over the slip ratio. 37, 38, 116, 119–123, 127–130, 132, 133, 136, 140–143, 145, 150, 153–155

F_d driving force of the vehicle, inclusive of any external force. 114

F_{ext} external forces applied to the body of the car in the longitudinal direction, including the effect of the gravitational force. 68, 76, 113, 114, 116–119, 122, 155

f_{ext} small signal of the external forces applied to the body of the car in the longitudinal direction. 118–122

FIFO First In First Out communication structure. 100–102

F_m total motive force applied to the wheel. 114, 116–120, 122, 155

f_m small signal of the total motive force applied to the wheel. 118–121, 123–130

FPGA Field-Programmable Gate Array. 8, 85, 90, 93, 94, 97, 98, 100, 101, 140, 154

FTP File Transfer Protocol. 100

F_w difference between the motive force applied to the wheel and the tractive force, representing the only force to produce the angular acceleration of the wheel. 114

F_X force applied by the vehicle along the X axis. 66–68, 113

F_X^{FL} force applied to the left front wheel along the X axis. 67

F_X^{FR} force applied to the right front wheel along the X axis. 67

F_X^{RL} force applied to the left rear wheel along the X axis. 67

F_X^{RR} force applied to the right rear wheel along the X axis. 67

F_x force applied by the ground to the tyre along the x axis. 24, 25, 44, 67, 113, 114, 116–120, 155

f_x small signal of the longitudinal tyre force. 118, 119

F_Y force applied by the vehicle along the Y axis. 66

F_y force applied by the ground to the tyre along the y axis. 44, 54

F_Z force applied by the vehicle along the Z axis. 66

f_z small signal of the force applied to the tyre along its z axis. 119

F_z^{FL} force applied to the ground at the contact point with the left front wheel along its z axis. 67

F_z^{FR} force applied to the ground at the contact point with the right front wheel along its z axis. 67

F_z^{RL} force applied to the ground at the contact point with the left rear wheel along its z axis. 67

F_z^{RR} force applied to the ground at the contact point with the right rear wheel along its z axis. 67

F_Z^{SU} force generated by the suspension unit along the Z axis. 71, 72

F_z force applied by the tyre to the ground along the z axis. 25, 44, 54, 59, 69–72, 114, 119–123, 127–130, 132, 133, 136, 140–143, 145, 150, 153–155

g gravitational acceleration ($\approx 9.8 m/s^2$). 71, 73, 74, 76, 128, 132

γ inclination angle of the tyre. 44, 50, 62

GPS Global Positioning System. 33

$G_p(s)$ transfer function between current and voltage in a continuous model of a DC motor, represented with Laplace transform. 95

$G_p(z)$ transfer function between current and voltage in the discrete model of a DC motor, represented with z-transform. 96

gyr_y measurement of the gyroscope around the lateral direction of the vehicle, basically the pitch of the vehicle. 75

h_{CG} height of the centre of gravity of the sprung mass, relatively to road plane. 69, 70

ICEV Internal Combustion Engine Vehicle. 21–23, 26, 30, 33, 34

IMU Inertial Measurement Unit. 20, 22, 34, 40, 65, 71–73, 76, 79, 87, 98

ITS Intelligent Transport System. 8, 17, 40, 65, 77, 79, 80, 108, 157, 159

I_y^w moment of inertia of the wheel around its y axis. 67, 68, 113, 114, 131

j imaginary unit. 121–123, 125, 127–130

k_1 gain of the transfer functions relater to the wheel speed. 123

ℓ wheelbase of the vehicle. 69, 70

L_a armature inductance of the motor. 95, 96

Λ_b slip ratio during braking. 24, 47

Λ_{FL} slip ratio of the left front wheel. 67

Λ_{FR} slip ratio of the right front wheel. 67

Λ_{RL} slip ratio of the left rear wheel. 67

Λ_{RR} slip ratio of the right rear wheel. 67

Λ_t slip ratio during traction. 24, 25, 36, 37, 47, 67, 114, 116–123, 127–130, 132, 133, 136, 140–143, 145, 150, 153–155, 158

λ_t small signal of slip ratio. 118–120, 130

LED Light-Emitting Diode. 87, 100

m mass of the vehicle or equivalent vehicle mass, in the "single wheel" model of the vehicle. 68–71, 112, 113, 115, 117, 119–123, 127–132

MOSFET Metal-Oxide-Semiconductor Field-Effect Transistor. 85, 87, 90, 91, 103

μ_{max} maximum friction coefficient between the tyre and the road. 59

μ_x longitudinal friction coefficient between the tyre and the road. 25, 36, 37, 67, 114, 116, 118–120, 128

μ_y lateral friction coefficient between the tyre and the road. 54

M_w moment of inertia of the wheel reported to the wheel radius. 114, 117, 119–124, 126–130

m^w mass of one wheel of the vehicle. 71, 72

N_s number of sampling periods (of the wheel speed) contained into one period of the oscillating signal of torque, which is used for the proposed estimation technique. 126

Ω angular velocity of the wheel. 45, 47, 67, 113, 114

ω angular frequency of a signal in the Fourier transform. 121–124, 127–130, 143

Ω_0 angular velocity of a non-sliding (free-rolling) wheel. 45, 47

ω_0 angular frequency of the oscillating signal of torque used for the proposed estimation. 124–126

Ω_{FL} angular velocity of the left front wheel. 68

Ω_{FR} angular velocity of the right front wheel. 68

Ω_{RL} angular velocity of the left rear wheel. 68

Ω_{RR} angular velocity of the right rear wheel. 68

p_1 dominant pole of the transfer functions among forces acting on the vehicle and the speed of the wheel and the speed of the vehicle. 123, 124, 126–128, 133, 136, 140, 142–145, 150

PCB Printed Circuit Board. 40, 81, 85, 103

PhD Philosophiae Doctor, in English "Doctor of Philosophy". 1, 17, 20, 79, 108, 157, 159

ϕ camber angle. 62

PI Proportional-Integral. 95, 96, 102

π mathematical constant, ratio between a circumference and its diameter ($\approx$ 3.14). 124, 125, 143–145, 150

p^{SU} extention of the suspension unit. 71, 72

PWM Pulse-Width Modulation. 85, 87, 90–95, 102, 103, 154

R_a armature resistance of the motor. 95, 96

R_e effective radius of a free-rolling tyre. 45, 47, 67, 68, 113, 114, 131

R_w undeflected wheel radius. 45

s longitudinal slip velocity. 47

SAE Society of Automotive Engineers. 43–45, 65

T torque provided to the wheel at the hub. 45, 113, 114

t time. 75, 121, 124–126

T_0 period of the oscillating signal of torque used for the proposed estimation technique. 125, 126

t_0 initial time. 75

TC Traction Control. 26–29

T_{FL} torque applied to the left front wheel. 68

T_{FR} torque applied to the right front wheel. 68

θ angle between the horizontal plane and the X axis of the vehicle. 73–76

θ_0 initial angle between the horizontal plane and the X axis of the vehicle. 74, 75

T_{PWM} period of the pulse-width modulation. 95, 96

T_{RL} torque applied to the left rear wheel. 68

T_{RR} torque applied to the right rear wheel. 68

T_s sampling period of the wheel speed. 126

UDP User Datagram Protocol. 98

V_v linear speed of the vehicle. 45, 47, 68–70, 73, 76, 113, 114, 116, 117

V_w angular speed of the wheel converted to its linear equivalent, by multiplying it to the effective radius. 114, 116–123, 127–130, 155

v_w small signal of angular speed of the wheel converted to its linear equivalent. 118–130

z_1 zero of the transfer functions relater to the wheel speed. 123, 124, 126–128, 133, 136, 140, 142–145, 150, 154

$ZOH(s)$ transfer function of a zero-order hold. 95

Chapter 1

Thesis Introduction

1.1 Intelligent Transport System Project

This PhD is funded by Oxford Brookes University and it is part of a wider Intelligent Transport Systems (ITS) project. The project aims to develop an autonomous vehicle, which should be safe as well as economically and environmentally sustainable (*Oxford Brookes ITS Website*). An important target for the project is to gain capabilities that are easily transferrable to the automotive industry. For this reason, the project was focused on a full-size vehicle, able to carry at least one passenger. The autonomous vehicle should be able to navigate and drive itself by identifying the road conditions, recognising road sign and obstacles (*Oxford Brookes ITS Website*). As various autonomous vehicles have already been developed around the world, to the point that several worldwide competitions have been organised (*DARPA Grand Challenge Website*), the aim of the whole project is not only to design a functional vehicle, but also to provide it with good dynamic performance and efficient operation.

With the intent of studying innovative techniques to improve the safety of the vehicle and to propose an environmentally friendly solution, the project was focused around a battery electric vehicle (BEV). These vehicles are emission free, as far as their usage is concern, and their general architecture allows for a precise control of the traction without the need for dedicated hardware (more on this in Section 1.2). In order to reduce the complexity and the cost of the vehicle, the project investigates the usage of a remote server to support the vehicle hardware in the computational effort required to provide autonomous guidance. The vehicle would be wirelessly connected with the server and it would support minimal autonomous functionality when disconnected from the server. This is needed to allow time for the driver to take over the control, or to safely bring the vehicle to a halt.

Six PhD students were assigned to the project, on different research areas. I was the first student to start the project and my responsibility was the development of the vehicle up to the stage of being completely controllable by a human from a remote computer. The overall task of the other students is to implement the transmission of the visual information from the cameras on the vehicle to the server and to automate the analysis of this visual information in order to plan the vehicle trajectory. The vehicle trajectory will be then

translated into commands for the vehicle. My research task was to obtain valuable information about the grip offered by the road during normal driving. This information is critical to calculate the most appropriate trajectories for the vehicle, as the longitudinal and the lateral accelerations are mainly limited by the grip with the ground. A block diagram of the overall dynamic control of the autonomous vehicle is shown in Figure 1.1.

Figure 1.1 shows that the inputs for the dynamic control of the vehicle are the set destination, the actual position and a map of the environment. The map of the environment is generated by computer vision algorithms, operating on the scene captured by the cameras installed on the vehicle. A vehicle-control trajectory-planning unit calculates the best trajectories to follow by using these inputs together with the information of vehicle speed, vehicle orientation and grip offered by the ground. The trajectories consist of a series of set points of linear and yaw acceleration for the vehicle, as well as some guidance about how to pursue these values. To clarify this, it is useful to understand the powertrain architecture of the vehicle, which includes two electric motors independently driving the two rear wheels. This architecture allows generating yaw moment in two possible ways: by providing the same torque to the two wheels and steering the front wheels, or by providing a differential torque to the two rear wheels while maintaining the front wheels aligned with the vehicle. Sometimes the environment requires the use of one solution instead of the other, for example when there is a step on the side of the vehicle which does not allow the steering of the front wheels, and this is the reason why the most appropriate control policy is provided by the vehicle-control trajectory-planning unit.

The planned vehicle trajectory is the input for the dynamic-control trajectory-planning unit, which calculates the torque that every actuator needs to generate in order to follow the trajectory as closely as possible. To do so, the unit also needs information about the speed of the wheels, the steering position, the acceleration of the vehicle, the normal force applied to the ground and the grip offered by the ground. The dynamic-control trajectory-planning unit implements techniques of longitudinal and lateral traction control by distributing the torque between the two rear wheels, by modulating the torque generated by each wheel and by varying the steering angle.

The set driving torque and the set steering torque are used to calculate the set currents for the traction motors and the steering motor. The set currents are compared to the actual currents flowing in the motors in order to calculate the voltages that need to be applied to the terminals of the motors. This is done by the driving-torque control unit and the steering-torque control unit. The applied voltages and the measured currents are used to estimate the speeds of the traction motors and, from them, the speeds of the two rear wheels, given

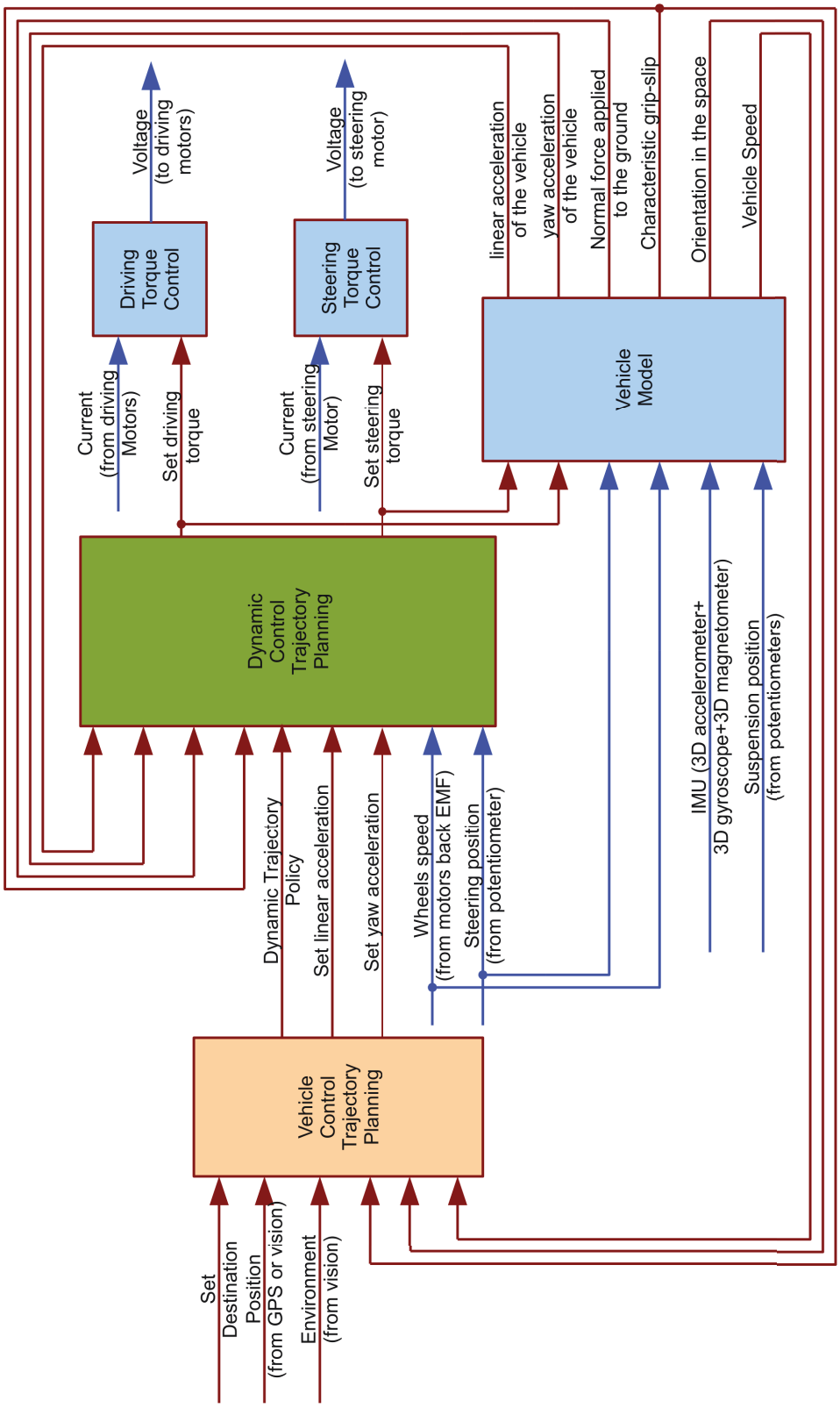

Figure 1.1: *The block diagram of the dynamic control of the vehicle*

that the motors and the wheels are linked by a direct gear.

A mathematical model of the vehicle is used in order to calculate the speed and the acceleration of the vehicle, its orientation in the space, the normal force applied to the ground at the four wheels and the grip offered by the ground. The vehicle model is based on the mechanical parameters of the vehicle, and its inputs are the speeds of the wheels, the steering position, the suspension position and the acceleration data in the three dimensions coming from an inertial measurement unit (IMU).

The blocks coloured in blue in Figure 1.1 represent my personal contribution and the main topic of this thesis. In particular:

1. I selected the most suitable components and I designed the hardware for the driving-torque control and the steering-torque control.

2. I programmed the control units in order to perform quick and reliable torque control.

3. I programmed the control units in order to communicate between them and with the sensors (voltage sensor, steering position sensor, current sensors, IMU).

4. I programmed the control units in order to calculate the vehicle acceleration, the vehicle orientation and the normal force applied to the ground.

5. I proposed a novel technique to estimate the grip offered by the ground in order to prevent the loss of adhesion during the execution of the planned trajectories.

The first three points are described in detail in Chapter 4. It took most of my PhD to set up a vehicle which can be fully controlled by a human from a remote computer, offering robust driving performances. The fourth point is partially discussed in Chapter 3. In the same chapter I present the vehicle model that will be later considered for the estimation of the grip with the ground. This model requires a precise knowledge of the mechanical parameters of the vehicle, including the vehicle moments of inertia and the model of the suspensions. Unfortunately these data were not available for the vehicle I developed, as their precise measurement would have required extensive work outside the scope of my research. For this reason, the latest revision of the code I have written for the vehicle does not consider dynamic effects such as weight transfer and suspension movements: it only considers the instantaneous vehicle orientation and the corresponding distribution of the gravitational force. The fifth point is extensively discussed in Chapter 5. Because of the missing data for the mechanical parameters of my vehicle, I did not implement the proposed

estimation technique on the vehicle. However, I validated it in simulation using a simplified model of the vehicle, which focuses on the longitudinal forces acting on a single wheel.

1.2 Battery Electric Vehicles

In a scenario where the global community is increasingly concerned about environmental protection, BEVs are now going through an extraordinary stage of development and are becoming increasingly popular (Chan and Wong 2004). This is because they represent a clean and silent means of transportation, being also particularly energy efficient. A wide adoption of this technology would break the dependence of transportation on fossil fuels, encouraging the transition towards cleaner and more sustainable energy sources (Husain 2010). In addition to this, the pollution emitted from the electrical power plants, if any, could be handled responsibly in a controlled environment instead of being distributed across our cities by a multitude of internal combustion engine vehicles (ICEVs) (Hodkinson and Fenton 2001).

The push towards electric vehicles is fostered by the high retail price of petrol, thus promoting the use of electric energy. Governments actively contribute by forcing vehicle manufacturers to reduce CO_2 emissions in new vehicles (Wansart and Schnieder 2010), as well as introducing low emission zones in central areas of some of our cities. From a technical point of view, BEVs require a much smaller number of moving parts compared to ICEVs, and vehicle manufacturers have already claimed a reduction of over 10% in the maintenance cost (Duleep et al. 2011). In its simplest form, the drivetrain of BEVs only consists of an electric battery, an electric motor and a motor controller. Of these three components, only the electric motor is actually moving, and it has a much simpler structure than an internal combustion engine, besides being much lighter. Electric motors do not require a clutch because they can provide torque to the wheel at zero speed. Moreover, they do not require multiple gear ratios and a shifting mechanism, because they are able to provide a constant torque over a wide range of speed. A permanent magnet synchronous motor such as the Yasa Motors YASA-400 can deliver 90 kW of continuous power, weighing only 22 kg (*YASA Motors Website*). For comparison an engine with similar power, such as the General Motors ECOTEC 1.6L I-4 VVT (LDE), weighs 116 kg while offering a lower output torque (155 Nm against 400 Nm of the YASA-400) (*GM Powertrain Website*).

The motor controller has to modulate the voltage provided to the motor in order to control the torque generated, according to the request of the driver. In recent years, a lot of effort has been made to integrate as many functional-

ities as possible into the motor controller in order to increase the performance and reduce the cost of BEVs. This integration is possible because of three key characteristics of BEVs which completely outclass conventional ICEVs in control performance (Fujimoto, Fujii, and Takahashi 2007; Hori 2004):

1. The torque control of electric motors is very quick. The torque response of most of the BEVs is in the order of few milliseconds (Hori 2004; Liu et al. 2005), many times faster than the torque response of internal combustion engines or even hydraulic braking systems.

2. The motor torque can be precisely measured and the motor speed can be easily estimated (Bose 1997). The torque generated by the electric motors is roughly proportional to the current flowing at their terminals which can be measured with the current sensors in-built to the motor controller. The motor speed is roughly proportional to the back electromotive force which can be estimated from the electrical characteristics of the motor, the voltage applied to the motor and the resulting current.

3. The low weight and the small size of the electric motors allow for the installation of multiple units on the same vehicle. In particular, it is possible to directly connect one motor to each wheel, in order to independently control the torque provided to every wheel (Sakai, Sado, and Hori 1999; Shino et al. 2000).

These qualities of BEVs would allow the integration of technologies such as anti-lock braking system (ABS), anti-slip regulation (ASR) and electronic stability control (ESC) without the need for specific control units or dedicated actuators (Hori, Toyoda, and Tsuruoka 1998; Sado, Sakai, and Hori 1999). Assuming all the four wheels of the vehicle could be controlled independently by four electric motors, it would be possible to remove from the vehicle the electrically-actuated valves and the pump required by the ABS as well as the wheel speed sensors. The only additional hardware required, in order to perform the ESC, would consists of an inertial measurement unit (IMU) and a steering position sensor. Using motors powerful enough to guarantee satisfactory braking performance means it would also be possible to remove the hydraulic braking circuit from the driven wheels, getting rid of calipers, disc brakes and brake pads. The maintenance of such a vehicle would be minimal compared with a conventional car.

The major problems of BEVs are mostly related to the limitations of the batteries (Ehsani, Gao, and Emadi 2009; Khan 2006). In particular the cost, which in 2011 was around 500 $\$/kWh$ for a mass-produced vehicle (Duleep et al. 2011; Howell 2012). A BEV of 1500 kg requires about 25 kWh of battery capacity to provide a range consistently larger than 100 km (data for

the Nissan Leaf in 2012 from *US EPA Fuel Economy Ratings*). The driving range can greatly vary, depending on the driving condition, and the data here reported is quite conservative (Nissan claims that in optimal conditions the same vehicle can reach up to 222 km with a single charge). Nonetheless, in order to guarantee 100 km of range, the cost of the battery is roughly 12500 \$ per vehicle, which is about one third of the total price of the car.

Cost aside, adding battery capacity to a vehicle is not convenient because of the low energy density of the batteries. The best commercially available cells for BEVs offer an energy density around 180 Wh/kg and 350 Wh/l (Dow Kokam Xalt HE 75 from *Dow Kokam Batteries Website*), meaning that roughly 140 kg of batteries, taking about 70 l of volume, are needed for every 100 km of range. The gasoline, in contrast, present an energy density around 12 kWh/kg and 8 kWh/l (Thomas 2000). Taking into account the better overall efficiency of the electric powertrain compared to the internal combustion engine, in the order of 80% and 20% respectively (Sweeting, Hutchinson, and Savage 2011), 8 kg of gasoline are needed for every 100 km of range. This comparison clarifies the reason behind the limited range of BEVs. While a battery weight of 140 kg is partially compensated by the lower weight of the electric motor compared to internal combustion engines of the same power, extending the range to more than 100 km would make the BEV much heavier than a similar ICEV. This would result in poor handling of the car, but also the overall efficiency of the vehicle would be affected. In fact a considerable amount of energy is required to accelerate the additional weight and only a small part of it, less than a third, can be recovered through regenerative braking (Larminie and Lowry 2003).

Another serious problem with the batteries is the time required to recharge them (Khan 2006; Larminie and Lowry 2003). A 230 V socket can provide power between 2.3 kW and 3.7 kW, for 10 A and 16 A fuse respectively (Grahn and Söder 2011). This is the most common charging solution at the moment and it would require from 6 to 10 hours to charge a 25 kWh battery. Very few fast-charging stations are available, which use high current to charge half of a similar battery in roughly 10 minutes (Grahn and Söder 2011; Grünig et al. 2011). However, these are expensive stations which would increase the charging cost. In addition, the use of high currents to charge the battery will dramatically reduce the battery life (Grünig et al. 2011).

The good news about battery technology is that it is rapidly evolving. Only a few years ago there were serious concerns about safety and life time of lithium-ion batteries. Moreover, there were important limitations in the power density, for both discharging and charging of the battery. In 2013, most of these issues seem solved, with encouraging data from crash tests and safety reports. The calendar life of the battery is now estimated as roughly 10 years,

while more than 3000 charging cycles can be sustained (Duleep et al. 2011; Grahn and Söder 2011). Nowadays cells with high energy density such as the Dow Kokam Xalt HE 75 offer a discharging power density of 890 W/kg and a charging power density of 356 W/kg (*Dow Kokam Batteries Website*). Projecting these figures on a BEV with 140 kg of batteries, this means such a vehicle would have an accelerating power of 125 kW and a regenerative braking power of 50 kW, which is enough for most of the braking in a urban environment although not enough for emergency braking. For applications which require higher power density, such as hybrid-electric vehicles, specific batteries are used. These batteries can offer a discharging power density up to 2500 W/kg (A123 Systems AMP20 from *A123 Website*).

1.3 Friction Characteristic and Slip Ratio

In this thesis I propose a technique to estimate the **friction characteristic** between the tyre and the ground. The friction characteristic will be extensively discussed in Chapter 2. However, for the sake of clarity, I will here introduce the basic definitions. In general, the friction characteristic is the relationship between the tangential force applied to the ground by the tyre and the resulting sliding between the tyre and the ground. This characteristic can be measured along different directions.

Along the heading direction of the wheel, the force applied to the ground by the tyre is defined as **longitudinal tyre force $\mathbf{F_x}$**, while the sliding between the tyre and the ground is quantified by the **slip ratio**. The definitions of slip ratio are various and they are all beyond the scope of this introductory chapter. At this stage it is only necessary to know that the slip ratio is a normalised value of the difference of speed between the wheel and the vehicle. I am going to use a separate definition for the slip ratio during acceleration and the slip ratio during braking, respectively represented by the symbols $\mathbf{\Lambda_t}$ and $\mathbf{\Lambda_b}$. In this thesis, a slip ratio of 0 corresponds to a free-rolling wheel, a slip ratio of -1 corresponds to locked braking and a slip ratio of 1 corresponds to a wheel skidding on the ground without moving the vehicle. The precise definition of the slip ratio will be given in Chapter 2.

The characteristic between slip ratio and longitudinal tyre force is called **longitudinal friction characteristic**. In symbolic terms, I will refer to the longitudinal characteristic using the formula $\boldsymbol{F_x}(\boldsymbol{\Lambda_t})$ or $\boldsymbol{F_x}(\boldsymbol{\Lambda_b})$, to specify that the characteristic is the longitudinal tyre force in function of the slip ratio, as well as to clarify which definition of slip ratio is used. This characteristic is non linear and highly variable with tyre properties and road surface conditions (Khatun et al. 2003; Wong 2008). Moreover, it depends on the **normal**

tyre force $\mathbf{F_z}$, which is the force pushing the tyre against the ground. The relationship between the longitudinal tyre force at a given slip ratio and the normal tyre force is almost linear (more details in Chapter 2). For this reason it is meaningful to define the **longitudinal friction coefficient $\boldsymbol{\mu_x}$** as the ratio between the two forces ($\boldsymbol{\mu_x}(\boldsymbol{\Lambda_t})$ or $\boldsymbol{\mu_x}(\boldsymbol{\Lambda_t})$ can also be used to refer to the longitudinal friction coefficient, in order to highlight the dependency on the slip ratio). This is expressed by Equation 1.1.

$$\mu_x(\Lambda_t) = \frac{F_x(\Lambda_t)}{F_z} \tag{1.1}$$

The longitudinal friction coefficient should not be confused with its maximum value, which is usually a constant property of two surfaces in contact with each other (for the sake of this thesis, the two surfaces are the tyre and the ground). The longitudinal friction coefficient depends on the slip ratio and it can be as low as 0 when the slip ratio is null. The characteristic between longitudinal friction coefficient and slip ratio is called **normalised longitudinal friction characteristic**, because it corresponds to the friction characteristic normalised by the normal force. In this thesis, *longitudinal* will be sometimes omitted if implied by the context.

Figure 1.2 shows the typical behaviour of the normalised longitudinal friction characteristic for a dry road. This characteristic in particular is the one that I used to validate my estimation technique in simulation. In general, when no torque is applied, a tyre operates at zero slip ratio. By applying some torque to the wheel, the operating point progresses along the friction characteristic. During the first part of the friction characteristic, the relationship between slip ratio and friction coefficient is almost linear. For every increase in torque corresponds an increase in longitudinal force (therefore friction coefficient) as well as an increase in the slip with the ground. By further increasing the torque, the operating point enters a transitional region, where the friction characteristics presents a maximum point. This corresponds to the maximum longitudinal force that can be sustained by the friction between the two surfaces: the tyre and the ground. While operating at the maximum of the friction characteristic, an increase in torque will only translate in rotational acceleration of the wheel without a corresponding acceleration of the vehicle, causing an increase in the slip ratio. This is because no more longitudinal force can be sustained at the interface with the ground. Because of the decreasing behaviour of the friction characteristic after its maximum, with the increase of the slip ratio the wheel will encounter less and less resistance from the ground and it will start skidding on the ground. Wheel skidding negatively affects the control of the

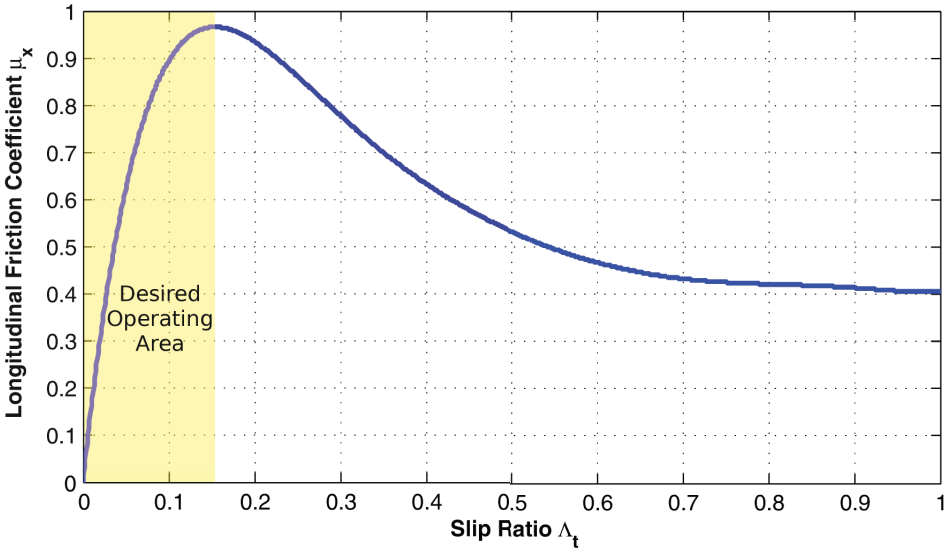

Figure 1.2: $\mu_x(\Lambda_t)$ *characteristic used in simulation*

car, particularly the longitudinal performance and the lateral stability (they will all be discussed in detail in Chapter 2). It is therefore desirable to operate the vehicle in the region between zero slip ratio an the slip ratio corresponding to the maximum friction coefficient. This is one of the fundamental targets of traction control (TC).

1.4 Friction Characteristic Importance in Traction Control

In Section 1.2 I introduced the advantages of BEVs over ICEVs in the implementation of functionalities such as ABS, ASR and ESC. These technologies aim to improve driving performances as well as to assist the driver in emergency manoeuvres (such as braking) by maximising the grip of each wheel with the ground (Hori, Toyoda, and Tsuruoka 1998). They are often deeply integrated with each other, sharing the same controller, sensors and actuators (Milliken and Milliken 1995). Because of this tight integration, I will generally refer to them as techniques for traction control TC, although this term is sometimes used to indicate solely ASR (Wong 2008). In this thesis, TC will refer to any technology that takes partial control of the vehicle whenever the trajectory of the vehicle does not match the commands of the driver, because of a lack of grip with the ground.

TC is a technology integrated in the vast majority of road vehicles, although there is a high variability in complexity and functionality. In general, TC improves driving safety in difficult road conditions as well as stability dur-

ing high performance driving. BEVs could offer a boost of performance for TC technologies, due to their particular characteristics discussed in Section 1.2. In addition to improving the driving safety, this increase in performance would allow the mounting of low-drag tyres, which would increase the overall efficiency of the vehicle. This could extend the range of BEVs (Delli Colli, Tomassi, and Scarano 2006; Hori, Toyoda, and Tsuruoka 1998) and enhance the market competitiveness of BEVs.

TC systems are usually managed by electronic control units. These devices use a detailed mathematical model of the vehicle and measurements coming from several sensors distributed across the vehicle, in order to detect the behaviour of the vehicle as well as the intentions of the driver. Often these measurements include the linear and rotational acceleration of the vehicle, the rotational speed of the wheels and the steering column position. The electronic control unit alters the trajectory of the vehicle using electrically actuated valves and hydraulic pumps acting on the hydraulic braking circuit (Savaresi and Tanelli 2010), fuel injection and engine ignition to modify the engine torque (Wong 2008), and sometimes a steering motor to change the steering position (Koehn and Eckrich 2004).

TC can be classified into two classes: longitudinal and lateral control (Hori, Toyoda, and Tsuruoka 1998). ABS and ASR are examples of longitudinal control while ESC is a very popular implementation of lateral control. Longitudinal control aims to control the slip ratio in order to provide, when required, the highest driving or braking force applicable to the ground. A prior knowledge of the longitudinal friction characteristic is essential to determine the optimal slip ratio, as well as the feasibility of certain trajectories. The performances of the longitudinal control are strongly dependent on this knowledge.

Lateral control aims to keep the vehicle on the desired trajectory, whenever the vehicle tends to deviate sideways because of a lack of grip with the ground. In general, the electronic controller measures the angular velocity on the horizontal plane of the vehicle, called yaw rate, comparing it with the target value set by the driver. The latter is derived from the steering position and the vehicle speed. The controller then balances the torque between the wheels on the right side of the vehicle and the wheels on the left side, generating a moment of force in order to reduce the error in the yaw rate (Sakai, Sado, and Hori 1999). It is basically the same principle used for skid steering (Shuang et al. 2007), the technique used to turn a vehicle with non-steerable wheels by providing a different driving torque to the wheels of different sides. The most refined techniques for lateral controls use four motors (Hallowell and Ray 2003; Jalili-kharaajoo and Besharati 2003; Pusca et al. 2002; Sakai, Sado, and Hori 1999), one for each wheel, but valid controls have also been proposed for

two-wheel drive (Fujimoto et al. 2004; Shino et al. 2000). In some advanced implementations, the steering position is also controlled (Koehn and Eckrich 2004).

Because the lateral control operates on the longitudinal forces generated at each tyre, it is highly dependent on the performances of longitudinal control. Mainly two ways of combining the longitudinal with the lateral control have been adopted:

1. The yaw rate control is external to the slip ratio control (Fujimoto et al. 2004; Pusca et al. 2002; Sakai, Sado, and Hori 1999). This way, if any of the wheels is skidding, the longitudinal control reduces the torque applied to the skidding wheels. However, because the set torque for a specific wheel is the output of the lateral control, the performances of the lateral control will be compromised by the intervention of the longitudinal control.

2. The slip ratio control is external to the yaw rate control (Hallowell and Ray 2003; Jalili-kharaajoo and Besharati 2003). This way, if any of the wheels is skidding, the total set torque is reduced by the longitudinal control, and the total set torque is then distributed among the wheels by the lateral control.

The second implementation is in general more reliable than the first one, however it is not optimal for some particular situations. For example, if the vehicle has four driven wheels and one wheel is skidding, a better solution would be to transfer some torque from the skidding wheel to the other one on the same side, without limiting the total torque available and maintaining the lateral control.

Regardless of the particular integration between longitudinal and lateral control, these two technologies are strongly dependent on each other. In particular, both of them will substantially benefit from a prior knowledge of the friction characteristics for any driving condition. Because the driving conditions have a high variability, it is necessary to estimate the friction characteristic during continuous operation of the vehicle. This thesis will focus on the continuous estimation of the friction characteristic, in order to determine the optimal slip ratio for any driving condition. The approach I am going to propose is targeted to electric vehicles with independently driven wheels. These vehicles are suitable for advanced TC techniques, both in longitudinal and lateral control. Because the research in longitudinal control and the estimation of the friction characteristic are tightly linked together, I will present a review of both technologies in Section 1.5.

1.5 Longitudinal Control and Friction Characteristic Estimation

Over the last few years, several techniques of longitudinal control for electric vehicles have been developed. Some of them merely prevent the slip ratio from being too large, without a precise control of its value. In this direction, several papers have been published that exploit the back-electromotive force in the motors in order to reduce the torque whenever a wheel starts skidding on the ground (Liu et al. 2005; Peng et al. 2009). In the case of electric motors connected directly to the wheels, in fact, the skidding of a wheel corresponds to a rapid increase in the speed of the driving motor. This causes the back-electromotive force of the motor to rise, an effect that is usually compensated by the motor controller with a variation of the voltage applied. The cited papers propose to add a small delay in this compensation, so that the sudden growth of the back-electromotive force would temporarily reduce the current in the motor. This would be reflected in a reduction of the torque applied to the wheel, thus limiting the skidding of the wheel on the ground.

A different approach to limit the slip ratio is to control the speed of the wheels to follow, with some margin (otherwise the vehicle will not move at all), the acceleration pattern of wheels in complete adhesion with the ground, which is calculated using a mathematical model of the vehicle (Fujimoto et al. 2004; Sakai, Sado, and Hori 1999). Having the wheels in complete adhesion with the ground corresponds to zero slip ratio, which is not a realistic model (Chapter 2 will explain why some slip ratio is always necessary to accelerate). However, because the desired slip ratio is always small, this is a good method to calculate the approximated value of the desired wheel speed. The skidding of a wheel is detected whenever the measured wheel speed significantly exceeds the speed of the wheels in conditions of adhesion, at which point the torque has to be reduced accordingly. Another popular approach to longitudinal control consists in controlling the slip ratio to a fixed value, independent from the conditions of the ground (Akiba et al. 2007; Chenglin et al. 2009; Foito, Guerreiro, and Cordeiro 2008; Jalili-kharaajoo and Besharati 2003; Pusca et al. 2002; Zhang, Yin, and Zhang 2006). A problem with this solution is that the system is usually tuned to accommodate the worst case scenario, typically icy conditions. Consequently, suboptimal slip ratios are imposed for most driving conditions (Khatun et al. 2003).

More advanced TC techniques evaluate the response from the road to determine some parameter, such as the maximum force applicable to the ground (Yin, Oh, and Hori 2009), or the entire friction characteristic (Delli Colli, Tomassi, and Scarano 2006; Hori, Toyoda, and Tsuruoka 1998; Sado, Sakai,

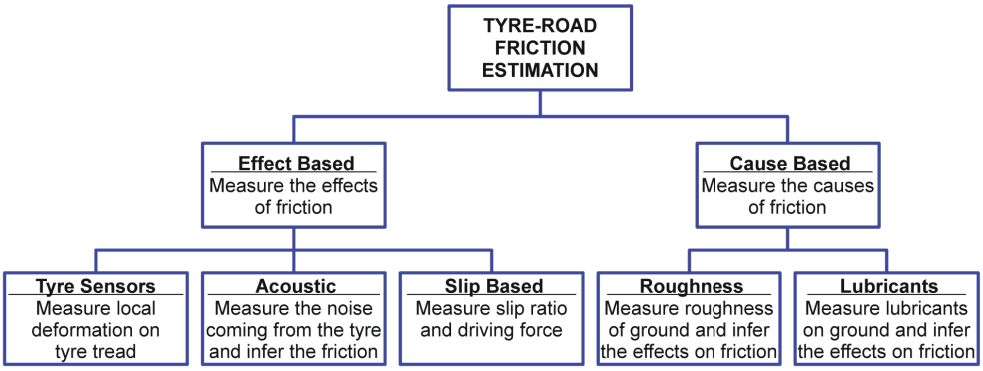

Figure 1.3: *The different branches of estimation of the ground characteristic (Müller, Uchanski, and Hedrick 2003)*

and Hori 1999). The latter has proved to be the most effective solution in order to offer optimal performances for any condition of the ground. For this reason, the estimation of the friction with the ground during vehicle operation has been a topic extensively researched, since the early 1990s (Li, Wang, and Zhou 2006). At the beginning the applications were targeted to ICEVs, however it is by focusing on electric vehicles that advanced techniques of estimation of the friction characteristic have been conceived.

There have been several approaches to the estimation of the friction characteristic, which can be grouped into two main categories (Müller, Uchanski, and Hedrick 2003):

1. Cause-based approaches try to measure factors that lead to changes in friction with the ground and they use this information to infer the friction characteristic, or some qualities of it, according to previous experience or analytical friction models. In general they measure characteristics of the road, such as composition and roughness, or characteristics of any substance that covers the road, such as water, snow, ice, or oil. These approaches are strongly dependent on the analytical models or the training data used. Moreover, they mainly use optical sensors, which require a proper illumination and a high resolution (Müller, Uchanski, and Hedrick 2003).

2. Effect-based approaches try to measure the effects of the friction with the ground, and they use this information to infer the friction characteristic, or some qualities of it, according to previous experience or analytical friction models. In general they measure the response of the vehicle to the longitudinal tyre force, in the form of slip ratio, deformation of the tyre or acoustic noise generated from the friction with the ground. The slip ratio can be estimated from the knowledge of the torque applied to the wheels and the resulting speed of the wheels. The last information

is obtained from speed sensors integrated in most of mass-produced cars nowadays. The measurement of the deformation of the tyre requires dedicated sensors inside the wheel, which are prone to damage and are not easily connected to the circuitry in the car. The measurement of the acoustic noise is relatively cheap to implement, however external disturbances and the complex nature of tyre noise makes it difficult to use it to estimate the friction with the ground (Müller, Uchanski, and Hedrick 2003).

Figure 1.3 summarises the main branches of the research in the estimation of the friction characteristic, as previously discussed. In this thesis I am focusing on estimation techniques that can be implemented in every electric vehicle with minimum cost. In particular, I aim to present techniques that are reliable, unaffected by external disturbances, and that do not rely on dedicated hardware. The approach that better meets these criteria is based on the measurement of the slip ratio. In the following paragraphs I am going to review the state of the research in this area.

1.6 Slip-Based Estimation

Slip-based estimation techniques for the longitudinal friction characteristics aim to quantify both the slip ratio and the longitudinal tyre force. Most of the earliest attempts calculated the slip ratio of the driven wheels by measuring the speed of every wheel and by using the speed of the undriven wheels as a measure of the vehicle speed. The longitudinal tyre force was calculated from the acceleration of the vehicle, by making assumptions of the aerodynamic drag, the rolling resistance and any additional external force (Germann, Wurtenberger, and Daiss 1994; Ray 1995). The obtained points on the friction characteristic were fitted to empirical friction models, in order to reduce the effect of the noise in the measurements. A very interesting article proposed how to determine the type of ground (gravel, asphalt, snow or ice) from the slope of the friction characteristic at very low values of slip ratio, when this characteristic is approximately linear (Gustafsson 1998). The variance in the measurement of the wheel speed was used to recognize the gravel. All parameters were determined using a Kalman filter, in order to reduce the effects of white noise in the measurements. In the aforementioned article, the longitudinal tyre force was estimated according to a detailed engine model, starting from the knowledge of the fuel injection. A later article compared the fitting of experimental data to a linear characteristic with the fitting to a non-linear friction model, discussing the correlation between the initial slope of the friction characteristic and the maximum longitudinal tyre force (Müller, Uchanski,

and Hedrick 2003). This article however failed to provide a reliable method to estimate the longitudinal tyre force, without a prior knowledge of the external forces acting on the vehicle.

With electric motors offering precise information about the torque generated and the motor speed, it became possible to easily estimate the longitudinal tyre force from the torque provided to the motors and the resulting wheel acceleration (Hori, Toyoda, and Tsuruoka 1998). Some authors used the longitudinal tyre force to estimate the vehicle speed, making assumptions over the external forces acting on the vehicle (Liu and Peng 1996). Others used the torque provided to the wheels and the wheel speed to determine the parameters of analytical models of the friction characteristics (Canudas De Wit and Horowitz 1999; Nishira, Kawabet, and Shin 1999). Starting from the longitudinal tyre force and the slip ratio, the derivative of the longitudinal tyre force with respect to the slip ratio was calculated and used as a control feedback (Delli Colli, Tomassi, and Scarano 2006; Sado, Sakai, and Hori 1999). This parameter is in fact a good indicator of the torque margin between the current operating conditions and the maximum torque that can be transferred to the ground. Without measuring the speed of the vehicle, a detector for wheel skidding was proposed (Sakai, Sado, and Hori 1999). One of the most refined approaches correlated the slope of the friction characteristics at low slip ratio to typical friction profiles, obtaining an estimate of the maximum longitudinal tyre force (Furukawa and Hori 2003). Up to this point all the approaches were affected by the external forces acting on the vehicle, therefore a slip ratio estimator considering the external force was presented (Fujimoto, Fujii, and Takahashi 2007). Instead of using the speed of undriven wheels as indicators of the vehicle speed, this approach used an accelerometer mounted on the vehicle to measure the vehicle acceleration and to estimate the external forces. The vehicle speed was calculated by simple integration.

The majority of the articles reviewed use several filters or state observers in order to merge multiple measurements and to reduce the effects of the noise in the measurements. Reviewing the performances of these filters and observers is outside the scope of my research, instead I will focus on the cost, the performance and the reliability of the different estimation techniques. All of them rely on a very simple idea: there are five different rigid bodies in the vehicle. These are the four wheels and the sprung mass. Assuming that these bodies are rigidly connected at the hubs, which is not entirely true because of the suspensions, it is possible to identify ten degrees of freedom of the system: the rotational position of each wheel and the position of the vehicle in space (six degrees of freedom). In general, the estimation of the friction characteristic is based on the longitudinal motion of the vehicle. For this reason, it is possible

to limit the analysis to five degrees of freedom. The accelerations of interest are: longitudinal acceleration of the vehicle and rotational accelerations of each of the four wheels. The forces of interest acting on the vehicle are: total longitudinal force and moments of force acting on each of the four wheels.

Most of the research in the field is based on the assumption that the linear and the rotational inertia of these five bodies are well known. Under this condition, it is possible to calculate the accelerations of the bodies by knowing all the forces acting on them. Conversely, by measuring all the accelerations it is possible to estimate the total forces acting on the bodies. The speeds could be obtained by integrating the accelerations, although in practice this is not an easy operation. In fact, a small offset in the measurement of the acceleration can lead, in the long term, to a huge deviation between the speed calculated and the actual speed. This is the reason why integrating the output of an accelerometer does not provide a good estimate of the vehicle speed, although it precisely detects its high-frequency variations. In order to correctly estimate the vehicle speed, a low-frequency reference speed is required. In general, to measure the longitudinal speed of a vehicle, the low-frequency reference is obtained from the speed of undriven wheels or position data from global positioning system (GPS) or analysis of video stream coming from cameras mounted on the vehicle.

A major problem addressed in the literature is the lack of information to fully describe the system. In general, the rotational speed of the four wheels is measured in most of the cars, because it is needed for the operation of the ABS. The speed of the vehicle, instead, is not directly measurable in every situation. Although most of the time it can be obtained from the rotational speed of the undriven wheels, there are situations in which undriven wheels are not available, such in the case of braking or 4-wheel drive vehicle (Sakai, Sado, and Hori 1999). The use of GPS is not reliable because the coverage can be spotty, and the position update is relatively slow. The use of speed information from cameras requires substantial computational power and it is affected by the visibility. Moreover, GPS units and cameras are often not integrated in the vehicles.

The torque applied to the wheels is also challenging to measure in ICEVs, because it would mainly require a torque sensor for every wheel. Solutions using engine lookup-tables have been proposed, however, in order to be accurate, they would need a detailed model of the engine together with information about the ignition and the mix of fuel and air coming into the combustion chamber. This information is usually not available in conventional passenger cars. In BEVs the torque provided to the wheels is easily determined from the current flowing through the motor. When a motor is directly connected to

each wheel, the torque provided to each wheel is known.

It is basically impossible to directly measure all the forces acting on the vehicle in the longitudinal direction. In general, these forces are longitudinal tyre force, gravitational force, aerodynamic drag and rolling resistance. The longitudinal tyre force can be estimated from the torque provided to the wheels and the rotational acceleration of the wheel. All the torque that does not contribute to an increase in the rotational speed of the wheel is transmitted to the ground in the form of longitudinal tyre force. The gravitational force can be estimated from the knowledge of the mass of the vehicle and the orientation of the vehicle in relation to the vertical direction. Obtaining a reliable orientation of the vehicle could appear as a simple task, instead it requires an expensive IMU and a good knowledge of the initial orientation, as I will explain in Chapter 3. Aerodynamic drag and rolling resistance cannot be measured directly, because they are forces distributed across the body of the vehicle and the tyres. This forces are strongly dependent on the environment (wind, altitude, road surface, etc.) and the only way to quantify them is to estimate their value from the vehicle acceleration and the knowledge of the other forces acting on the vehicle.

All the articles that I came across base their approach on the measurement of the speed of every wheel, driven or undriven. Many articles focusing on ICEVs assume no prior knowledge of the torque provided to the wheels and they use the speed of undriven wheels as a measurement of the vehicle speed (Germann, Wurtenberger, and Daiss 1994; Müller, Uchanski, and Hedrick 2003; Ray 1995). They obviously have to make assumptions over the external forces acting on the vehicle, in order to estimate the longitudinal tyre force. Most of the articles focusing on BEVs assume the knowledge of the torque provided to each wheel but no information over the vehicle speed (Canudas De Wit and Horowitz 1999; Furukawa and Hori 2003; Hori, Toyoda, and Tsuruoka 1998; Liu and Peng 1996; Nishira, Kawabet, and Shin 1999; Sakai, Sado, and Hori 1999). They also have to make assumptions over the external forces, in order to determine the vehicle speed and therefore the slip ratio. Some articles assume the knowledge of both the torque provided to the wheels and the vehicle speed (Delli Colli, Tomassi, and Scarano 2006; Fujimoto, Fujii, and Takahashi 2007; Gustafsson 1998). In this case the system is fully determined and the sum of all forces acting on the vehicle can be calculated.

A problem that has been marginally discussed in the literature is the continuous excitation of the vehicle system (Germann, Wurtenberger, and Daiss 1994; Müller, Uchanski, and Hedrick 2003). Basically, it is not possible to estimate the behaviour of the friction characteristic while the vehicle exerts a constant longitudinal tyre force on the ground. This situation corresponds to

constant accelerations, constant decelerations or constant speed. The problem arises because a specific value of longitudinal tyre force is represented by a single point on the friction characteristic. This point on its own does not carry information about the friction characteristic in the neighbourhood of the point, which means it is not possible to detect if the operating point is in the linear region, close to the maximum of the longitudinal tyre force or in the skidding region. It is usually necessary to measure multiple points that are far apart, in order to understand the behaviour of the friction characteristic. Because the most common driving patterns are composed of long segments of driving at constant speed, interleaved by fairly constant acceleration or deceleration, the excitation of the system is a critical problem for the estimation of the friction characteristic. This is why most estimation techniques operate under progressive acceleration or braking manoeuvres. Often these manoeuvres need to be quite extreme, in order to approach the maximum driving force attainable. This is not safe for driving in public roads and it is not suitable for an autonomous vehicle, which is supposed to gather information in safe operating conditions. An interesting and recent article proposed to add oscillations to the torque provided to the wheels, in order to maintain the excitation of the system (Chen and Wang 2011). This approach used large oscillations to estimate a significant section of the friction characteristic, in order to fit the obtained data to a friction model. The effects of the oscillations on the unsprung mass are minimized by exploiting the actuator redundancy of a vehicle with independently controlled front and rear wheels. In particular, the torque oscillations at the rear wheels are calculated in order to minimize the effects of the torque oscillations at the front wheels, on the unsprung mass. This approach is also affected by the external forces acting on the vehicle, although these are not considered in the article.

1.7 Novel Approach to the Estimation of the Friction Characteristic

My approach aims to estimate the friction characteristic using two easily measurable variables: the torque provided to the wheel and the wheel speed. The torque can always be calculated from the current flowing in the motor, while the wheel speed can be estimated from the current, the voltage provided to the motor and the motor parameters. Other variables, such as the air resistance or the vehicle speed, are extremely difficult to be accurately measured.

The relationship between the motor torque and the wheel speed depends on the friction characteristic. In fact, the wheel acceleration depends on the torque applied to the wheels, but also on the amount of this torque that is

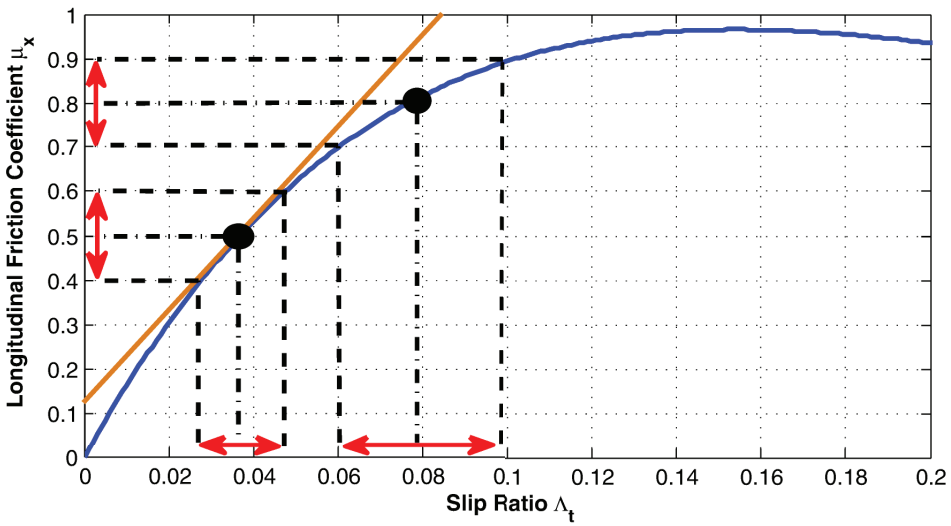

Figure 1.4: *The application of small-signal oscillations around an operating point*

distributed to the ground, which corresponds to the longitudinal tyre force. The smaller the fraction of the motor torque that is distributed to the ground, the quicker the wheel would accelerate because the inertia that the torque has to overcome would be lower (inertia of the wheel alone compared to the inertia of the whole vehicle). The fundamental idea behind many approaches to the estimation of the friction characteristic is to determine a mathematical relationship between the motor torque and the wheel speed, which obviously requires a mathematical description of the friction characteristic. By inverting the relationship, it would then be possible to obtain the friction characteristic. Several attempts have been made to fit the characteristic $\mu_x(\Lambda_t)$ obtained from experimental results to a mathematical description (Alvarez 1999; Canudas De Wit and Tsiotras 1999; Dahl 1968; Milliken and Milliken 1995; Pacejka 2005; Wong 2008). Some of these approaches are extensively reviewed in (Li, Wang, and Zhou 2006), however they are mainly relevant to specific kind of tyres and grounds. My aim is to propose an estimation technique which could fit to a generic friction characteristic. In order to do so, I will focus my analysis on a local relationship in the neighborhood of an operating point. The latter is defined by specific values of wheel speed, vehicle speed, motor torque, external force and their time derivative. In the neighborhood of the operating point I can apply small sinusoidal oscillations of torque in order to obtain small sinusoidal oscillations in the wheel speed. This is a characteristic behaviour of a linear system which can be easily understood by looking at Figure 1.4.

The blue line in Figure 1.4 is exactly the same friction characteristic in Figure 1.2 but, for clarity, the horizontal axis is limited between a slip ratio of 0 and 0.2. The two big dots in the figure represents two operating points on the

friction characteristic. Each point corresponds to a specific value of slip ratio and longitudinal friction coefficient. A small oscillation of torque would cause a small oscillation in the slip ratio around the operating point, introducing a variation in the longitudinal friction coefficient. From Figure 1.4 it is possible to notice that, for oscillations small enough, the relationship between slip ratio and the longitudinal coefficient of friction can be approximated with a straight line. The local relationship is therefore characterised by the slope of the line that best approximates the function in the neighbourhood of the operating point. This line is the tangent of the function $\mu_x(\Lambda_t)$ at any operating point. From now on, I will call η its slope, as defined in Equation 1.2.

$$\eta = \frac{d\mu_x}{d\Lambda_t} \tag{1.2}$$

The very important thing to notice is that the local relationship changes with the operating point. In particular, the parameter η decreases with the increase of the slip ratio until it becomes 0 in correspondence to the maximum value of the friction coefficient, before moving to negative values. I mentioned before that, from the vehicle control perspective, it is desirable to operate at slip ratios equal or smaller to the value required to reach the maximum longitudinal tyre force (more information in Chapter 2). In simple words, it is necessary to control the parameter η always in the positive range. The best way to do so is to reduce the torque provided to the wheels whenever η approaches 0. The core idea behind my approach is to exploit the fact that the local relationship between the motor torque and the wheel speed depends on η. My approach aims to estimate η by analysing the variation in the wheel speed after modulating the torque set by the driver with a small cosinusoidal signal.

I will demonstrate in Chapter 5 how the local relationship between motor torque and wheel speed depends on the frequency as well as other parameters, but here it is useful to give a rough explanation of the estimation process. As a first approximation one can say that, for frequencies high enough, the modulating signal of torque generates negligible oscillations in the vehicle speed, because of the large inertia of the vehicle body. The small inertia of the wheel allows instead for higher oscillations in the wheel speed, which dominate the oscillations in the slip ratio. For this reason it is possible to approximate the oscillations in the slip ratio with the oscillations in the wheel speed. Now I will focus on the measure of the longitudinal tyre force, considering a scenario where the characteristics of the ground and the external force acting on the vehicle are not changing. A further assumption would be to operate in an

area of low slip ratio, with positive values of η. Under these conditions, the increase of the longitudinal tyre force is always caused by an increase of the motor torque. Although they are not proportional to each other, the longitudinal tyre force and the motor torque are tightly linked together. In particular, one can say that an increase of the oscillation in the motor torque will always increase the oscillation in the longitudinal tyre force. To summarise, under this particular conditions one can use the oscillations in wheel speed as a measure of the oscillations in the slip ratio and the oscillations in the motor torque as a measure of the oscillations in the longitudinal tyre force. This is a rough approximation and it will only be quantified in Chapter 5. Now I will focus on the relationship between longitudinal tyre force and slip ratio. The red arrows in Figure 1.4 are used to highlight an important concept: similar oscillations in the longitudinal tyre force at different operating points generates oscillations in the slip ratio that are very different in amplitude. This is due to the difference of slope of the friction characteristic for different operating points. In particular, when the parameter η is closer to 0 and therefore the longitudinal tyre force is closer to its maximum, the oscillation in the slip ratio is larger. After all these considerations, using the approximations discussed in this paragraph it is possible to conclude that an equal oscillation in the motor torque corresponds to a larger oscillation in the wheel speed whenever the parameter η is lower. Monitoring the oscillation in the wheel speed resulted from a constant oscillation in the motor torque is therefore a viable solution to detect the proximity of the operating point to the maximum longitudinal tyre force attainable.

I have here provided a simple explanation of the estimation method proposed in this thesis. This explanation is only relevant to the particular case described above, as will be demonstrated in Chapter 5. This concept needs to be formalised and quantified, in order to be applicable to more general conditions. This will be the task of the following chapters. The method here presented requires a precise modulation of the torque generated by the motors and a frequent wheel speed measurement (in the order of 100 Hz). These requirement are almost impossible to meet with a conventional car powered by an internal combustion engine and using slotted wheel for the wheel speed measurement, while they are already met by most of the BEVs on the market. Because of this reason, I would like to stress how my method goes beyond a mere academic discussion and it finds its natural application in the coming generation of sustainable transportation.

1.8 Aim of the Research and Structure of the Thesis

This thesis is focused on BEVs with independently driven wheels. For this reason I will further assume precise knowledge of the torque provided to each wheel. My aim is to propose a technique that estimates the approaching of the maximum driving force during both acceleration and braking. Because during braking no wheel speed can be used to approximate the speed of the vehicle, the speed of the vehicle will be further considered unknown. Although it is normally not possible to estimate the speed of the vehicle without knowing the value of the forces acting on it, I will work around the problem by exciting the system at frequencies where the external forces acting on the vehicle have negligible effect. Gravitational force, aerodynamic drag and rolling resistance are in fact slow changing, because they are mainly related to the orientation and the speed of the vehicle. The vehicle, because of its large inertia cannot change speed or orientation too abruptly, while the torque provided by electric motors can change almost instantaneously.

The estimation technique I propose will maintain the excitation of the system by superposing a small oscillation to the torque request coming from the driver. Unlike the approach of Chen and Wang 2011, my approach does not require a large oscillation of torque in order to estimate a significant section of the friction characteristic, because my approach does not try to fit the obtained data to a friction model. Instead it will obtain local information about the friction characteristic, around the operating point. In particular, the approach that I propose will estimate the slope of the friction characteristic and the slip ratio at the operating point. The slope is an important parameters because it is the best indicator of the margin between the operating point and the maximum driving force. It is the input of several control techniques, aiming to use all the longitudinal tyre force available while keeping the slip ratio as low as possible (Delli Colli, Tomassi, and Scarano 2006; Sado, Sakai, and Hori 1999). In addition, the estimation of the slip ratio will provide a measure of the vehicle speed. This information is not essential for the optimum control of the torque provided to the wheels. Nonetheless it could be useful for other applications, such as the reconstruction of the full friction characteristic.

In summary, the aim of this thesis is to present the fundamental theory behind the estimation of the friction characteristic and to propose a reliable estimation during common operations of the vehicle, with the following novel features (some of them are not novel on their own but in combination with the others):

- My technique does not require extreme manoeuvres in order to obtain information about a large section of the friction characteristic, because

it estimates local information that can be used directly in the control of the slip ratio.

- My technique continuously detects changes in the ground grip, even during long sections at constant speed, because it maintains the excitation of the system by introducing oscillations in the motor torque.
- My technique does not rely on any measurement of the vehicle speed, nonetheless it is able to correctly estimate the value of the slip ratio.
- My technique is not affected by external forces acting on the vehicle, such as rolling resistance and aerodynamic drag, as long as these forces are slow-changing (when their frequency content is negligible, compared to the motor torque, around the frequency used to excite the system - the frequency of the torque oscillation).
- My technique does not require any hardware that is not already available in any mass-produced BEV.

I validated my novel approach through a simulation based on Simulink. This work has been presented in the IEEE International Conference on Vehicular Electronics and Safety (ICVES), in 2012 (Cecotti, Larminie, and Azzopardi 2012). In this thesis I will also describe the development of the remotely-controlled electric vehicle used for the ITS project. Although this might not be a novel contribution to engineering knowledge, it is an important collection of information gathered through literature review and my personal experience. It is a useful guide for anyone interested in developing an electric vehicle from scratch. I will discuss in detail the hardware used for my project as well the most critical challenges encountered.

The outline of this thesis is briefly summarised as follows. Chapters 2 and 3 will introduce the basic theory necessary to understand the challenges associated with the estimation of the friction characteristic between the tyre and the ground. They will discuss the operation of the tyre and the dynamics of the vehicle, respectively. In Chapter 3 I will propose a model to calculate the normal force applied to the ground at each wheel, using additional sensors to measure the movements of the suspension units. I will also present a method to calculate the orientation of the vehicle together with the longitudinal and the lateral acceleration, using an IMU. In Chapter 4 I will present my work on the vehicle, including the choice of the components used, the design of the electrical system, the design of the printed circuit boards (PCBs), the preparation and the tuning of the control code as well as the limitations in the control performance due to the hardware chosen. In Chapter 5 I will introduce my novel approach to the estimation of the friction characteristic. I will start

by presenting the general idea, supporting it with the mathematical theory behind it. Finally, I will discuss the performance of my approach, according to the simulation results. In Chapter 6 I will summarise the contributions of my thesis, discussing possible future developments.

Chapter 2

Tyre Behaviour

2.1 Introduction

The aim of this chapter is to analyse the forces generated at the interface between the tyres and the ground in driving conditions. This is particularly important because the major forces and moments affecting the motion of a ground vehicle are applied through the tyres (Wong 2008). The tyres support the vehicle weight, softening the roughness of the road and providing the tractive, braking and cornering forces. Moreover, the forces acting on the tyres generate aligning torque, which is perceived as a centring effect in the steering system. The tyres also dissipate some of the driving power through heat, because of the deflection of the carcass while rolling (Wong 2008).

The content of this chapter is based on a thorough literature review of the most influential sources in the field. It is intended to introduce important concepts that will be frequently recalled in the following chapters. The aim of this thesis is to present a novel technique to estimate the friction between the tyre and the ground, and it requires a good understanding of the tyre mechanics. My approach does not use any information about the physical characteristics of the tyres mounted on the vehicle, nonetheless it does rely on the typical behaviour of pneumatic tyres, which is described in this chapter.

In Section 2.2 I will introduce the axis system used to decompose the forces and the moments of force acting on the tyre. I will analyse the forces along the longitudinal and the lateral direction in Section 2.3 and 2.4 respectively. I will explain the moment of force around the vertical direction in Section 2.5, while I will use Section 2.6 to discuss the combination of longitudinal and lateral force. Finally, in Section 2.7 I will present the effects of the lateral tilt on tyre operations.

2.2 Tyre Axis System

In order to decompose the forces and the moments of force acting on the tyre, it is necessary to define an axis system. In this thesis I will use the axis system recommended by the Society of Automotive Engineers (SAE), as shown in Figure 2.1 (Vehicle Dynamics Standards Committee 2008).

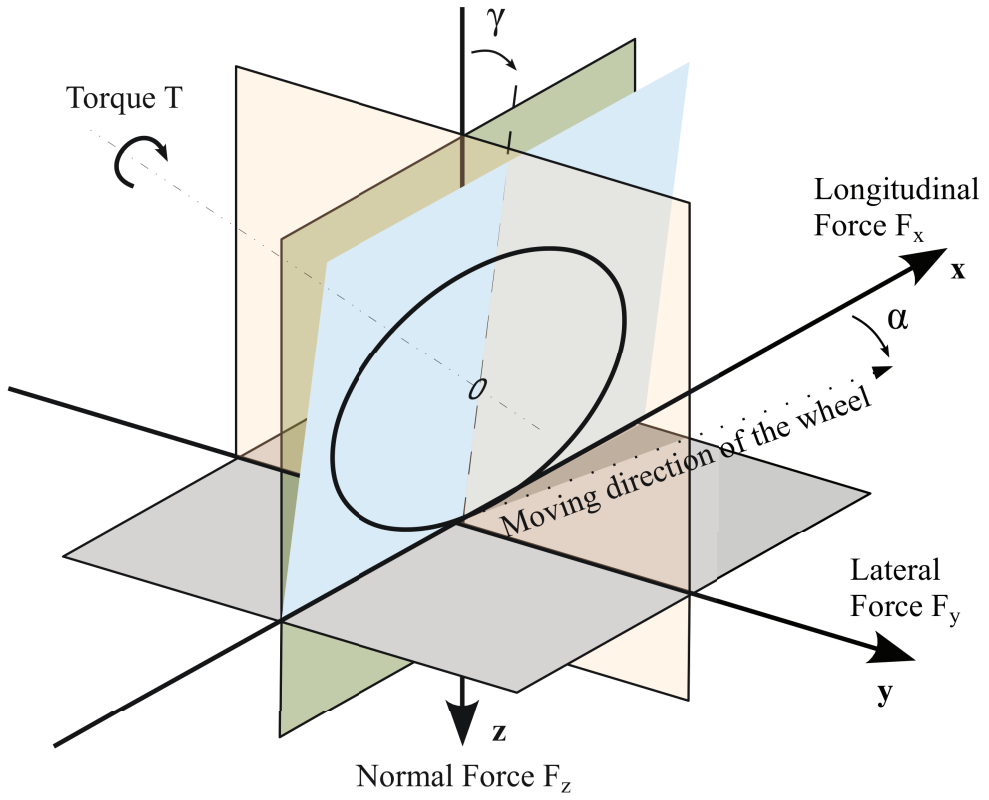

Figure 2.1: *SAE tyre axis system*

A SAE tyre coordinate system is defined for every single wheel, with the origin at the centre of the contact patch between the tyre and the ground. Assuming a flat road surface, a road plane at the contact patch can be defined. The x axis is the intersection between wheel plane and road plane and it is oriented towards the direction of the wheel heading. The z axis is normal to the road plane and directed towards the ground, while the y axis is normal to the plane containing the x axis and the z axis. This is represented in Figure 2.1.

Whenever the tyre is in contact with the ground, a force is generated at the contact patch. This force can be represented in the tyre coordinate system by a single vector, according to the magnitude and direction of the force. This vector is conventionally decomposed into its projections along the axes of the tyre coordinate system. While the projection along the x axis is the longitudinal tyre force F_x, the projection along the y axis is defined as **lateral tyre force $\mathbf{F_y}$** while the projection along the z axis is the normal tyre force F_z.

The angle between the z axis and the wheel plane is defined as **inclination angle $\boldsymbol{\gamma}$** while the **tyre slip angle $\boldsymbol{\alpha}$** is the angle between the x axis and the moving direction of the wheel (which might be different from the heading of the

wheel). In this thesis I am going to use the symbol $\mathbf{\Omega}$ to identify the **angular velocity of the wheel**. Although this choice is in disagreement with the SAE terminology, which uses the symbol ω instead, it is consistent with the convention here adopted of using the upper case for the variables describing the forces acting on the vehicle and the resulting displacement. The reason behind this will be clarified in Chapter 5. While Ω will be used to identify the angular velocity of any wheel, the symbol $\mathbf{\Omega_0}$ will be reserved to represent the angular velocity of a non-sliding (free-rolling) wheel. This would allow an easy comparison between driven and undriven wheels. The **wheel torque T** is the moment of force around the rotational axis of the wheel and $\mathbf{V_v}$ is the linear speed of the tyre centre, also called **longitudinal speed of the vehicle**.

2.3 Longitudinal Force

When a driving torque is applied to a wheel, a longitudinal tyre force is developed at the contact patch between the tyre and the ground. This is the force required to accelerate or to brake the vehicle. Figure 2.2 shows the behaviour of the tyre when a driving torque is applied to the wheel.

To understand the longitudinal force acting on a driven wheel it is important to analyse first the longitudinal stress in a free-rolling tyre. This is described by curve 1 in Figure 2.2. The longitudinal stress originates from the distortion of the tyre, pressed against the ground by the gravitational force (Milliken and Milliken 1995). Because of this distortion, the distance of the tyre tread from the wheel hub decreases while approaching the centre of the footprint. This causes the linear velocity of the tyre tread to decrease accordingly. A decrease of the linear velocity means that the tread is subjected to compression, resulting in shear stresses in the tread (road to tyre). While moving away from the centre of the footprint, the distance between the tyre tread and the wheel hub increases and the stress reverses. Because of the distortion in the tyre due to the gravitational force, the effective perimeter of the tyre while rolling can be quite different from the circumference of the tyre when no force is applied to it. For this reason it is common to differentiate between the **undeflected wheel radius $\mathbf{R_w}$** and the **effective wheel radius $\mathbf{R_e}$**. The effective radius is defined as the forward speed of a free-rolling tyre (equal to the vehicle speed V_v) divided by the free-rolling tyre angular speed Ω_0, as described by Equation 2.1 (Pacejka 2005).

$$R_e = \frac{V_v}{\Omega_0} \tag{2.1}$$

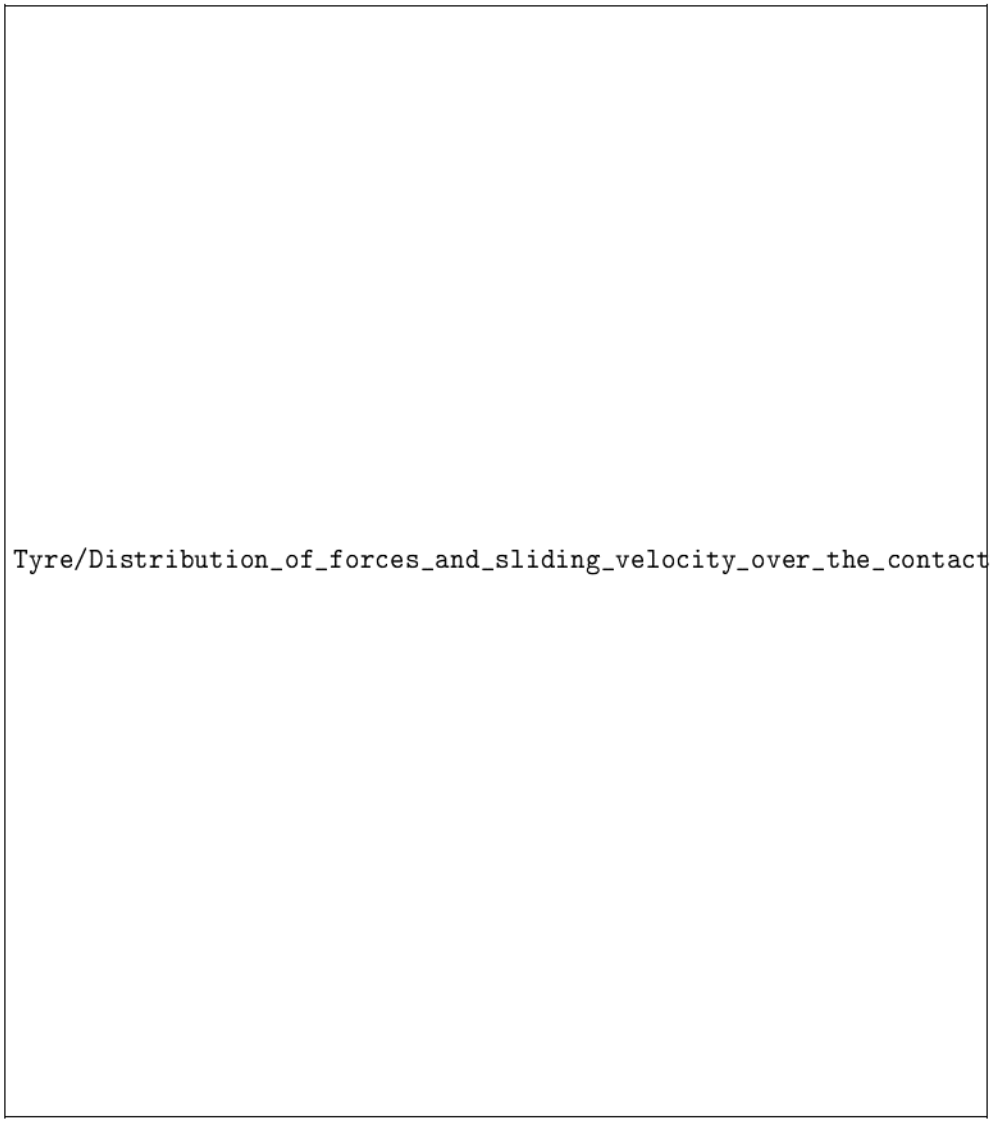

Figure 2.2: *Distribution of forces and sliding velocity over the tyre footprint (National Highway Traffic Safety Administration 1981)*

Now that the longitudinal stress in a free-rolling tyre has been discussed, I will analyse the longitudinal stress due to the application of torque to the wheel. This is described by curve 2 in Figure 2.2. First of all, it is important to understand that a driving torque applied to the wheel compresses the tread in front of the footprint (compare C_1 and C_2 in Figure 2.2). The compressed elements then enter the footprint, resulting in a shear force in the tyre that grows linearly while proceeding in the footprint. In the proximity of the trailing edge of the footprint the normal load quickly decreases, allowing the tread to slide on the ground in order to release the piled shear stress (Wong 2008).

The sum of the stresses due to the gravitational force and the driving torque is described by curve 3 in Figure 2.2. The same figure illustrates the variation of the linear velocity of the tyre along the footprint. Before reaching the

ground the tread starts to compress, reducing its speed. After the tread enters the footprint, the normal force keeps the compressed tread in adhesion with the ground. For this reason, the linear velocity remains constant, although lower than the uncompressed part. While the longitudinal stress increases, some sliding occurs to relax the compressed tread causing a slight increase in the speed. After leaving the footprint the tread stretches further to recover the original shape and the uncompressed speed. Because of the compression in the tread, more revolutions are needed to cover the same distance when a driving torque is applied to the wheel (Milliken and Milliken 1995). This effect is quantified by the **longitudinal slip velocity** $s = \Omega - \Omega_0$, although it is common to consider its normalised versions: the slip ratio. There are several definition of slip ratio. As mentioned in Chapter 1, in this thesis I am going to use a separate convention for acceleration and braking. The adopted convention is defined in Equation 2.2.

$$\begin{aligned} &\text{for acceleration,} && \Lambda_t = 1 - \frac{V_v \cos\alpha}{\Omega R_e} \\ &\text{for braking,} && \Lambda_b = \frac{\Omega R_e}{V_v \cos\alpha} - 1 \end{aligned} \tag{2.2}$$

Equation 2.2 is a generic definition, applicable when lateral force is developed in addition to the longitudinal force. In absence of lateral forces acting on the tyre, $\alpha = 0$ and $\cos\alpha = 1$. During free-rolling $\frac{\Omega R_e}{V_v \cos\alpha} = \frac{V_v \cos\alpha}{\Omega R_e} = 1$ and the slip ratio is null. During locked braking $\frac{\Omega R_e}{V_v \cos\alpha} = 0$ and the slip ratio is -1. During spinning $\frac{\Omega R_e}{V_v \cos\alpha}$ tends to $+\infty$ when the longitudinal tyre force is not enough to move the vehicle (this could happen uphill, for example). Under this condition $\frac{V_v \cos\alpha}{\Omega R_e}$ tends to zero and the slip ratio is +1.

The longitudinal force generated at the interface between the tyre and the ground is strongly dependent on the slip ratio as well as the normal force applied to the ground. The friction with the ground is dependent on the normal force, because the normal force increases the interference between the tyre and the ground by pressing the two surfaces against each other. As a first approximation, it is possible to assume that the maximum longitudinal force is directly proportional to the normal force applied to the ground (this is how I have intentionally simplified this topic in Section 1.3). In reality the maximum longitudinal friction coefficient changes slightly with the normal force. In particular it is higher for lower normal loads. Figure 2.3 shows some data taken at the Highway Safety Research Institute, University of Michigan (Ervin,

Figure 2.3: *Longitudinal friction coefficient vs slip ratio for different normal loads; data taken at the Highway Safety Research Institute, University of Michigan (Ervin, Macadam, and Fancher 1975)*

Macadam, and Fancher 1975). These data depict the normalised friction characteristic for different values of normal force. Figure 2.3 shows a variation in the normal force of about 400%, corresponding to a variation in the longitudinal friction coefficient of merely 20%. It is therefore reasonable to consider a constant longitudinal friction coefficient in spite of small variations in the normal force.

The friction characteristic can be divided into three regions, according to the physical effect dominating the tyre operation: elastic region, transitional region and frictional region. At low slip ratios, the elastic compression of the tyre is the dominant effect because a large area of the footprint is in contact with the ground. The elastic force grows linearly with the compression, and the compression is the main cause of the slip velocity. For this reason, the longitudinal tyre force increases linearly with the slip ratio. This is the elastic region of operation of the tyre. In this region, the coefficient between the longitudinal tyre force and the slip ratio is defined as the **longitudinal tyre stiffness** and it corresponds to the initial slope of the longitudinal friction characteristic. By multiplying the characteristics in Figure 2.3 by the respective normal force, it would be possible to observe the respective non-normalised friction characteristics and it would clearly appear that the longitudinal stiffness (which depends on the tyre force, and not the friction coefficient) increases with the normal load. This is generally true because, for a given inflation pressure, the contact length grows with the normal force, and a longer footprint generates a higher elastic force for the same compression (simply because there is more

rubber to oppose to the deformation) (Wong 2008).

With the increase of the longitudinal force, a larger fraction of the footprint starts sliding on the ground. This is because the force generated by the tyre deformation overcomes the static friction with the ground. This is the transitional region of operation of the tyre, where both the elastic force and the frictional force have an important effect. When most of the contact patch is sliding on the ground, the tyre enters in the frictional region, where tyre operation is dominated by the frictional force. This region begins with the longitudinal friction characteristic reaching the peak value. In the frictional region, the sliding is the major cause of slip velocity. With the increase of the slip velocity, the friction with the ground decreases (partly because the static friction is larger than the dynamic friction). This causes the longitudinal tyre force to decrease monotonically and with a non-linear behaviour. This region corresponds to an unstable operating area, with the wheel that accelerates because of the reduction of grip, causing the slip ratio to grow and further reducing the longitudinal force attainable. For large values of slip ratio, the longitudinal friction coefficient tends to settle to a value significantly lower than the maximum one.

Figure 2.4 shows the normalised friction characteristic under different road conditions. The data are produced by the Highway Safety Research Institute (Fancher et al. 1970). These data show that the maximum value of the longitudinal friction coefficient could change significantly from dry to wet conditions, depending on the structure of the road. This effect is even more pronounced when icy and snowy conditions are considered (Wong 2008). Because these changes directly affect the performances of the car under braking and acceleration, limiting safety-critical manoeuvres, it is important to constantly monitor the changes in the road condition. This the main motivation for my thesis, which proposes a technique to quantify the longitudinal friction with the road. As Figure 2.4 also shows, it is not uncommon for the slip ratio associated to the maximum friction coefficient to change value according to the road condition. For this reason, in order to provide the maximum driving performance, the slip ratio has to be constantly controlled at its optimal value. The detection of changes in the road condition and the control of the slip ratio around its optimal value are both addressed in this thesis and they will extensively discussed in Chapter 5.

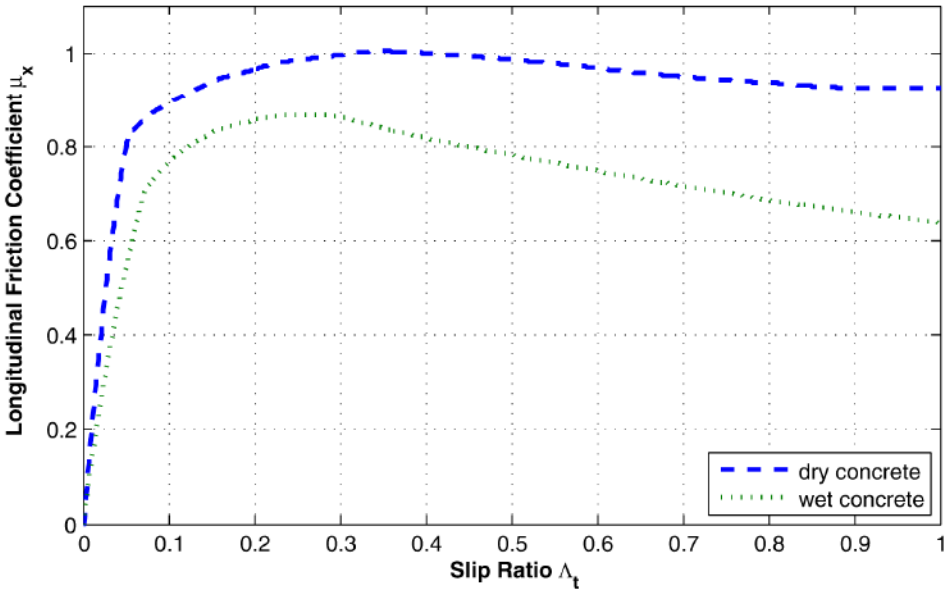

Figure 2.4: *Longitudinal friction coefficient vs slip ratio for different conditions of the road; data taken at the Highway Safety Research Institute, University of Michigan (Fancher et al. 1970)*

2.4 Lateral Force

I have previously introduced several concepts that will be extensively used in the continuation of the thesis. The content of the remaining sections in this chapter will be less critical for the understanding of the whole thesis. Nonetheless, these sections will provide a general overview of the tyre behaviour, which is needed to apply the theory presented in this thesis to the various driving situations in real life. In addition, these sections will provide further evidence for the purpose of my thesis.

I defined before the lateral tyre force as the force applied to the wheel along the y axis. I will first analyse the behaviour of the tyre in a vertical position, when the inclination angle γ is zero. The effects of the inclination angle on the lateral force will be discussed later on. By considering a widely adopted tyre model (Milliken and Milliken 1995), consisting of a flat rubber sheet between two metal discs, it is easy to understand the behaviour of the tyre under lateral force. The behaviour of such tyre model is illustrated in Figure 2.5.

I will start by looking at a stationary wheel, pressed against the ground by a force normal to the surface. Applying a small lateral force to the centre of the wheel, the rubber bends laterally until the elastic force balances the applied lateral force. This situation is illustrated in Figure 2.5 by the side view, the rear view and the initial position of the wheel in the bottom view. Increasing the lateral force, the lateral deflection grows proportionally until it overcomes the maximum frictional force offered by the ground (for a given

Figure 2.5: *Behaviour of the tyre when lateral force is applied (Milliken and Milliken 1995)*

normal force). At this point the rubber starts to slide on the ground surface. The **lateral tyre stiffness** is defined as the amount of elastic force generated for a given deflection. It is measured as a spring rate, in N/m. For the considered tyre model, the lateral stiffness reduces as the diameter of the metal discs reduces (for the same diameter of the wheel), because smaller discs leave exposed a larger area of the rubber sheet. With a larger area exposed to deformation, the same elastic force can be distributed over a longer path, the local stresses are therefore reduced and the lateral displacement is increased. The lateral stiffness of the tyre model can also be increased by using a stiffer rubber compound. In a real tyre, the width of exposed area of the rubber sheet corresponds to the height of the tyre. For a given height of the tyre, the lateral stiffness is mainly affected by carcass structure, rubber compound and

inflating pressure.

I will now consider the effect of rolling the wheel while maintaining a lateral force on it. As I will explain in Section 2.5, a slight moment of force around the z axis is needed in order to keep a constant heading direction of the wheel. Under these conditions, the wheel follows a direction which deviates from the wheel heading by a slip angle α. This is clearly shown in the bottom view of Figure 2.5. This phenomenon is due to the lateral deflection of the tyre caused by the lateral force. While the wheel is rotating, the points of the tyre laterally displaced from the footprint will gradually come in contact with the ground, maintaining the same orientation of the tyre deflection. The lateral stress increases while moving forward in the footprint, until the frictional force offered by the ground can no longer maintain the distortion. At this point the lateral stress is released with the thread sliding back towards the wheel plane. It is important to notice that this effect is usually limited to the narrow trailing edge, where the normal force is low compared to the centre of the footprint.

The lateral deformation of the tyre is important because it produces the lateral force required by any ground vehicle to manage a turn. The maximum lateral deformation is limited by the grip with the ground, which depends on the characteristic of the ground and the force pushing the tyre against the ground (the normal force). Figure 2.6 shows in detail how the lateral stresses are distributed along the tyre footprint.

Helped by Figure 2.6, I will analyse how the lateral deformation of the tyre generates lateral force. Point A represents the leading edge of the footprint. The deformation of the carcass above the footprint causes the point A to be laterally displaced from the wheel centre plane, by a distance ν. At the point A the tyre is just starting to be in contact with the ground and therefore the normal force is very low.

Moving along in the footprint, the normal force increases rapidly keeping the tyre in complete adhesion with the ground. Until the point B, in fact, the footprint follows the direction of the velocity vector V of the wheel. The last plot of Figure 2.6 shows the lateral velocity of the points in the footprint, referred to the velocity of the wheel centre plane. The points between A and B have a constant speed $V_d = V \sin \alpha$, which is the speed of the ground referred to the wheel centre plane. The other points are actually moving with respect to the ground. The deformation of the tyre increases linearly between A and B, together with the lateral stress.

The point H is the point stretching furthest from the wheel centre plane and therefore it corresponds to the point of maximum lateral stress. The points between H and D, which experienced beforehand the maximum lateral stress,

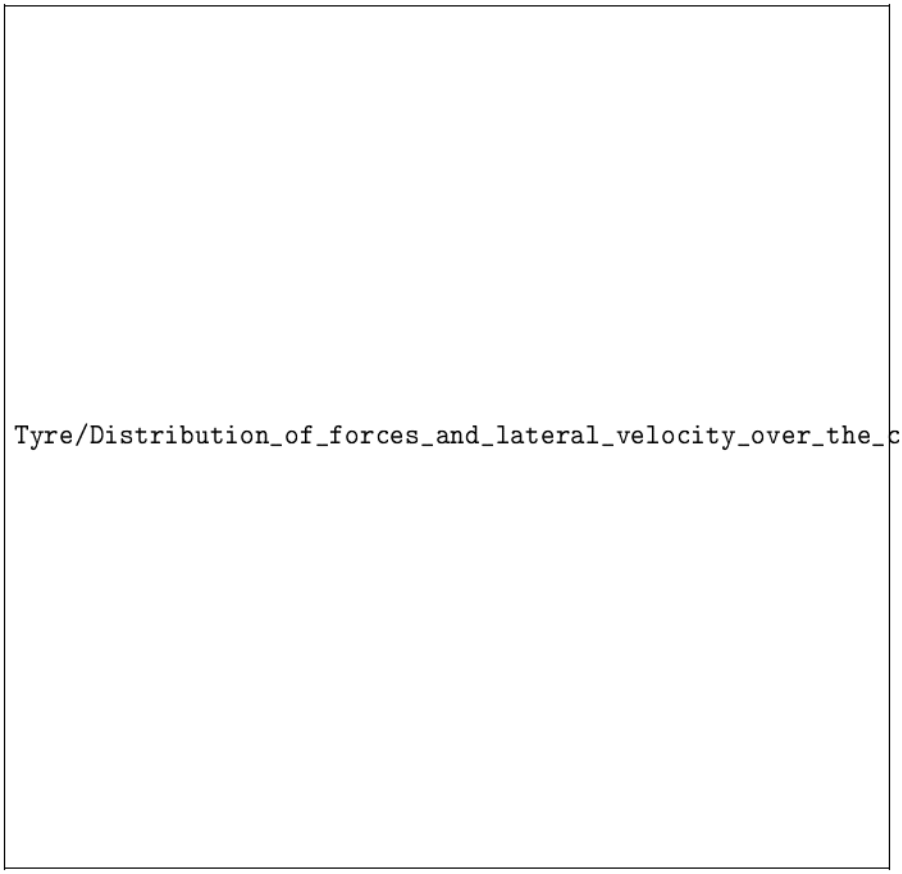

Figure 2.6: *Lateral stress and lateral velocity over the tyre footprint (National Highway Traffic Safety Administration 1981)*

were pushed by the rotation of the wheel to overcome the frictional force with the ground. Now they are sliding on the ground towards the wheel centre plane, pulled by the elastic force of the tyre. The sliding is helped by the fact that the normal force is reduced towards the trailing edge of the footprint, which lowers the reaction force from the ground.

Because of the stiffness of the tyre, the point farthest apart from the wheel centre plane (point H) is pulled towards the centre plane by the trailing edge of the footprint, which is sliding on the ground. This is the reason why all the points between B and H are also sliding, although their lateral stress is still below the maximum reaction force offered by the ground. The lateral velocity of these points referred to the wheel centre plane is reduced from V_d until it reaches 0 at the point H. The points from H to D have a negative velocity, because they are sliding towards the wheel centre plane.

Along the footprint the lateral deformation is distributed between the carcass of the tyre and the tread rubber. Figure 2.6 highlights the deformation of the tread rubber. In particular, the rubber in contact with the ground follows the path ABHD while the rubber in contact with the carcass of the tyre follows

the path AED. It is obvious that outside the footprint, when the tyre is not in contact with the ground, the carcass is the only element of the tyre to sustain the deformation.

Looking at the distribution of lateral force, it is easy to see that the barycentre of lateral force (application point of the aggregate lateral force F_y) falls behind the centre of the footprint. This causes a moment of force which tends to align the wheel to the lateral force applied to it. This effect will be extensively discussed in Section 2.5. The distance between the centre of the contact patch and the barycentre of the lateral force is called **pneumatic trail**. Multiplying the pneumatic trail with the lateral force returns the **tyre aligning torque**.

I have previously explained that the lateral force generated by the tyre is directly related to the slip angle at which a tyre rolls. The relation between lateral force and slip angle is called **lateral friction characteristic** (*lateral* will be omitted when implied by the context). I also mentioned that the maximum lateral force that can be produced by the tyre is affected by the grip with the ground, which ultimately depends on the normal force applied to the ground. I will now discuss how the lateral force changes with the slip angle and the normal force. As a first approximation, it is possible to assume that the maximum lateral force is directly proportional to the normal force applied to the ground. For this reason it is meaningful to define the **lateral friction coefficient** μ_y as the ratio between these two values. This is expressed by Equation 2.3.

$$\mu_y = \frac{F_y}{F_z} \tag{2.3}$$

The relation between lateral friction coefficient and slip angle is called **normalised lateral friction characteristic**. In reality the maximum lateral friction coefficient changes slightly with the normal force. In particular it is higher for lower normal loads. Figure 2.7 shows some data taken at the Japan Automobile Research Institute (Sakai 1981). These data depict the normalised friction characteristic for different values of normal force. Figure 2.7 shows a variation of the normal force of about 300%, corresponding to a variation in the lateral friction coefficient of roughly 15%. It is therefore reasonable to consider a constant lateral friction coefficient in spite of small variations in the normal force.

This behaviour is very similar to the case of the longitudinal friction coefficient. Also the same regions of tyre operation can be identified. At low slip angles, the elastic deformation of the tyre is the dominant effect because a large area of the footprint is in contact with the ground. The elastic force

Figure 2.7: *Lateral friction coefficient vs slip angle; data taken at the Japan Automobile Research Institute (Sakai 1981)*

grows linearly with the lateral deformation, which is the only cause of slip angle. For this reason the lateral force increases linearly with the slip angle. The coefficient between these two values is the lateral tyre stiffness and it corresponds to the initial slope of the lateral friction characteristic. By multiplying the characteristics in Figure 2.7 by the respective normal force, it would be possible to observe the respective non-normalised friction characteristics and it would clearly appear that the lateral stiffness (which depends on the tyre force, and not the friction coefficient) increases with the normal load. This is analogous to the behaviour of the longitudinal tyre stiffness, as discussed in Section 2.3. While the general rule is that the lateral stiffness increases with the normal load, this is not true when the normal load becomes so high to cause a significant deformation of the tyre shoulder.

With the increase of the slip angle, a larger area of the footprint starts sliding on the ground. This happens in a transitional region where both the elastic force and the frictional force have an important effect. When most of the contact patch is sliding on the ground, the tyre operation is dominated by the frictional force. The frictional region begins with the lateral friction characteristic reaching its peak value. In the frictional region the sliding is the major cause of slip angle. Because the tyre is mainly sliding on the ground and the frictional force does not depend on the direction of sliding (Hall and Davis 1965), the lateral force changes very little with the slip angle. In the frictional region the lateral force is basically not controlled. The control is restored when the slip angle is reduced and the tyre operation is brought back

into the transitional or the elastic region. Under this operating condition, the sliding of the tyre is reduced and a larger part of the footprint is able to follow the slip angle with rolling and lateral deformation.

The similarities between the lateral friction characteristic and the longitudinal friction characteristics allow similar techniques to be used for their estimation, as well as similar procedures to control slip angle and slip ratio. This is particularly interesting because very few techniques for slip angle control have been developed. Until now, in fact, the control of the slip angle has been mostly reserved to the driver without electronic intervention, but this might soon change. Due to the improved reliability of automotive electronics, more and more automated procedures are assisting the driver (see Chapter 1). In Chapter 5 I will propose a technique for the estimation of the longitudinal friction characteristic that could be easily modified in order to estimate the lateral friction characteristics. My project is well suited for this application because it is based on an autonomous vehicle with electric steering control (developed by me and extensively presented in Chapter 4). Such a vehicle offers all the hardware needed to implement an automatic control of the slip angle, which could be a natural development for the future of the project.

I have mentioned before how the lateral force changes with the normal load: the frictional force is roughly proportional to it and the lateral stiffness generally increases with the normal load. When high performances are required however, the details of the load sensitivity become crucial for the handling of the car. Figure 2.8 shows some data taken at Delft Vehicle Research Laboratory (National Highway Traffic Safety Administration 1981), for a tyre rolling at a constant speed of 30 km/h. These data demonstrate that in real conditions the linearity between the lateral force and the normal force is less than ideal. In particular, the slope of the characteristic between the two is monotonically decreasing. This means that any increase of the lateral force with the normal load is always slightly lower than what a linear progression would be. This deeply affects the handling of the vehicles when the mass increases. In fact, while in racing cars most of the normal load is due to aerodynamic downforce, in passenger cars this is mainly associated to the gravitational force, which is proportional to the vehicle mass. The lateral force required to manage a curve at a certain speed is also proportional to the vehicle mass. While both the normal load and the lateral force required to manage a curve grow linearly with the vehicle mass, the lateral force generated at the tyres grows slightly less. This is a crucial reason why, from the handling point of view, the vehicle mass should be kept as low as possible.

The load sensitivity of the tyres also explains why a vehicle with weight equally distributed over the tyres provides better cornering performances than

Figure 2.8: *Normal load sensitivity for the lateral force; data taken at Delft Vehicle Research Laboratory (National Highway Traffic Safety Administration 1981)*

a vehicle with unequally distributed weight. A linear relationship between the lateral force and the normal load would in fact allow the weight to be distributed between two tyres in any proportion, and the overall lateral force generated by the tyres would remain the same. Because the lateral force grows with the normal load slightly less than linearly, the overall lateral force generated by two tyres with equally distributed load is always higher than the overall lateral force generated by tyres unequally loaded.

Figure 2.8 shows that the non-linearity between the lateral force and the normal load is more noticeable at low slip angles. This is because at low slip angle the tyre is operating in the elastic range which is characterised by the lateral stiffness of the tyre. The latter, unlike the frictional force, is only loosely dependent on the normal load. As I previously mentioned, the lateral stiffness grows with the normal load because this increases the tyre footprint on the ground, but it reduces when the tyre shoulder is heavily deformed.

2.5 Aligning Torque

I introduced the pneumatic aligning torque while commenting on Figure 2.6. This is due to the uneven distribution of lateral force, with the elastic distortion increasing towards the back of the tyre. The barycentre of lateral force is located behind the centre of the footprint, giving rise to aligning torque. The distance between the centre of the footprint and the barycentre of force is the pneumatic trail.

Figure 2.9: *Aligning torque vs slip angle; data taken at the Calspan Tire Research Facility (Milliken and Milliken 1995)*

Figure 2.9 shows some data taken at the Calspan Tire Research Facility (Milliken and Milliken 1995). These data depict the aligning torque for different values of slip angle. For low values of slip angles, the torque increases roughly linearly. This is mostly because the lateral force grows linearly with the slip angle and the sliding part of the tread is really small, so that most of the footprint is elastically distorted. In this condition, the barycentre of lateral force is almost static. As the slip angle increases, the lateral force stops growing and a larger part of the tread starts sliding on the ground, shifting the barycentre of force forward in the footprint. As a result, the pneumatic trail is reduced as well as the aligning torque. When the friction limit is reached, most of the tread is sliding and the aligning torque is around zero, if not even negative.

In addition to the pneumatic trail, there is another factor generating aligning torque: the **mechanical trail**. This is the distance between the steering axis and the centre of the footprint on a flat level road, measured on the road plane. The pneumatic and the mechanical trail together give the distance between the steering axis and the barycentre of lateral force. This distance is called **total trail**. The total trail multiplied by the lateral force returns the **steer torque**. While the mechanical trail is constant, the pneumatic trail varies with the slip angle providing information about the cornering operations. In particular, a rapid reduction of the steer torque means that the tyre is approaching the grip limit. Such observation suggests to limit the mechanical trail in order to use the aligning torque as an useful feedback of the grip

with the ground.

2.6 Combined Operations

In Section 2.3 and Section 2.4 I have separately analysed the longitudinal force and the lateral force generated at the interface between the tyre and the ground. These forces, however, are often present at the same time and they are coupled with each other. Both the tyre stiffness and the friction with the ground are reduced in one of the two directions (longitudinal or lateral) when a force in the other direction is applied to the tyre (Wong 2008). The friction with the ground is particularly interesting because it is the limiting factor in the total applicable force to the ground. Unlike the tyre stiffness, which is directionally dependent (anisotropic), the friction with the ground is mostly the same in every direction whenever the ground is a hard surface (Hall and Davis 1965). This information allows the establishment of a simple relationship between the maximum applicable longitudinal and lateral forces during combined operation. By representing the longitudinal and the lateral force as vectors on the road plane, this relationship can be visualised as a **friction circle** limiting the sum of the two forces with a value dependent on the **maximum friction coefficient** μ_{max} and the normal force F_z. Figure 2.10 shows two friction circles for a different value of the product $F_z\mu_{max}$. The total force F_{tot} represents the sum of the longitudinal and the lateral force, and it is limited by the biggest circle of radius 300 N. It is important to notice that sometimes the ground does not behave as a hard surface and its shape is altered by the passage of the tyre. If this is the case the friction is actually dependent on the direction of the displacement and the limit of the total applicable force is represented by a friction ellipse, with one of the two axis (longitudinal or lateral) slightly shorter than the other.

While the friction circle is useful to calculate the maximum value of longitudinal and lateral force for combined operation, it does not provide information about the combined operation within the frictional limit of the tyre. To understand the behaviour of longitudinal and lateral force for different values of slip ratio and slip angle it is necessary to analyse some of the few available experimental data. Figures 2.11 and 2.12 show some data taken at the Japan Automobile Research Institute (Sakai 1981). The normal load at the tyre is around 3920 N.

Figure 2.11 shows the characteristic between the longitudinal force and the slip ratio, for different values of slip angle. With the increase of the slip angle, the maximum longitudinal force is generally reduced. Moreover, the longitudinal tyre stiffness is reduced and a higher slip ratio is required to

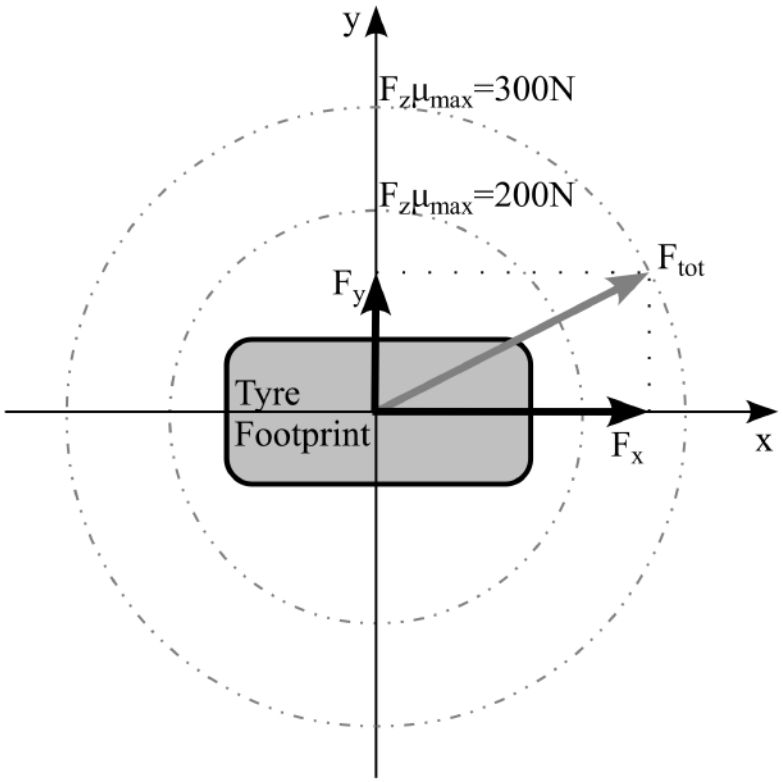

Figure 2.10: *The friction circle limiting the longitudinal and lateral tyre force*

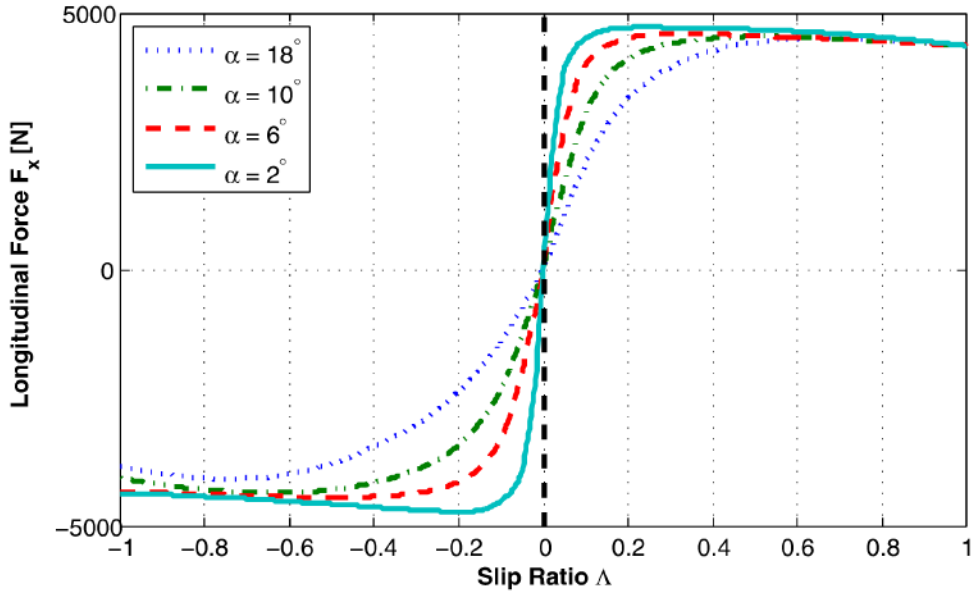

Figure 2.11: *Braking and traction forces vs slip ratio, for different values of slip angle; data taken at the Japan Automobile Research Institute (Sakai 1981)*

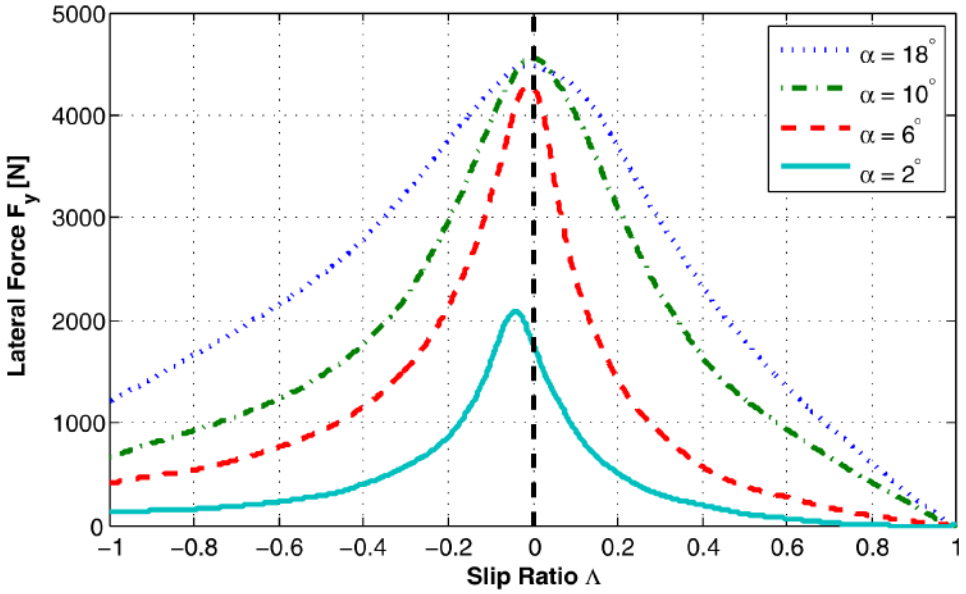

Figure 2.12: *Lateral force vs slip ratio, for different values of slip angle; data taken at the Japan Automobile Research Institute (Sakai 1981)*

generate the same longitudinal force.

Figure 2.12 shows the characteristic between the lateral force and the slip ratio, for different values of slip angle. As expected, with the increase of the slip angle the lateral force is also increasing. More interesting is the behaviour of the lateral force with the slip ratio. The lateral force monotonically decreases with the absolute value of the slip ratio, meaning that the cornering capabilities of a vehicle are strongly reduced when the wheels are skidding. Please note that the maximum value of lateral force for each curve might not coincide exactly with zero slip ratio, but this is not the real behaviour and it is only the result to the discrete number of measurement (and the noise in the measure) that are linked to form a complete characteristic. The behaviour of the lateral force with the slip ratio is possibly the most important reason to limit the slip ratio between 0 and the value that provides the maximum longitudinal force. Sometimes, when the maximum longitudinal force is obtained at a relatively high slip ratio (for example on ice), it might also be advisable to limit the longitudinal force to a value slightly lower, in order to maintain a good lateral control of the vehicle.

2.7 Inclination and Camber

In the previous sections I provided the basics to understand the effects of the slip ratio and the slip angle. To be thorough, I will use this section to present a parameter which is usually not controlled during driving, nonetheless it affects

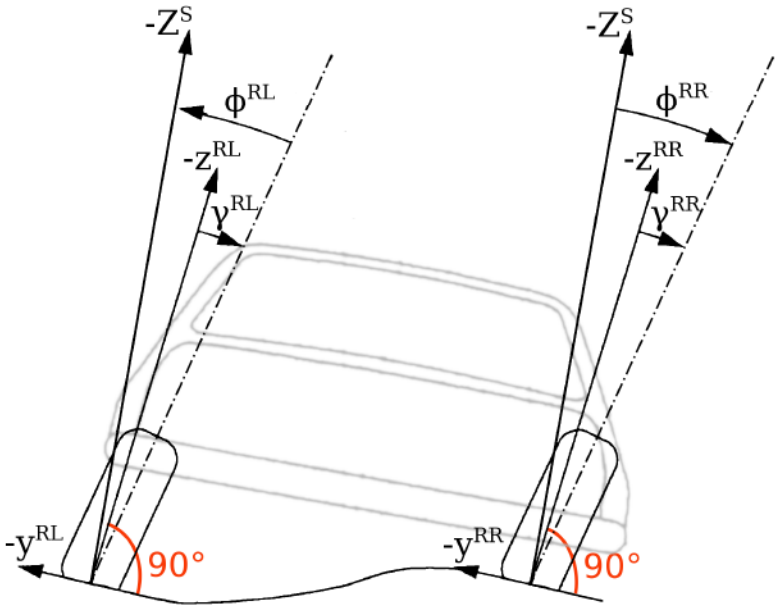

Figure 2.13: *Distinction between inclination and camber angle, for a ground surface which is not flat (Vehicle Dynamics Standards Committee 2008)*

the lateral force generated at the tyre. This parameter is the inclination angle γ, which is the angle between the wheel plane and the axis normal to the ground (the tyre z axis). The inclination angle depends on the curvature of the ground, the vehicle track and the position of the suspension. Because the inclination angle is not controlled by the driver and the curvature of the ground varies with the road, the vehicle design is usually focused on a related parameter, called **camber angle** ϕ. Figure 2.13 shows the distinction between inclination and camber for a generic ground surface. The camber is the angle between the wheel plane and the vertical axis of the sprung mass, indicated in this thesis with the capital Z (the superscript S might be used to indicate that it is referring to the sprung mass, as it is the case in Figure 2.13). In general the road ground is approximately flat, in which case the inclination angle and the camber angle coincide.

The camber cannot be controlled by the driver and it is usually set by design, although in some expensive sports cars it is possible to vary it with simple mechanical modifications. The aim of camber tuning is to use the tyre at the best inclination angle, on average, for a certain road. Without considering the tyre deformation due to the normal force, a free-rolling wheel with an inclination angle would revolve around a point, which is the intersection between the road plane and the wheel axis. This is clearly illustrated in Figure 2.14. In general, the wheel is forced to follow a straight path by the vehicle and this generates a distortion in the tyre tread. This distortion causes local stresses, that summed together are perceived as a lateral force in the direction

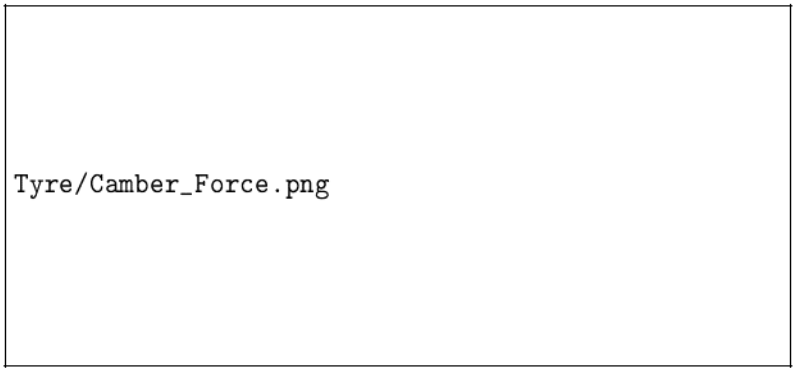

Figure 2.14: *Distortion of a free-rolling tyre with an inclination angle (National Highway Traffic Safety Administration 1981)*

of the tilt, called **camber thrust**.

A vehicle is generally designed to offer the same performances for left and right turns, therefore the camber angle of the wheels at the left side of the vehicle is opposite to the camber angle of the wheels at the right side. Under these conditions and with the weight equally distributed on both sides of the vehicle, the total lateral force due to the camber is zero. During cornering, however, the weight transfer towards the outside of the turn provides higher load to the outer wheels. If the top of the wheels is tilted towards the inside of the car, the outer wheels generate camber thrust towards the inside of the curve. Because of the difference in normal load between inner and outer wheels, the total lateral force due to the camber is directed towards the inside of the curve. This allows a greater cornering force for the same tyre slip angle, but also a higher peak of lateral force. Figure 2.15 shows some data taken at the Cornell Aeronautical Laboratory (Fonda 1956). These data report the peak lateral force for different values of camber, referring to a round slick tyre subject to a normal load of 4106 Nm. It is interesting to notice the slight increase in peak cornering force when the tyres are tilted towards the inside of the vehicle.

Because the elastic distortion due to the camber is symmetric to the centre of the footprint, the camber alone does not generate aligning torque. However the camber does affect the total aligning torque when some slip angle is applied. The asymmetry of the elastic distortion due to the slip angle is partially neutralised by the symmetry of the camber, resulting in a reduction of the total aligning torque with the increase of the camber angle.

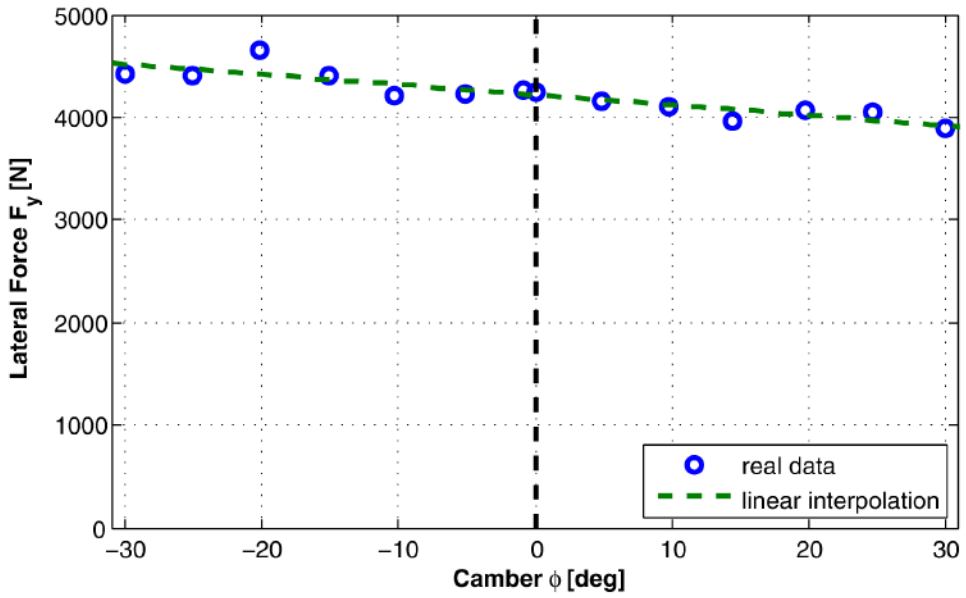

Figure 2.15: *Peak lateral force vs camber (the negative camber corresponds to the top of the wheels tilted towards the inside of the vehicle); data taken at the Cornell Aeronautical Laboratory (Fonda 1956)*

2.8 Summary

The aim of this chapter was to introduce the characteristics of the grip between the tyres and the ground. Because the grip is the limiting factor of the performances of any ground vehicle, the literature about this subject is particularly vast. For this reason, my review was not intended to be comprehensive and it was limited to a qualitative analysis. After presenting the conventions adopted in this thesis, I analysed the effects of normal force, slip ratio, slip angle and inclination angle on the grip between the tyre and the ground. I supported my analysis with experimental data selected from the available literature.

Introducing the optimal operating range for the slip ratio and the slip angle, I provided reasons for their continuous control during driving. I discussed the variation of the friction characteristics with the road condition, explaining the need for a continuous estimation of the grip with the ground. I stressed the importance of limiting the slip ratio, in order to provide longitudinal force while maintaining lateral stability. I highlighted the similarities between the longitudinal and the lateral friction characteristics, suggesting that similar techniques can be used for their estimation. In Chapter 5 I will recall much of this information to propose a novel technique to estimate the longitudinal friction characteristic.

Chapter 3

Vehicle Motion and Normal Force

3.1 Introduction

The aim of this chapter is to present the general model for the longitudinal motion of a vehicle, in order to prepare the reader for the simplified "Single wheel" model that will be used in Chapter 5. I will also analyse the measurable forces acting on the vehicle, proposing some techniques to estimate the forces whose measurement is more difficult. In particular, I will cover the topic of the estimation of the normal force at each tyre. This topic is complementary to the estimation of the longitudinal tyre force that will be covered in Chapter 5, in order to obtain valuable information about the friction characteristic of the ground. The normalised friction characteristic, in fact, is dependent on both the normal force and the tyre force, as covered already in Chapter 2. Finally, I will propose the use of an IMU to estimate the contribution of gravitational force and external forces to the longitudinal motion of the vehicle.

This chapter does not aim to present any original contribution. It is the result of personal considerations based on literature (always cited) and discussions with my supervisory team. The topics discussed are not the main focus of my research and, for this reason, I did not prepare an exhaustive literature review to defend a possible personal contribution. Nonetheless, I decided that a brief discussion on these topics was needed, because they are essential to produce a comprehensive framework for the estimation of the grip with the ground. The aim of this Chapter is to pave the way for a more rigorous analysis of these problems, possibly a future work for our ITS project. The topics introduced in this Chapter are particularly relevant for the implementation of the dynamic-control trajectory-planning unit discussed in Section 1.1.

3.2 Vehicle Axis System

The axis system used to describe the motion of the vehicle can be referred to a point fixed either to the ground or to the vehicle. In this thesis I will use an axis system fixed in the reference frame of the vehicle, as recommended by the SAE (Vehicle Dynamics Standards Committee 2008). The fact that

the axis system moves with the vehicle allows to assign to every component of the vehicle a coordinate that is constant or that varies in a narrow range (for components that are not rigidly linked to the body of the vehicle).

In general, a vehicle is not a rigid body and it is composed of different bodies moving independently. In a complex system like a car, the masses that are not rigidly connected to each other are numerous: vehicle body, engine, fuel, steering, suspensions, wheels and then of course the passengers and any additional load inside the car. Conventionally however, a road car is divided in only two masses: the mass that is not supported by the suspension is called **unsprung mass** and it is composed of the wheels, brakes and about half the mass of the connecting component (links, springs and dampers) while the remaining part is called **sprung mass** (Vehicle Dynamics Standards Committee 2008).

The vehicle axis system is usually referred to a reference point in the vehicle sprung mass, which is considered as a rigid body. In this thesis I will use the centre of gravity of the sprung mass (CG), determined in static conditions, as the reference point and the origin of the vehicle axis system. To distinguish the axes of the tyre axis system introduced in Chapter 2 from the axes of the vehicle axis system, I will reserve the lowercase letters x, y, z for the tyre axis system and I will introduce the uppercase letters X, Y, Z for the vehicle axis system.

The axis system is established on a vehicle travelling in a straight line on a level road at a constant speed. The X axis is oriented along the direction of motion, the Z axis is normal to the road plane and directed towards the ground while the Y axis is normal to the plane containing the X axis and the Z axis, and it is directed towards the right of the driver. The forces acting on the vehicle as well as the movements of the vehicle are decomposed along the axes of the vehicle axis system. In particular, the **longitudinal vehicle force $\mathbf{F_X}$** is the total force generated by the vehicle along the X axis, the **lateral vehicle force $\mathbf{F_Y}$** is the total force generated along the Y axis and the **normal vehicle force $\mathbf{F_Z}$** is the total force generated along the Z axis.

The angular movements of vehicle are also decomposed according to the vehicle axis system. In particular, **roll** is the movement of the vehicle around the X axis, **pitch** is the movement of the vehicle around the Y axis and **yaw** is the movement around the Z axis (Vehicle Dynamics Standards Committee 2008).

The **steering angle** is the average angle between the steering wheels (usually the two front wheels) and the longitudinal axis of the vehicle. Generally, it is controlled by the driver through a steering wheel, although in some cases,

such as the vehicle I developed for this project, it might be controlled by an electric motor. The **toe** is the angle that each wheel makes with the longitudinal axis of the vehicle, when the steering angle is null.

3.3 Equations of Longitudinal Motion

The longitudinal vehicle force is the total force generated by the vehicle along the longitudinal axis X. It corresponds to the total driving force, which is the sum of the longitudinal forces generated at each wheel. This is clearly expressed by Equation 3.1. F_X^{FL}, F_X^{FR}, F_X^{RL} and F_X^{RR} are the forces generated along the X axis, respectively at the front left wheel, the front right wheel, the rear left wheel and the rear right wheel.

$$F_X = F_X^{FL} + F_X^{FR} + F_X^{RL} + F_X^{RR} \tag{3.1}$$

For the continuation of this thesis I will assume that all the wheels are parallel to the direction of motion of the vehicle. This is roughly verified whenever the steering wheel is kept at its central position, if the toe of the vehicle is negligible. Under this assumption, the X axis of the vehicle corresponds to the x axis of each wheel, and the longitudinal forces of each wheel can be substituted into Equation 3.1. In order to make explicit the dependency of the longitudinal vehicle force on the slip ratio and the normal force, I will substitute the longitudinal forces at each tyre (expressed as a function of the slip ratio with $F_x(\Lambda_t)$) using Equation 1.1. The resulting relationship is expressed by Equation 3.2, where F_z^{FL}, F_z^{FR}, F_z^{RL} and F_z^{RR} are the normal forces at each wheel and Λ_{FL}, Λ_{FR}, Λ_{RL} and Λ_{RR} are the slip ratios of each tyre.

$$F_X = F_z^{FL}\mu_x(\Lambda_{FL}) + F_z^{FR}\mu_x(\Lambda_{FR}) + F_z^{RL}\mu_x(\Lambda_{RL}) + F_z^{RR}\mu_x(\Lambda_{RR}) \tag{3.2}$$

Another way of looking at the longitudinal vehicle force is to derive it from the driving torque, which is the only force generated directly by the vehicle. In particular, the force F_x at every tyre is the result of the driving torque applied to the respective wheel minus the inertial torque of the wheel, everything divided by the wheel radius R_e. The **inertial torque of the wheel** is defined as $I_y^w\dot{\Omega}$ where I_y^w is the **moment of inertia of the wheel** around the hub. Assuming that every wheel has the same moment of inertia I_y^w and the same radius R_e, the relationship between the longitudinal force of the vehicle

and the driving torque applied to each wheel is expressed by Equation 3.3. T_{FL}, T_{FR}, T_{RL} and T_{RR} are the driving torque applied to each wheel, while $\dot{\Omega_{FL}}$, $\dot{\Omega_{FR}}$, $\dot{\Omega_{RL}}$ and $\dot{\Omega_{RR}}$ are the time derivatives of the speed of each wheel.

$$F_X = \frac{T_{FL} - I_y^w \dot{\Omega_{FL}} + T_{FR} - I_y^w \dot{\Omega_{FR}} + T_{RL} - I_y^w \dot{\Omega_{RL}} + T_{RR} - I_y^w \dot{\Omega_{RR}}}{R_e} \tag{3.3}$$

The longitudinal vehicle force is opposed by the inertia of the vehicle and the external force acting on the vehicle. The **external force F_{ext}** includes the aerodynamic resistance, the rolling resistance and the gravitational force along the X axis. The **inertial force of the vehicle** is defined as $m\dot{V_v}$, where m is the **mass of the vehicle** and $\dot{V_v}$ is the time derivative of the vehicle speed, in other words the acceleration of the vehicle.

$$F_X = m\dot{V_v} + F_{ext} \tag{3.4}$$

Equations 3.2 and 3.4 provide the relationship between the slip ratio at each wheel, the normal force at each wheel and the longitudinal motion of the vehicle. These equations of motion will be the starting point of Chapter 5, in order to build a simplified "Single wheel" vehicle model.

3.4 Estimation of Normal Force

In Chapter 5 I will propose a novel technique to estimate the longitudinal tyre force. The knowledge of the applied longitudinal tyre force is fundamental to estimate the grip offered by the ground, however it is not sufficient on its own. As discussed in Section 2.3, the longitudinal tyre force is the product of the longitudinal friction coefficient, which is a measure of the grip with the ground, and the normal force applied to the ground. A first approximation of the normal force is to assume a constant value during the motion of the vehicle. Without considering aerodynamic effects that, in the normal direction, are usually negligible in passenger vehicles (but not in racing cars), the normal force is, on average (excluding transients due to irregularities of the road), due solely to the gravitational force between the vehicle and the ground. For this reason, the average normal force at each wheel can be measured in static conditions on a flat road. In dynamic conditions, however, the normal force can vary greatly due to the profile of the road, in the form of slopes, bumps,

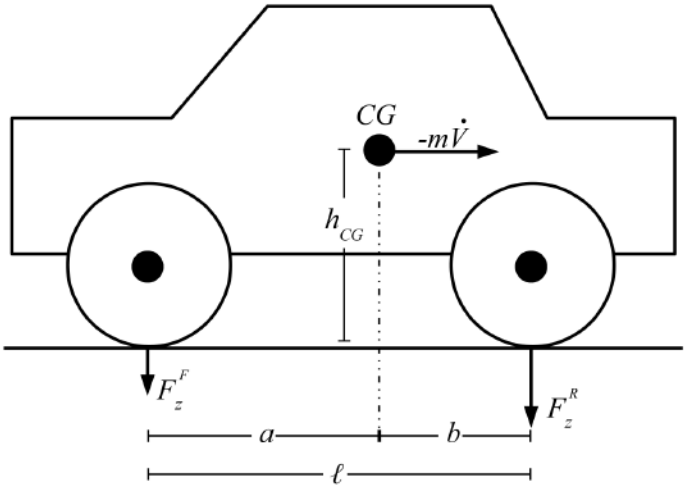

Figure 3.1: *Longitudinal load transfer*

crests, dips and so forth. Moreover, the normal load at the wheels is strongly affected whenever a force in the longitudinal or the lateral direction is applied to the sprung mass. In this section I am going to introduce briefly the problem of the estimation of the normal force, in order to offer a complete framework for the estimation of the ground characteristics.

3.4.1 Normal Force on a Flat Road

Every force acting on the centre of gravity of the vehicle in a direction parallel to the road plane will transfer normal load among wheels. In general, these forces can be classified into inertial forces and aerodynamic forces, although inertial forces are by far the most important in production vehicles. Inertial forces can be easily measured by knowing the acceleration of the vehicle. While lateral accelerations can only be measured using accelerometers, longitudinal accelerations can also be estimated from the speed of the wheels. The latter might differ slightly from the speed of the vehicle due to the slip ratio, however in Chapter 5 I will propose a novel technique that allows to estimate such a difference and that can be used to produce more accurate results.

Figure 3.1 illustrates the situation when the vehicle experiences an acceleration $\dot{V}_v$ along the X axis of the vehicle. Under this condition, the inertial force along the X axis is $-m\dot{V}_v$. The moment of force caused by the inertial force at the rear contact patch reduces the normal load at the front tyre by a value ΔF_z. This value is dependent on the inertial force, the height of the centre of gravity of the vehicle h_{CG} and the wheelbase of the vehicle ℓ, as expressed by Equation 3.5. Similarly, the normal load at the rear tyres in increased by the same value ΔF_z (Milliken and Milliken 1995).

$$\Delta F_z = \frac{h_{CG}}{\ell} m \dot{V}_v \tag{3.5}$$

In general, the wheelbase ℓ varies very little due to the suspension movements, therefore it can be considered a constant mechanical parameter of the vehicle. The same observation can be made for h_{CG}. For this reason, compensating for load transfer in the normal force is relatively easy and can be done in any mass-produced BEV, without requiring additional hardware.

3.4.2 Normal Force on Uneven Ground

The theory presented until here covers the behaviour of the vehicle on a flat road, but what happens when the road presents slopes, bumps, crests and dips? In this case it would not be possible to detect the normal force based on the longitudinal motion of the vehicle. In fact, a slope would be detected as a constant force against the motion, which can be confused with aerodynamic drag. Bumps, crests and dips instead would be detected as temporary losses of adhesion with the ground, which can be confused with variations in the ground condition.

In order to estimate the normal force at the tyres while travelling on uneven ground, it is necessary to measure somehow the vertical motion of the vehicle. A solution to estimate the normal force would be to measure the deformation of the tyre, at several points of the circumference of the tyre. A careful modelling of the deformation of the tyre could provide accurate results, however this technique requires the use of several sensors mounted on a rotating wheel. A reliable implementation would be a major engineering challenge, and would probably be very expensive. The tyre pressure could also be used to estimate the normal force, although the sensitivity of the tyre pressure towards the normal force is very low. In addition, the tyre pressure varies with temperature and location in the air chamber (considering the dynamic behaviour in a rotating wheel), therefore it would be very difficult to discern useful information from the pressure reading.

What I propose in this section is a technique to estimate the normal force by measuring the forces acting on each rigid body of the vehicle together with the acceleration of these bodies. Some forces will be measurable, some others will not. However, if it is possible to make reasonable assumptions over the forces that are not measurable, and the only unknown is the normal force acting on the ground, the estimation would be possible. It sounds much more complicated than it actually is, given that the forces acting on the vehicle are only a few, and that they act mostly in a specific direction.

The **gravitational force**, for example, is constant in magnitude and direction. It is always directed along the vertical and the vertical can be detected using an IMU on the sprung mass (more on this in Section 3.5). The magnitude of the gravitational force is determined by the mass m of the vehicle, which is easily measurable. The magnitude is always equal to mg. The **aerodynamic drag** is always directed against the direction of motion of the vehicle, which corresponds to the X axis of the vehicle (the vehicle will never move at a relevant speed in other directions, unless it is rolling over).

Now it is important to clarify a crucial point. The separate analysis of the longitudinal motion is, to my knowledge, always at the basis of the techniques for the estimate of the longitudinal tyre force, and the novel technique that I will propose in Chapter 5 is no exception. In some situations, however, the longitudinal motion of the vehicle cannot be separately analysed from the vertical motion because they are coupled with each other. This happens whenever the suspensions are designed to produce some components of force in the longitudinal directions, in response to a vertical force coming from the wheels. Although this is a quite common design in vehicles, the effects are usually minor and can be neglected. A more relevant situation is when the axis z of the tyre and the axis Z of the vehicle are not parallel, as shown in Figure 3.2. This is a frequent situation in off-road vehicles, in the presence of large obstacles in the path. Road vehicles, instead, are rarely facing a significant misalignment between the axis z of the tyre and the axis Z of the vehicle. Whenever this occurs, a correct estimation of the longitudinal tyre force requires a technique which takes into account the longitudinal and the vertical motion of the vehicle, as well as the coupling between them. This development is beyond the scope of my research, therefore I will limit my analysis to a vehicle whose suspensions move solely in the vertical direction, travelling on a road with a fairly smooth profile (so that the axis z of the tyre and the axis Z of the vehicle are almost parallel).

After clarifying the limitations of my analysis, I can proceed with the estimation of the normal force. First, because the aerodynamic drag is only acting along the longitudinal direction, I do not have to consider it further. Equation 3.6 summarises the forces acting on each wheel along the Z axis. They are the normal force F_z and the suspension unit force F_Z^{SU}, which is a function of the suspension unit extension p^{SU} and its derivative and double derivative over time, $p^{\dot{S}U}$ and $p^{\ddot{S}U}$ respectively. The difference between the normal force and the suspension unit force is the inertial force $m^w a_z^w$, where m^w is the mass of the wheel and a_z^w is the acceleration of the wheel along the Z axis, referred to an inertial reference frame. This means that a_z^w includes the contribution of the gravitational acceleration along the Z axis of the vehicle.

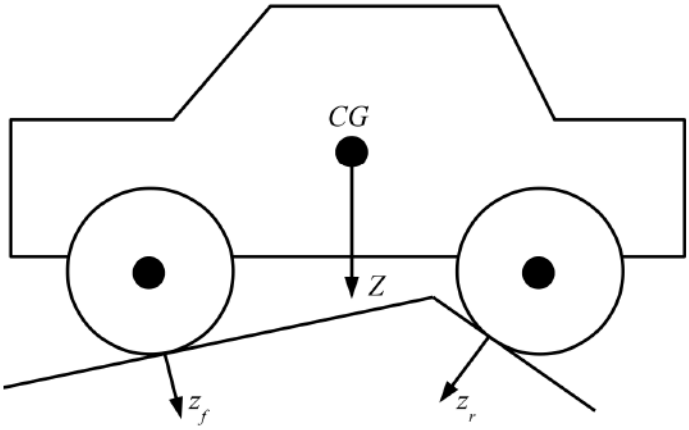

Figure 3.2: *Example of road profile producing a misalignment between the axis z of the tyre and the axis Z of the vehicle*

$$F_z = F_Z^{SU}\left(p^{SU}, p^{\dot{S}U}, p^{\ddot{S}U}\right) - m^w a_z^w \tag{3.6}$$

According to Equation 3.6, in order to estimate the normal force I need a measurement of the inertial force as well as the suspension unit force. The characteristic $F_Z^{SU}\left(p^{SU}, p^{\dot{S}U}, p^{\ddot{S}U}\right)$ describes the behaviour of the suspension unit. It could be close to a linear characteristic but in general it is not. In both cases, the characteristic needs to be measured experimentally, either by measuring the parameters of the linear function, or by building a look-up table of values for different positions, speeds and accelerations of the suspension unit. Once this is done, the only possible way to measure the force generated by the suspension unit force is to monitor its extension with a potentiometer and to use it as an input for the measured characteristic $F_Z^{SU}\left(p^{SU}, p^{\dot{S}U}, p^{\ddot{S}U}\right)$.

In order to measure the inertial force I need a measurement of the wheel acceleration (inclusive of the gravitational acceleration) along the Z axis. Potentially, the wheel acceleration could be measured by accelerometers attached to each hub of the vehicle. Instead I will propose a more centralised solution, which takes advantage of the measurements of the suspension unit extension, needed anyway to calculate the suspension unit force. These measurements provide information about the relative motion of the wheels in respect to the sprung mass. Thanks to a refined IMU, which could be comfortably located on the sprung mass of the vehicle, it would be possible to obtain an accurate measurement of the position and the orientation of the sprung mass, therefore defining the absolute motion of it. The absolute motion of each wheel could then be calculated from the relative motion between the wheel and the sprung mass and the absolute motion of sprung mass.

3.5 Inclination of the Vehicle and External Forces

In Section 3.4 I have repeatedly referred to the use of an IMU to track the gravitational force as well as the orientation of the vehicle. In this section I am going to discuss how this could be implemented, and how this information could be used to estimate the external forces acting on the vehicle along the X axis.

In the previous sections I derived the basic relationships between driving torque, external force, normal force, wheel speed, vehicle speed, slip ratio, road characteristic and the mechanical parameters of the vehicle. It is appropriate to evaluate which of these values is easily measurable and which one is not. I have mentioned how the torque generated by electric motors is easily measurable without the need for specific hardware, therefore I will assume it to be a known variable in any BEV. The external force is not measurable on its own, because it can have multiple origins (gravitational, frictional, aerodynamic) and it can act on multiple locations in the vehicle. In this section I will propose a solution to estimate the external force. Regarding the normal force, I have extensively covered the topic of its estimation in Section 3.4. The wheel speed is measured on every vehicle equipped with ABS, which is currently the vast majority of the vehicles on the market. For this reason, I will consider the wheel speed to be a known variable of the system. At the current time, very few vehicles integrate a direct measure of the vehicle speed and in this section I will discuss the limitations of each measurement technique. I will cover the estimation of the slip ratio and the road characteristic in Chapter 5. The mechanical parameters are easily measurable and I will always consider them to be known.

According to Equations 3.3 and 3.4, the external force can be calculated by knowing the torque applied to each wheel and by measuring the rotational acceleration of the wheels and the longitudinal acceleration of the vehicle. This approach was presented in (Fujimoto, Fujii, and Takahashi 2007) where $\dot{V}_v$ was supposed to be measured by an accelerometer mounted along the longitudinal axis of the vehicle. Such an assumption holds well when the vehicle is running on an horizontal path with the accelerometer measurement not affected by the gravitational acceleration, however it is not correct when the vehicle is facing a slope. This is expressed by Equation 3.7, where acc_x is the reading of the accelerometer along the longitudinal axis and θ is the inclination angle of the road, as shown in Figure 3.3.

$$acc_x = \dot{V}_v + g \sin(\theta) \tag{3.7}$$

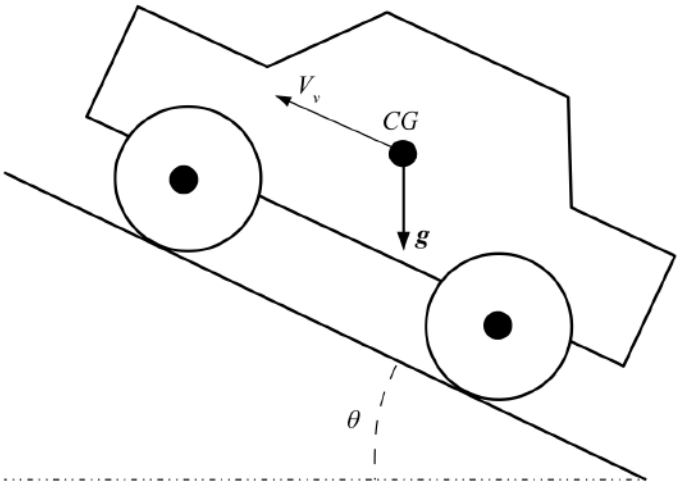

Figure 3.3: *Vehicle accelerating on a slope*

To estimate the external force in a general case a more complex approach is presented in this thesis. It involves the use of two accelerometers along the longitudinal and vertical direction of the vehicle, and a gyroscope measuring the pitch. The measurement along the vertical direction is not affected by the longitudinal acceleration but only by the slope of the road and the vertical oscillations due to the irregularities of the road. Such oscillations are in the relatively high frequency domain, depending on the suspensions and the mechanical parameters of the vehicle. In general they have a period smaller than a few seconds. In the low frequency domain, the reading $\boldsymbol{acc_z}$ of the vertical accelerometer is only dependent on the inclination angle $\boldsymbol{\theta}$, as expressed in Equation 3.8.

$$\boldsymbol{acc_z} = -\boldsymbol{g}\cos(\boldsymbol{\theta}) \tag{3.8}$$

It is important to notice the previous function is symmetric around $\theta = 0$, meaning it does not differentiate a climb from a downhill if they have the same slope. This makes it difficult to use the sole vertical accelerometer for the estimation of the gravitational acceleration. In the proposed approach, an initial angle $\boldsymbol{\theta_0}$ is calculated during the initialisation of the vehicle control, under the assumption that, at this stage, the vehicle is not moving. In this condition, the reading of the accelerometers along the longitudinal and the vertical direction of the vehicle can provide a reliable measurement of $\boldsymbol{\theta_0}$, as expressed by Equation 3.9.

$$\theta_0 = \arctan\left(\frac{acc_x}{-acc_z}\right) \tag{3.9}$$

The current angle θ is calculated from θ_0 by integrating with time the reading gyr_y of the gyroscope, as expressed by Equation 3.10.

$$\hat{\theta} = \theta_0 + \int_{t_0}^{t} gyr_y \, \mathrm{d}t - \Delta\theta_{LF} \tag{3.10}$$

The variable $\Delta\theta_{LF}$ is needed to correct inevitable errors. In fact, a small offset in the gyroscope output would generate an error growing linearly with the time, while a small error in the calculation of the initial angle would be carried over indefinitely. In order to correct these errors, I propose to use the reading of the vertical accelerometer to generate a low frequency indicator of the inclination angle. According to Equation 3.8, the vertical accelerometer can only measure the absolute value of the inclination angle, therefore the zero-crossing has to be determined by the gyroscope. Using this information, the corrective factor $\Delta\theta_{LF}$ can be obtained by filtering with a low-pass filter the variable $\Delta\theta$, calculated according to Equation 3.11.

$$\Delta\theta = \theta_0 + \int_{t_0}^{t} gyr_y \, \mathrm{d}t - sign\left(\hat{\theta}\right) \arccos\left(acc_z\right) \tag{3.11}$$

The proposed approach is very robust, and it only fails to converge when the initial angle is measured with the wrong sign and the angle never crosses the zero. In this case the solution would converge towards $-\theta$, deviating briefly from it while the angle is changing because of the integral in 3.10 but never enough to flip the sign. This situation is very unlikely as it requires an initial angle very close to zero, so that an error in the measurement can lead to a calculation of the initial angle with the wrong sign, and a slope that, despite starting very close to zero, deviates from it without ever crossing it again. The method proposed covers anyway a much wider scenario than the flat road assumed in (Fujimoto, Fujii, and Takahashi 2007).With the correct estimate of the road angle, the longitudinal acceleration of the vehicle can be calculated

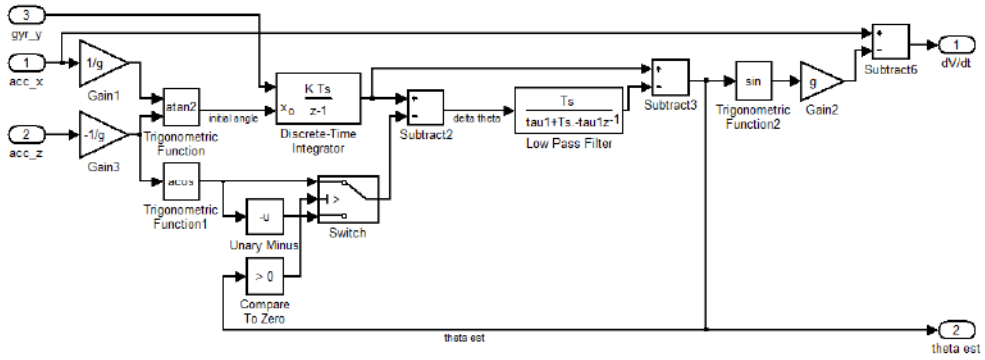

Figure 3.4: *The block diagram of the estimation of the road angle and the longitudinal acceleration*

according to Equation 3.12.

$$\dot{V}_v = acc_x - g \sin\left(\hat{\theta}\right) \tag{3.12}$$

As previously discussed, it would be finally possible to use the acceleration of the vehicle $\dot{V}_v$ to estimate the external force F_{ext}. The block diagram summarising the estimation of the road angle and the longitudinal acceleration is shown in Figure 3.4.

I have implemented the proposed estimation of the inclination angle and the longitudinal acceleration on the quad bike used for my project (I will provide more information in Chapter 4). Instead of discrete accelerometers, I have used an advanced IMU which integrates three accelerometers, three gyroscopes and three magnetometers. This unit is pragmatically located on the sprung mass in order to easily communicate with the vehicle control unit. In the future, the IMU could allow the calculation of the absolute acceleration and the absolute orientation in the three spacial dimensions.

3.6 Summary

In this chapter I have discussed the longitudinal and the vertical motion of the vehicle. I have presented the basic equations of longitudinal motion, which will be the foundation of my analysis in Chapter 5. I have introduced the problem of the estimation of the normal force, proposing different solutions based on the sensors available on the vehicle, in order to cover the whole range of driving conditions (from a flat horizontal road to off-road). Finally I have proposed a technique which uses an IMU to estimate the contribution of the gravitational

force on the longitudinal and the vertical motion. The same technique allows to estimate the overall contribution of external forces acting on the vehicle along the longitudinal direction.

The proposed estimation of the normal force has not been implemented on the vehicle platform used for the ITS project (the quad bike) for several reasons, mainly for lack of time and resources. Its implementation would have been particularly challenging because the two rear wheels are suspended together, and further studies would have been required. Nonetheless, I felt the need to briefly present some of the thoughts that has been addressed to this problem over the years, in order not to lose such information. In addition, I wanted to stress how a correct estimation of the normal force is crucial for the estimation of the ground condition, although this is often neglected in the relevant literature. The estimation of the gravitational force and the longitudinal acceleration has been implemented on the vehicle, with qualitatively successful results.

Chapter 4

Design and Development of Test Vehicle

4.1 Introduction

This chapter summarises the process of designing and building a vehicle in order to meet two challenging requirements:

- it should be suitable to validate the techniques of traction control discussed in the following chapters of the thesis
- it should be used as a platform for the whole Intelligent Transport Systems project, therefore it should be possible to control it remotely from a server while receiving a video stream from the cameras on the vehicle

This was one of the main targets of my PhD and it proved to be the most demanding task.

In the following chapters some algorithms to estimate the ground conditions will be introduced and their implementation will require a fast and precise control of the torque applied to each driven wheel. This is the reason why the vehicle has two electric motors independently controlling the two rear wheels. Such an architecture allows the distribution of torque across the two sides of the car, in order to control the heading of the vehicle. The use of an inertial measurement unit (IMU) provides information about the orientation and the movement of the vehicle.

Being used as a platform for the ITS project, the vehicle has to include all the equipment necessary to drive autonomously, which is the ultimate goal of the project. Together with cameras and a computer to process their data, the vehicle is provided with a system to control the steering and the propulsion through messages coming from a wireless network.

In this chapter the vehicle will be presented, with its mechanical architecture and electric components. The design of the software and the hardware used for the motor control will be described, together with the performance obtained. Whenever not specified, everything in this chapter is entirely my own contribution.

Figure 4.1: *The quad bike used for the ITS project*

4.2 The Quad Bike

The vehicle chosen for the aforementioned task was a full size electric quad bike. Such a vehicle is small enough to be driven almost everywhere in a university campus but big enough to host all the necessary equipment. The mechanical simplicity of the quad bike facilitates modifications of the chassis, leaving exposed all the hardware mounted on it. This makes it suitable to showcase all the technology integrated with the vehicle. The vehicle is powerful enough to carry a driver, allowing for collection of video data-sets or algorithm validation without the need for a fully-functional autonomous quad bike. The electric powertrain enables a fast and precise control of the torque provided to the wheels. This was a fundamental requirement for testing advanced traction control techniques on the vehicle.

The vehicle was bought in 2010 as a second-hand Global Electric Motorcars (GEM) Quadriga. Over the following two years, the vehicle has been completely modified. Figure 4.1 shows the quad bike as it is at the end of 2012. I contributed to most of the development of the vehicle, in particular:

- I selected the components for the electrical and the control system of the vehicle.
- I designed and wired the electrical system of the vehicle.

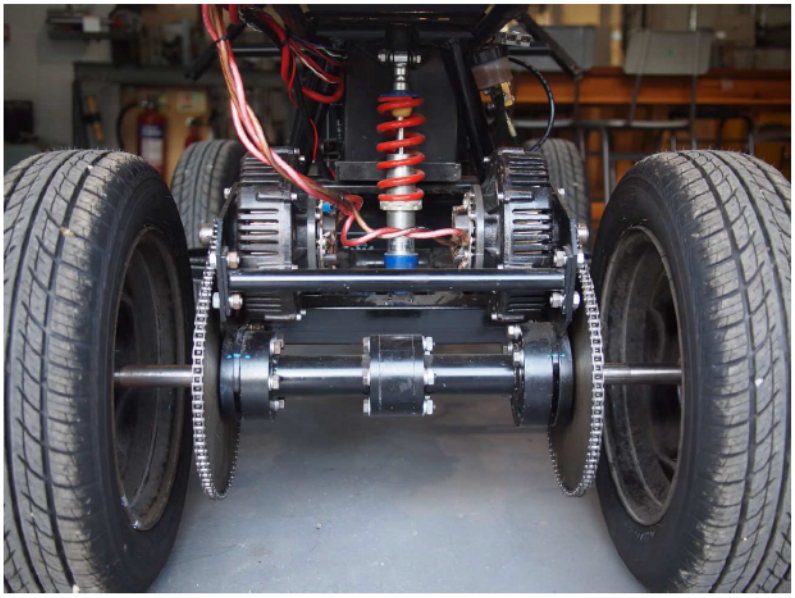

Figure 4.2: *The DC motors on the back of the quad bike*

- I designed the circuit board for the supply of the different voltages to the electrical system, the printed circuit board (PCB) to control the steering motor, the PCBs driving the traction motors and the connection board to route the input and the output wires to the right pin of the controller.
- I wrote the code controlling the vehicle.
- I selected the components in order the change the gearing between the motors and the wheels.
- I fixed all the components to the vehicle.

Hereinafter I am going to present the main components used on the vehicle, as well as the challenges I had to face in order to develop a reliable system.

At the centre of the quad bike there are five Lead Acid Batteries. Each one of them has a nominal voltage of 12 V and a capacity of 75 Ah. Four of them in series (48 V) are used to power the two traction motors and the steering motor, while the fifth is used for powering all the control circuitry.

The original single motor, fixed axle drivetrain has been completely replaced. Two electric motors were selected to independently drive the two rear wheels. Figure 4.2 shows the two motors installed on the quad bike. They are Perm Motor PMG 132, permanent magnet DC motors generating 20 Nm of torque for 110 A of current. Their maximum operating voltage is 72 V, but on the quad bike they are working at 48 V, providing each one a maximum continuous power of 5.2 kW (110 A) and a peak power of 9.6 kW (200 A). They are geared to the wheels with a 7.3 gear ratio, bringing the continuous

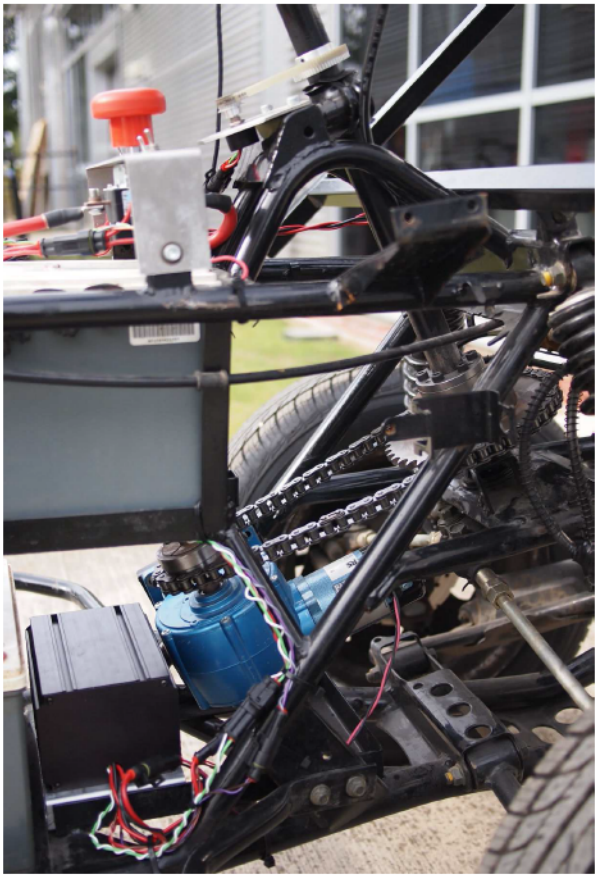

Figure 4.3: *The motor to control the steering of the quad bike, with the motor control box and the potentiometer on top to measure the position of the steering column*

torque available to each wheel to 146 Nm. The wheels having a radius of 270 mm, the continuous propelling force generated by the two motors reaches up to 1081 N (110 A per motor).

Between the two front wheels there is a small DC motor connected to the steering column. Figure 4.3 shows the motor, as well as the box containing the steering control board. The motor is a Parvalux PM10 with LWS gearbox (this is an acronym used by Parvalux) and it is used to control the steering position programmatically. It is powered by the same 48 V used for the propulsion motors and it can provide 0.2 Nm of torque for 2 A of current. The motor is geared down to provide a sufficient torque at the steering column. First, the shaft of the motor is connected directly to a worm drive which brings the rated speed of 4000 rpm down to about 5 rpm at the output shaft (the precise gear ratio is 833). Such a gearbox configuration causes high losses and requires 100 W of electrical power to generate 50 W of mechanical power, but the torque available increases to 100 Nm. Besides offering huge gear ratios in a relatively small space, the worm drive architecture offers another important advantage: due to the friction between the worm and the worm wheel, the input shaft

cannot be driven from the output shaft (Norton 2008). This characteristic eliminates any movements of the steering column caused by external forces (e.g. a bump). The output shaft of the worm drive is connected to the steering column by two sprockets and a chain. Such transmission provides a further gear ratio of 2.2, in order to bring the torque at the steering column up to 220 Nm, for a rotational speed of 2.2 rpm. This torque is similar to what can be provided by an average person turning the handlebar, although the person can exert more power and turn the handlebar much faster. Nonetheless, the speed of the steering was not a critical requirement for our autonomous vehicle.

Very close to the steering motor there is a black box containing the steering control board, presented extensively in Section 4.6. Few switches are located right behind the handlebar, in order to power and control the system. Together with them there is an emergency button to cut off the power to the motors. Located very close to the emergency button, a rotary potentiometer is connected to the steering column. This is used to provide the steering position to the steering control board. The potentiometer is a Vishay Spectrol 357-4506-502, single turn (340° electrical travel) with 5 $k\Omega$ resistance. It is connected to the steering column by two gears and a toothed belt, providing a gear ratio of 2.5. This means turning the steering column by 136° causes one entire electrical turn of the potentiometer. This gearing therefore increases the resolution of the steering position measurement (due to the quantization of the analog-to-digital converters, described in Section 4.6).

At the very front of the quad bike there is a frame to mount all the cameras (stereo cameras, 3D cameras with infrared emitter, etc.) used for the visual recognition of the environment around the quad. There is also a PC to compute the video information coming from the camera and communicate wirelessly to a stationary server. Such devices are not used for the research presented in this thesis, but are needed for other projects targeting the development of an autonomous vehicle (see Section 1.1).

4.3 The Vehicle Control Box

Most of the electronics to control the quad bike is inside a large white box on the rear of the vehicle. The content of the box is shown in Figure 4.4. On the left of the box there is a "reconfigurable embedded control and acquisition system" from the manufacturer National Instruments. This system is called **CompactRIO** and it is a standalone device with input-output modules which can receive data from sensors, compute them in real-time and control actuators in response. Thanks to its rugged hardware, designed to withstand shocks and vibrations and its suitability for a wide range of supply voltages, CompactRIO

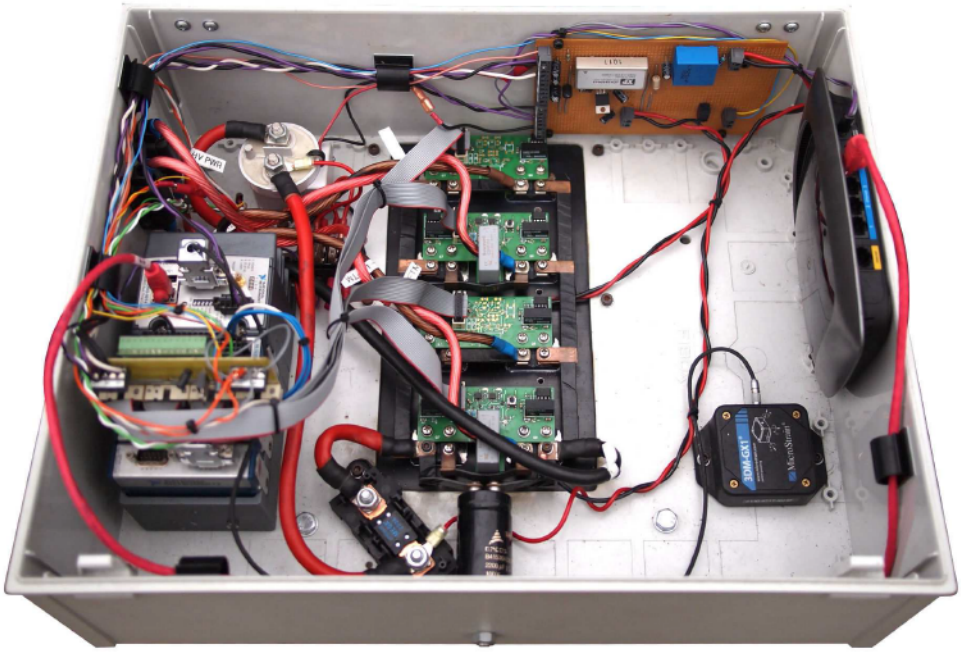

Figure 4.4: *The electronics inside of the white box*

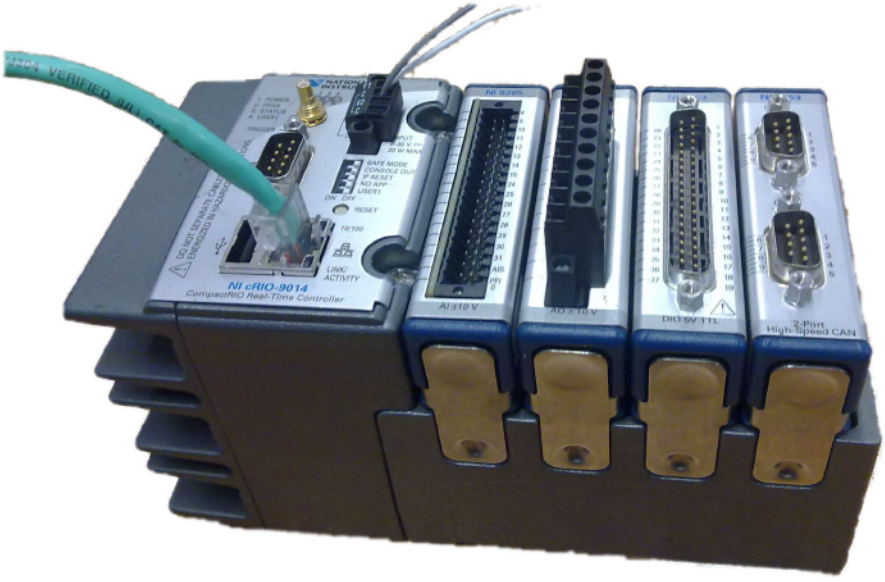

Figure 4.5: *The configuration of the CompactRIO used on the quad*

is an ideal device to be mounted on a vehicle. The configuration used on our quad bike is shown in Figure 4.5 and it consists of:

- NI cRIO-9014: real-time controller running a 400 MHz Freescale MPC5200 floating-point microprocessor and integrating 128 MB of DRAM, 2 GB of nonvolatile storage, one Ethernet port, one USB port, one serial port, power supply, a few control switches and LEDs. Its processing power is used for the computation of the mechanical dynamics

of the quad, for saving the data into files, for managing the user interface, for communicating with other devices like the server providing the trajectories to follow or the inertial sensor providing the acceleration experienced on the quad (more details are given in Section 4.5).

- NI cRIO-9103: 4-slots chassis integrating a reconfigurable Field-Programmable Gate Array (FPGA) Virtex-II from XILINX. Its processing power is used for the current control of the motors and the speed estimation (more details are given in Section 4.5).
- NI 9205: 32-channels 250 kS/s analog input module. It is used to sample the current in the two motors, the battery voltage and a few user interface data such as the potentiometer position on the handlebar. The inputs are multiplexed.
- NI 9403: 32-channels 7 μs digital I/O module. It is used to sample all the digital inputs, in particular for the user interface.
- NI 9401: 8-channels 100 ns ultrahigh-speed digital I/O module. It is used to send the pulse-width modulation (PWM) signals to the drivers of the power transistors.
- NI 9853: 2-ports high-speed CAN module. It is used to communicate with the steering control board (see Section 4.6).

There are some connections to these boards, as can be seen in Figure 4.4. From the top of the NI 9401 four ribbon cables connect to the four PCBs at the centre of the box. These PCBs hold the power electronics to drive the two traction motors, and they have been entirely designed by me (see Figure 4.6).

Each board is mounted on top of two power MOSFETs. These MOSFETs are IXFN 150N15 and they can sustain a current of 100 A and a voltage between source and drain of 150 V. Four of them are needed to drive each motor, given that they are connected according to the H-bridge architecture, which is shown in Figure 4.7. The power MOSFET embodies a freewheel diode, which carries the current when there is no other electric path to follow. This happens quite often when PWM is applied (see Section 4.4 for details), because some deadbands are left after turning off one transistor and turning on the opposite one, to avoid short circuits.

Each board drives one half of the H-bridge and two of them are needed to drive each motor. One board for each pair integrates a current sensor and protection against overcurrent. Figure 4.8 shows the schematic of this board. Each MOSFET is driven by an optocoupler powered by an isolated DC-DC converter, in order to separate the voltage used by the control electronics

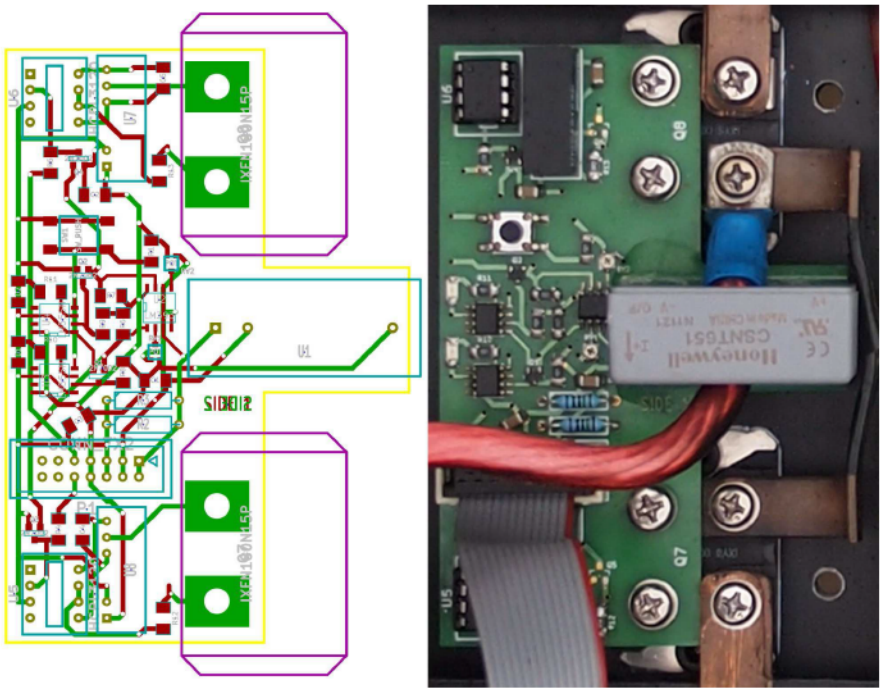

Figure 4.6: *The design of the power electronics*

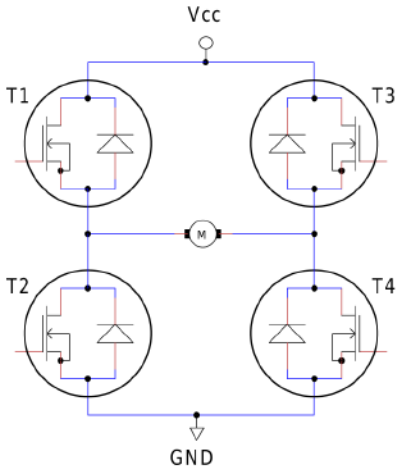

Figure 4.7: *An H-bridge with a motor connected to it*

from the voltage used to drive the motor. Each optocoupler drives the gate between +12 V and -12 V, referred to the source of the MOSFET. The negative voltage is applied to make sure the transistor does not turn on unexpectedly because of slight oscillations in the gate voltage. These oscillations are due to the junction capacitance of the MOSFET (Wu et al. 2006). The overcurrent protection works by short circuiting the input of the optocoupler whenever the corresponding comparator detects an overcurrent. The values for the maximum positive and negative currents can be set through two potentiometers on the board. Both signals for positive and negative overcurrent are latched, with two Light-Emitting Diodes (LEDs) showing if any of these faults occurred. The boards are connected to the battery voltage (48 V) by a bus made from a thick copper plate, in order to carry the high currents needed to drive the motors.

At the bottom of Figure 4.4 there is a capacitor connected in parallel to the 48 V bus, to filter the oscillations of current caused by the PWM, and a big fuse to protect the battery from short-circuit. The motors are individually protected by fuses, which can be found at the top-left corner, near to a relay used to connect the power electronics to the 48 V battery.

On the right of Figure 4.4, starting from the top, it is possible to see the board measuring the bus voltage and providing the various voltages to the circuitry: 12 V non regulated from the battery is used to power the CompactRIO and $\pm$ 12 V regulated supply is used to power the current sensors and the drivers. Just below there is the wireless router that receives the directions for the vehicle through WiFi and sends them to the CompactRIO via Ethernet. It is also used to send the video stream captured on the vehicle to an external server in order to reconstruct the scene surrounding the quad bike. On the bottom-right corner there is the IMU, which communicates with the CompactRIO via serial interface. It is used to provide information about the orientation and the movement of the vehicle. To summarize the most important electrical connections on the quad bike, a diagram of the wiring is shown in Figure 4.9.

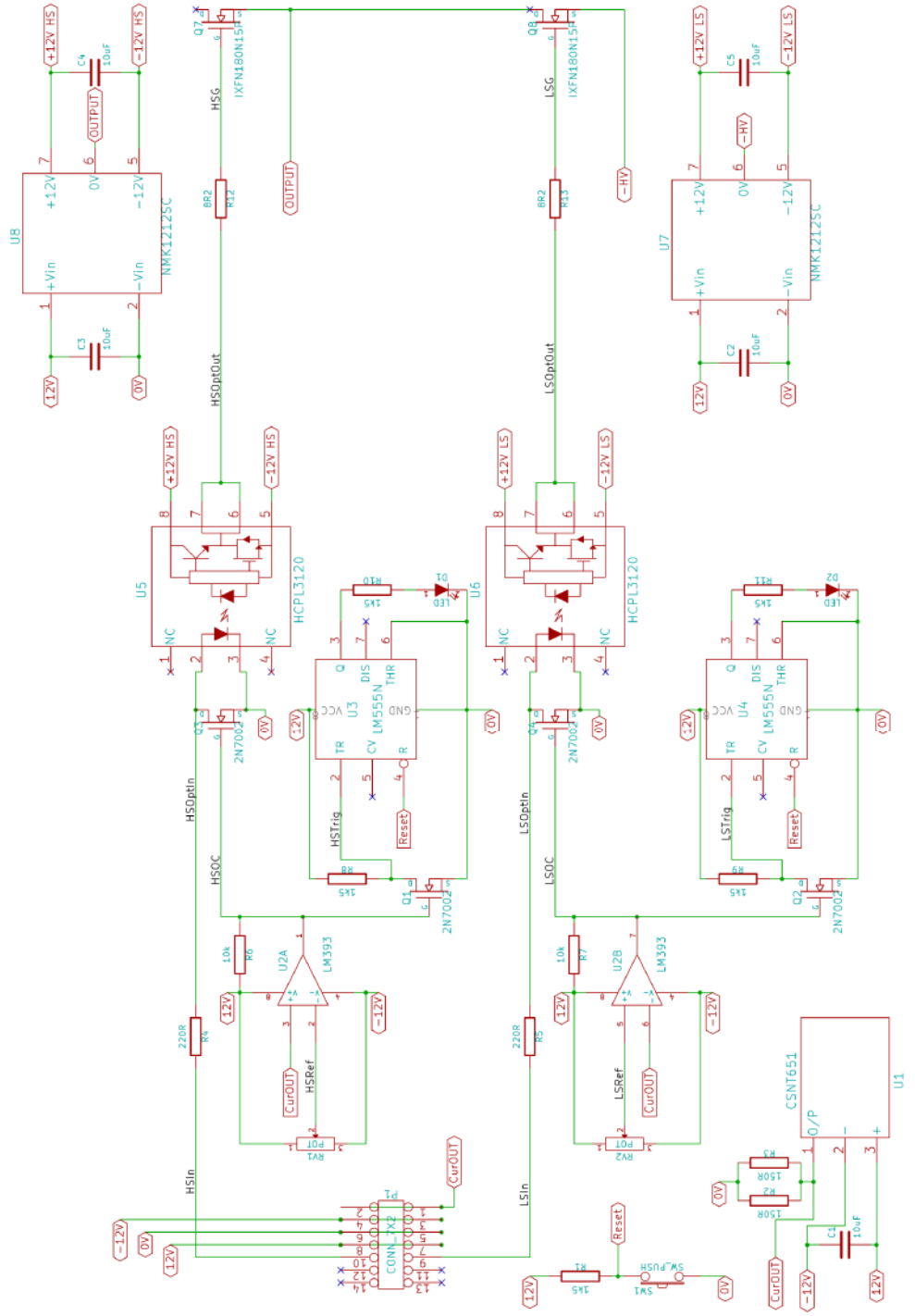

Figure 4.8: *The circuit diagram of the driver boards*

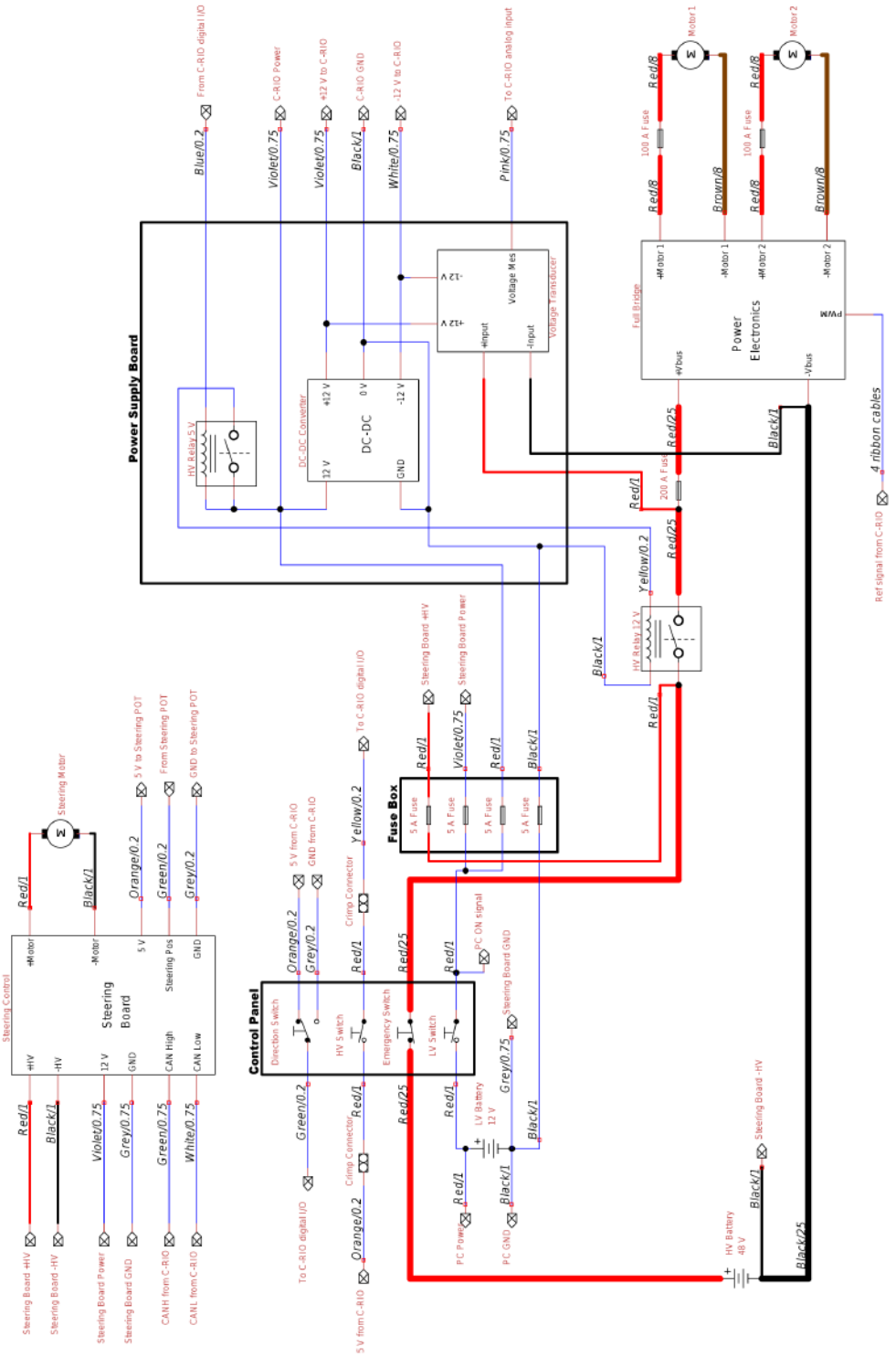

Figure 4.9: *The electric connections on the quad bike*

4.4 Control of Traction Motors

The motor control needed for most of the traction control application is a torque control. With a first approximation, quite reasonable for a permanent magnet DC motor, the torque is considered proportional to the armature current. Because the current can be measured much more easily than the torque, current control is implemented instead of torque control. The coefficient between current and torque is 0.18 Nm/A at the motor and 1.32 Nm/A at the wheel (See Section 4.2).

Commercial controllers are available for the motors used, however these are mostly speed controllers. Some torque controllers are available but they are off-the-shelf components and they cannot be customised according to the specification of my project. In Chapter 5 some advanced techniques of traction control will be presented, which require the control of the torque applied with a relatively high bandwidth, about a hundred Hz. This corresponds to a current response in the order of few milliseconds, which is easily achievable by some commercial devices. Unfortunately, I was not able to find any controller which was designed to run custom applications or to respond to external commands at such a fast rate. For this reason, a bespoke current controller had to be developed. This turned out to be a very significant part of the work.

An H-bridge of metal-oxide-semiconductor field-effect transistors (MOSFETs) was chosen as the hardware architecture to drive the motors (see Section 4.3 for details). This is a common solution in motor control for automotive applications thanks to its high efficiency and relatively low cost. Such architecture exploits pulses of voltage with different width to modulate the average voltage applied between 0 V and the battery voltage (PWM). The pulses of voltage are filtered by the inductance and the resistance of the motor, generating a current with a ripple at the PWM frequency. The ripple has a triangular shape, with the current increasing when the battery voltage is applied and decreasing when the motor is short circuited.

Because the motor current is associated to the torque generated, the current ripple translates into mechanical vibrations. Moreover, it causes high electromagnetic disturbance. It is therefore important to reduce the amplitude of the current ripple by increasing the PWM frequency. On the quad bike a PWM frequency of 20 kHz is used. This frequency is towards the upper boundary of the hearing range (approximately from 20 Hz to 20 kHz), making the motors barely audible. The increase of the PWM frequency causes a loss of resolution in the voltage applicable, due to the limited time-resolution of the microcontroller. In fact, the PWM signals are generated with an accuracy of 25 ns (40 MHz is the clock speed of the FPGA) and have a minimum width of 100 ns,

due to the limitations of the I/O module. This translates into a voltage resolution of 0.024 V and a minimum voltage applicable of 0.096 V. Such values are relatively small and do not affect the current control substantially.

The motors used have very low values of armature inductance and armature resistance, about 20 uH and 45 $m\Omega$ respectively. The smaller these parameters are the wider the ripple of the current is and the faster the current response can be. To have a rough idea of the complications in the development due to such a low inductance it is possible to neglect the effect of the resistance for a moment. An erroneous implementation of the current control which applies the maximum voltage for one PWM period would cause the current to rise from 0 A to 120 A, which is very close to the current limit of the transistor used. This was a huge problem because initially the boards driving the motors were not protected against overcurrent and a current limitation implemented by software would have been too slow. Finally a proper protection circuit integrated into the driver of the transistors was designed (more on that in Section 4.3).

4.4.1 Challenges

4.4.1.1 Minimum Non-Zero Voltage Applicable due to Deadbands

In Section 4.3 I mentioned the need to apply certain deadbands between the switching of the two transistors in each leg of the H-bridge. In each leg, in fact, the two transistors switch in opposition in order to pull the voltage at the motor terminal alternatively towards the battery voltage and towards 0 V. Without the deadbands, because of the time inherently required to switch a transistor from an off to an on state, a short circuit would be temporarily created across the bus of the H-bridge. The deadbands need to be applied for a specific time dependent on the physical characteristics of the transistors. During the deadbands, the motor current is sustained by the freewheeling diode embodied into one of the two MOSFETs, depending on the current direction. For example, in Figure 4.7 a positive current going through the motors from T1 to T4 will start passing through the freewheeling diode in T2 as soon as T1 is switched off. This will apply 0 V at the motor terminals during the deadband. A negative current instead will be carried by the diode in T1, applying Vcc at the motor terminals. During a full PWM period each transistor switches two times in order to alternatively pull the voltage of the motor terminal to 0 V and Vcc, therefore modulating the average voltage applied. The fraction of the PWM period in which the motor terminal is pulled to the battery voltage is called duty cycle. The duty cycle is particularly important because it also represents the ratio between the average voltage

applied and the battery voltage.

Because each transistor switches two times, two deadbands are applied for every PWM period. During each deadband, the voltage applied to the motor terminal only depends on the direction of the motor current. When the motor current is negative, which happens during braking, the voltage applied during the deadbands is the battery voltage (Vcc). This limits the minimum time that the motor terminal can be pulled to the battery voltage. Consequently, for a given PWM period, the minimum non-zero duty cycle that can be applied (zero duty cycle can always be applied if there is no switching at all) depends on the deadbands. The deadband chosen for the hardware in the quad bike was 1 μs and with a PWM period of 50 us, the minimum non-zero duty cycle is 4/100. This translates into a minimum voltage applicable (averaged in a full PWM period) of about 2 V, which is actually a critical value that significantly affects the current control. It is important to stress that this limitation stands only when the motor current is negative, which only happens when the motor act as a generator.

4.4.1.2 Control Instability due to the Minimum Non-Zero Voltage Applicable

Figure 4.10 shows the experimental data from a test of one of the earliest implementations of the current control on the quad bike. The top diagram shows the currents in the two motors and the set current, while the bottom diagram shows the voltages applied to each motor. In general, for positive values of the set current, the motor currents are correctly controlled. Most of the current ripple is inherently due to the resolution of the current sensors and the timing of the sampling of the analog signals (more on this in Subsection 4.4.1.3). There are also some fluctuations of the current of one of the two motors for high positive values of current. This is because the control of both motor currents was erroneously using the feedback of only one motor current, and therefore any difference in the characteristics or the loading of the two motors would cause a poor control in one of the two currents.

The aim of this paragraph is to focus on the instability that appears for negative values of the set current, whenever the voltage applied to the motor approaches zero. This is an example of issue caused by the limitation in the minimum non-zero voltage that can be applied to the motor (already discussed in Subsection 4.4.1.1). At this stage the current control was implemented with half H-bridges (instead of the full H-bridges of the latest revision), meaning it was not possible to apply negative voltage to the motor terminals but only zero (short circuit) or the positive voltage of the battery. For this reason, it was only possible to produce negative current (therefore braking) with the

motors moving forward, exploiting the back-electromotive force generated by their motion. This explains why, when the motor speed is zero, the currents cannot be controlled to the negative set value. But what is the origin of the instability shown in Figure 4.10? The deadbands.

To a first approximation (ignoring the inductive load), the current is roughly proportional to the difference between the voltage applied to the motor terminals and the back-electromotive force. For this reason, for a constant value of set current, the voltage applied to the motor terminals has to change accordingly to the back-electromotive force, and consequently to the speed of the motor. With the motor slowing down the back-electromotive force reduces, therefore the motor controller reduces the voltage applied to the motor, in order to control the current at the set negative value. When the speed is low enough, the voltage required at the motor terminals for an effective current control goes below 2 V, a value that cannot be applied, on average, in a single PWM period because of the presence of deadbands. The motor controller will then start to alternate the voltage at the motor terminals between 0 V and 2 V.

It is important to clarify that these values are the average value in every PWM period, but during each PWM period the voltage will keep oscillating between zero and the battery voltage. Basically, the optimal voltage will be applied, on average, over multiple PWM periods instead of a single PWM period because of the deadbands. This induces important oscillations in the current, with amplitude in the order of 30 A, as seen in Figure 4.10. To avoid such a critical condition, I decided not to apply braking power when the voltage is so low. This happens when the motor speed is similarly low, depending on the current flowing in the motor coil, and the vehicle is almost stopped. To have a consistent feeling during driving, I used the motor speed as a reference to decide when to remove the braking torque, instead of using the applied voltage. Using the applied voltage would have caused the removal of the braking torque at slightly different speeds every time.

4.4.1.3 Timing of the Control

Another issue I encountered, related to the hardware architecture chosen, is that the currents need to be sampled as close as possible to the beginning or the middle of the PWM (Bose 1997). Because of the triangular shape of the current ripple, this is the only way to measure the average value of current during one PWM period, as sampling at another point would record the current ripple due to the PWM and using a low pass filter would noticeably delay the control. Thanks to the precise control of the hardware offered by the FPGA (see Section 4.5) it was possible to sample the current correctly. It is

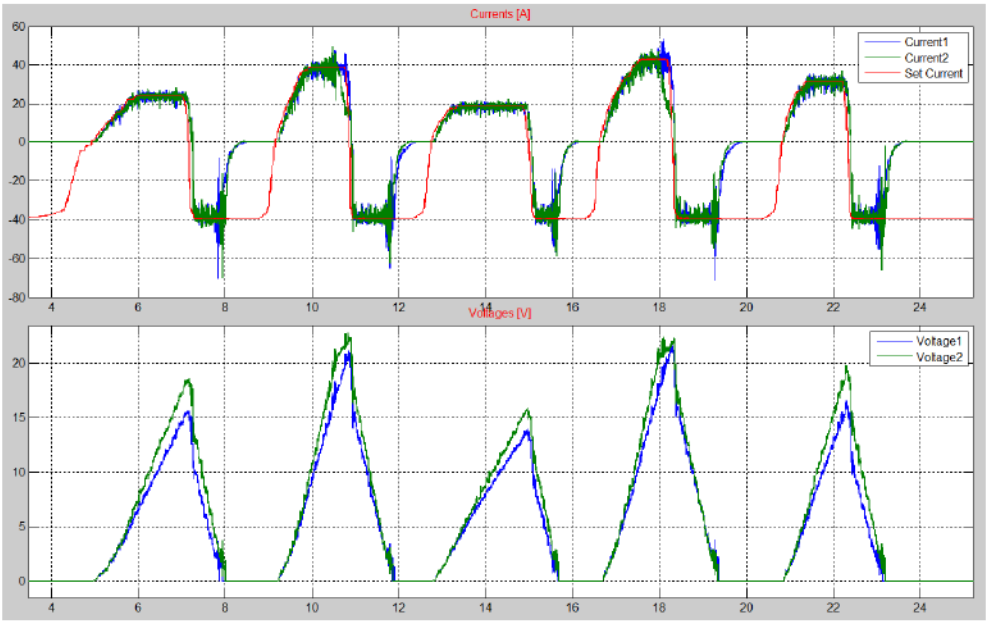

Figure 4.10: *Early implementation of current control on the quad bike, with instability during braking at low speed*

Table 4.1: *Specifications for the current control of the quad bike*

Parameter	Value
PWM period	50 us
PWM deadband	1 μs
FPGA clock	25 ns
analog sampling period	100 us
motor resistance	45 $m\Omega$
motor inductance	20 uH

important to remark that because there are four analog inputs that need to be measured (the current for each motor, the bus voltage and the position of the potentiometer at the handlebar) and because the analog input module is multiplexed, only two inputs can be sampled during each PWM period (50 us). As previously explained, the samples are taken at the beginning and at the middle of each period. For this reason, the measurement of all four inputs takes two PWM periods, with each input sampled at a frequency of 10 kSa/s. Because the current control has to wait for the current sample, it also runs at 10 kHz for each motor. Table 4.1 summarises the specifications of the system used for the control of the motor current.

4.4.2 Simulation and Tuning

The current control consists of a proportional-integral (PI) controller implemented in discrete form with the output limited according to the battery voltage. Integral windup problems are avoided by limiting the integral term whenever the output saturates. Even a simple task like tuning the gains of the controller proved to be more challenging than expected. In fact, the brushes of the motor make contact with a number of rotor coils that changes with the position of the motor. This discontinuity in the system generates rapid current variations that are impossible to eliminate, making the online tuning of the controller very difficult. To find the best gains for the controller I used an analytical model of the motor and the control. While the motor model is continuous, it has to be expressed in the discrete domain because the control is discrete. The transfer function between voltage and current in the motor is expressed by Equation 4.1.

$$G_p(s) = \frac{\frac{1}{L_a}}{s + \frac{R_a}{L_a}} \tag{4.1}$$

Where L_a is the armature inductance and R_a is the armature resistance. This transfer function is expressed with the Laplace transform. As suggested in (Bolton 1998), the discrete model corresponds to the z-transform of the series of a zero-order hold and the system under consideration. The zero-order hold represent the discrete changes to the applied voltage, because of the discrete execution of the current control. As discussed earlier, the current control runs every two PWM periods. The Laplace transfer function of a zero-order hold is expressed by Equation 4.2.

$$ZOH(s) = \frac{1 - e^{-2T_{PWM}s}}{s} \tag{4.2}$$

Where T_{PWM} is the PWM period. The discrete model of the motor can be obtained from the z-transform of the product of $G_p(s)$ and $ZOH(s)$, as expressed by Equation 4.3.

$$
\begin{aligned}
G_p(z) &= \text{z-transform of } \mathcal{L}^{-1}\left\{\frac{1-e^{-2T_{PWM}s}}{s}\frac{1}{L_a}\frac{1}{s+\frac{R_a}{L_a}}\right\} \\
&= \text{z-transform of } \mathcal{L}^{-1}\left\{\left(1-e^{-2T_{PWM}s}\right)\left[\frac{1}{R_a s}-\frac{1}{R_a\left(s+\frac{R_a}{L_a}\right)}\right]\right\} \\
&= \left(1-z^{-1}\right)\left[\frac{z}{R_a\left(z-1\right)}-\frac{1}{R_a}\frac{z}{z-e^{-2\frac{R_a}{L_a}T_{PWM}}}\right] \\
&= \frac{z-1}{z}\frac{z\left(1-e^{-2\frac{R_a}{L_a}T_{PWM}}\right)}{R_a\left(z-1\right)\left(1-e^{-2\frac{R_a}{L_a}T_{PWM}}\right)} \\
&= \frac{1-e^{-2\frac{R_a}{L_a}T_{PWM}}}{R_a\left(z-e^{-2\frac{R_a}{L_a}T_{PWM}}\right)}
\end{aligned}
\tag{4.3}
$$

The variables in Equation 4.3 can be substituted with the correct values for the system in use, which are summarised in Table 4.1. The resulting discrete transfer function is expressed by Equation 4.4.

$$
G_p(z) \approx \frac{4.47}{z-0.79} \tag{4.4}
$$

Starting from the discrete transfer function of the system, I used MATLAB to automatically calculate the optimal gains for the PI controller. Using the function *pidtune*, it was simply a matter of choosing the desired response time among the ones that were achievable without compromising the stability of the system. The chosen gains are 0.002 and 40 respectively for the proportional and the integral term and the resulting response is shown in Figure 4.11. The settling time is in the order of 5 ms, with an overshoot of merely 5%. A response so fast would allow the control of the current at a frequency up to 50 Hz. This discretization process might looks unnecessarily complex as the response for a continuous system is basically the same. However I used the discrete model to simulate the effects of a delay of one control period ($\frac{1}{z}$) or the average of the last n samples ($1+\frac{1}{z}+\frac{1}{z^2}+\ldots+\frac{1}{z^{n-1}}=\frac{z^n-1}{(z-1)z^{n-1}}$). I discovered a delay of one control period will not significantly affect the response of the current while averaging the samples leads to unwanted instability and has been avoided. In the discrete PI controller there is no calculation of the integral of

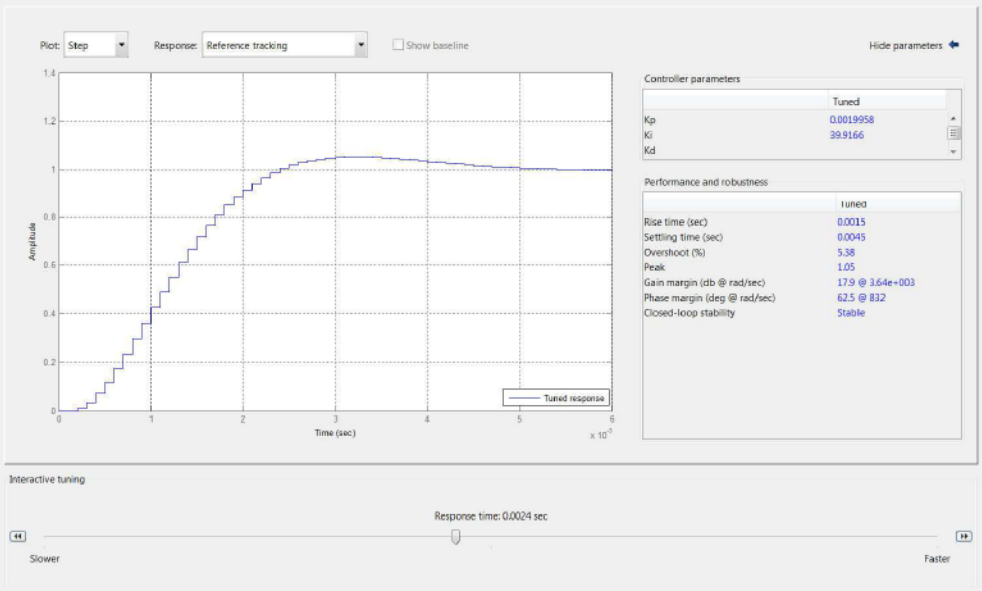

Figure 4.11: *The interface resulting from the MATLAB function* pidtune

the current error over time, which can be approximated to the sum of the errors multiplied by the control period. To avoid such operation the sum of the current errors is directly multiplied by the integral gain times the control period which is $40 * 100 * 10^{-6} = 0.004$.

4.5 The Control Code

The code running on the CompactRIO is divided in two parts, one running on the floating-point microprocessor and the other one implemented in fixed-point on the FPGA. This is to deal with the different requirements for different areas of the control code. The code running on the microprocessor is the easiest to write, because it does not have to deal with the limitations of the FPGA like the limited set of libraries and operations, the limited length of one computational cycle (everything has to be executed in one clock cycle), the limited size of the code (due to the area limit of the FPGA), the precise timing description of each task, the fixed-point operations, etc. It has also to be considered that it is very quick to compile a code for a microprocessor, while it takes a long time to translate a code into its FPGA implementation. The final code used in the quad bike takes around half an hour to be compiled for the FPGA. The downside of running a code on the microprocessor is the lack of control of the timing below 1 ms, because of the jitter due to the multitasking management and the operative system operations. Moreover, the FPGA allows multiple tasks to run simultaneously, as they are physically implemented on the silicon surface, while the microprocessor can only manage as many simultaneous task

as the number of cores, which is one in my configuration. All these characteristics makes the FPGA the only possible candidate to run the current control of the motors at 20 kHz, while the other operations are performed on the microprocessor. Among them there are the recording of data, the control of the mechanical dynamics and the communication with other devices and with the user interface.

The programming language used is LabVIEW, a visual programming language developed by National Instruments. Later in this section some examples of code will be presented. The code has been created with a modular structure in order to limit the size of the code base, to simplify updates and to reduce errors.

4.5.1 Microprocessor Code

Figure 4.12 shows the main diagram of the code running on the microprocessor. It only represents a small portion of the code, which includes several functions called inside the blocks of the main diagram. In this version of the code a User Datagram Protocol (UDP) message sets the steering position and the current in the traction motors. The code is too large to be displayed in detail in Figure 4.12, but it is possible to identify three separate frames: the initialisation, the control and the shutdown procedure. There is a fourth frame underneath the main sequence, which contains the shutdown procedure in case of timeout of the watchdog. This happens when the software stops responding for a critical amount of time, set at 200 ms. Inside the control frame it is possible to identify four tasks, grouped into separate block, which I marked from **a** to **d** for clarity. These tasks are running on a single core therefore they do not run in parallel but are interleaved. Because a delay in the execution of one task can interfere with the operation of another one, a priority value is assigned to each one of them and the tasks with higher priority are always executed first.

Task **a** of Figure 4.12 manages the communication with the IMU. It also computes the linear accelerations and the angles of yaw, pitch and roll of the vehicle. It has the highest priority because it runs faster than the other tasks, every 20 ms. Any other task would take longer than 20 ms to execute, so they could not have an higher priority without delaying the communication with the IMU. This would cause the inertial samples to be unequally spaced and it is not desirable.

Task **b** of Figure 4.12 is the most critical and the most complicated. It runs every 50 ms to guarantee a smooth control of the quad bike. First, it services the watchdog, to make sure the task executes periodically. Then, it receives the UDP message from the Ethernet connection and sends the set current and

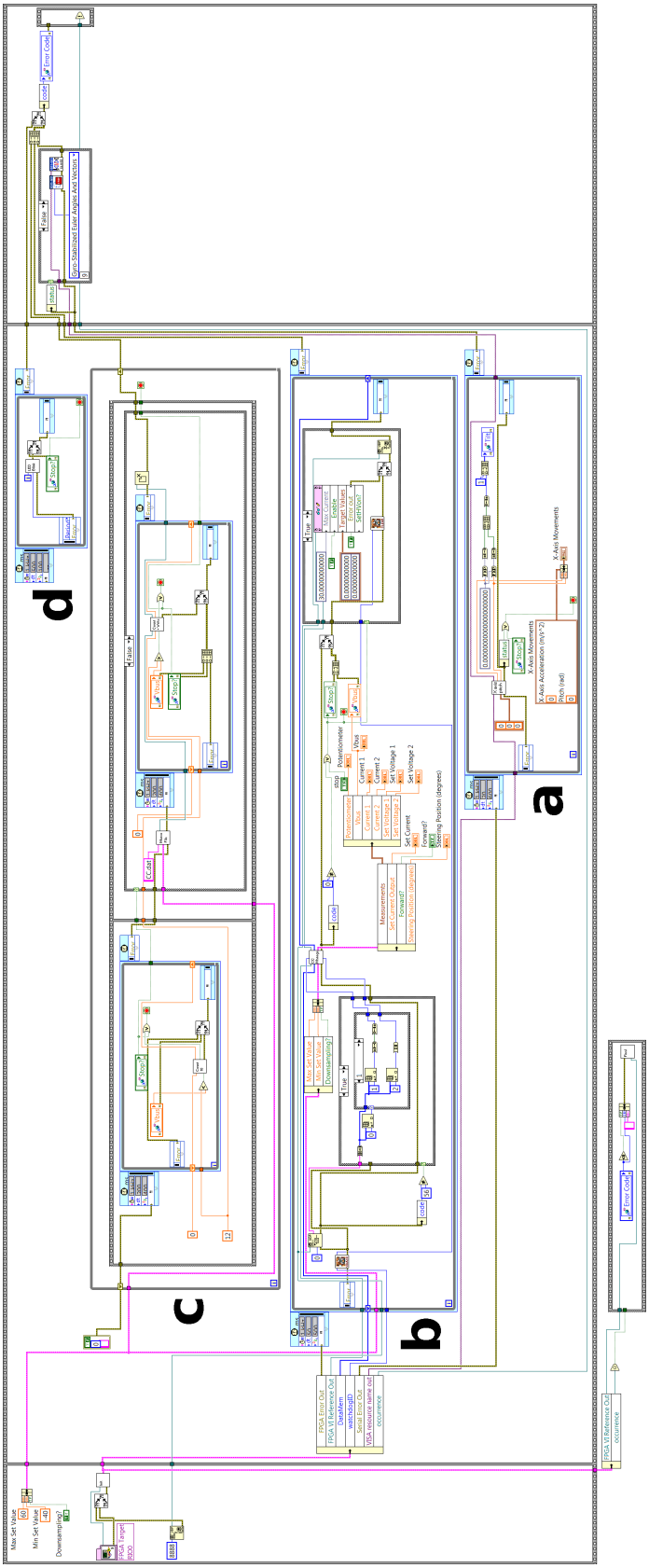

Figure 4.12: *The code running on the microprocessor*

the set steering position to the FPGA, together with other control variables. It reads the measurements from the FPGA and stores them in a local array, in order to log the data in a file. It manages the CAN communication and it deals with any error occurring during the control.

The communication between the microprocessor and the FPGA is particularly critical. It uses a First In First Out (FIFO) structure that needs to be initialized first. It is the most optimised way to transfer large amounts of data between the FPGA and the microprocessor and it allows the transfer and recording of all the measurement samples. There are four measurement channels (one current for each motor, the bus voltage and the potentiometer position) sampled at 10 kHz, meaning 40 kSa/s. Each sample is composed of 16 bits, and two samples are grouped together because the FIFO only manages data structures of 32 bits. This corresponds to a data rate of 640 kB/s, which is about 38 MB each minute. The management of such quantities of data is necessary during the developing stage to tune the control and to spot any anomaly, but it is avoided during normal operation.

Task **c** of Figure 4.12 manages the logging of the data into a file. To limit the size of the file no data is recorded when the bus voltage is low, which corresponds to the vehicle being stopped, using a loop at the beginning which waits for the voltage to rise. A switch at the front of the quad bike controls the relay connecting the batteries to the bus. This means that the voltage can be suddenly raised to the battery voltage or quickly lowered to zero by toggling the switch, and the recording of the file will start or stop accordingly. Each interruption will cause a new file to be created, named with the actual time and date. The location of the file can be accessed with any File Transfer Protocol (FTP) client from any computer in the same network of the CompactRIO, just by typing the IP address assigned to it.

Task **d** manages the blinking of a LED. It allows the operator to see when the control code is running properly or when it has stopped.

4.5.2 FPGA Code

Figure 4.13 shows the main diagram of the code running on the FPGA. Like the microprocessor code, most of the routines called from the main diagram will not be discussed. This version of the code can be used in combination with any code running on the microprocessor that requires current control. The code is too large to be displayed in detail in Figure 4.13 but it is possible to identify two separate frames: the initialisation and the control.

Inside the initialization frame the offsets of the current sensors are calculated assuming no current is flowing into the motors. At the top of the frame

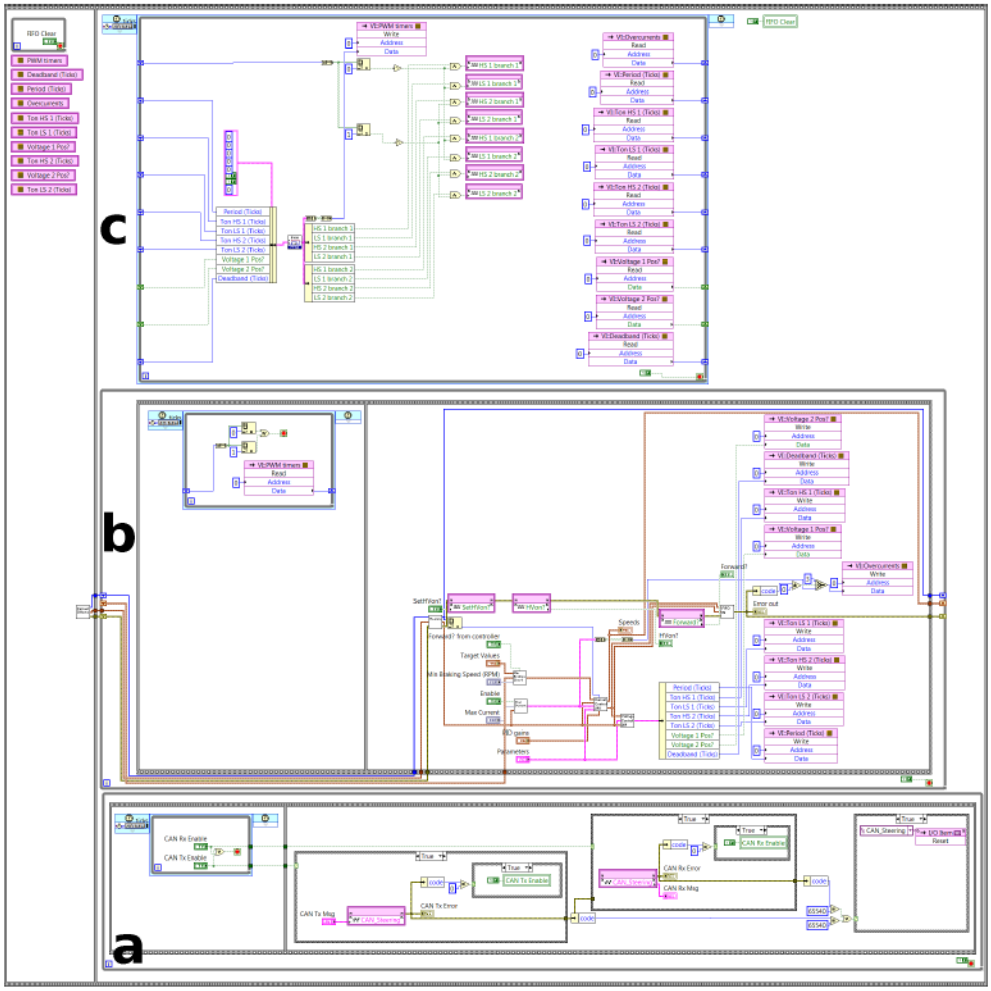

Figure 4.13: *The code running on the FPGA*

an empty loop waits for an input from the microprocessor code following the clearing of the FIFO. After the FIFO has been cleared the execution moves to the second frame where the data transfer is started and a flag indicating the FIFO being clear is reset.

The control frame presents three different tasks, which I marked from **a** to **c** for clarity. These tasks are executed in parallel, at exactly the same time, because they are allocated to separate hardware structures. Consequently there is no clash between tasks for the time allocation and no need to assign a priority value to each task.

Task **a** of Figure 4.13 manages the CAN communication. It is divided into two frames. In the first frame the process waits till one of the two flags to read and write the CAN bus are set by the microprocessor. In the second frame the message are read and/or written, according to the flags, and if the communication succeeded the flags are reset. If the communication fails the loop carries on until the communication succeeds, if ever. For every attempt,

error messages are written in a register so the microcontroller is always aware of the communication status.

Task **b** of Figure 4.13 handles the current control. The task is divided into two frames to synchronise the current sampling with the beginning or the middle of the PWM cycle (see 4.4 for further information). The first frame is a simple loop waiting for a flag from the PWM task, in order to proceed. The second frame represents the core of the current control, managing the measurement sampling, the overcurrent check, the reset of negative set current in case of low speed (see 4.4 for further information), the PI control of the current in the two motors, the conversion of set voltages into PWM data and the writing of the data into the FIFO. Most of the variables can be set from the code running in the microprocessor, such as the target currents, the motor parameters, the PWM parameters, the PI gains and the minimum speed to apply negative current.

Task **c** of Figure 4.13 generates the PWM for the two H-bridges driving the motors. At every PWM period it receives from task **b** data such as PWM period, duty cycles and deadbands. At every clock tics it converts these data into logic states for the digital outputs. It also reads the overcurrent flags and stops the PWM in case any of them is set. Finally, it sets two flags whenever the execution is respectively at the beginning or the middle of a PWM cycle, in order to synchronize the current sampling.

The PWM for the full H-bridge is implemented similarly to a half H-bridge architecture, in that the applied voltage is not modulated between plus and minus the battery voltage. Instead, a positive set voltage is modulated between 0 V and the battery voltage, while a negative set voltage is modulated between 0 V and minus the battery voltage. Using Figure 4.7 as a reference, T3 and T4 change state whenever there is a change in the sign of the set voltage while T1 and T2 continuously switch in order to modulate the absolute value of the voltage applied. For example, to apply a positive voltage T4 pulls one motor terminal to 0 V while T1 and T2 modulates the voltage at the other terminal between the battery voltage and 0 V. Such control strategy applies a smaller variation of voltage during each PWM period, reducing the amplitude of the current ripple. Moreover, only two of the four transistors commute for most of the time, which helps to keep down electrical losses.

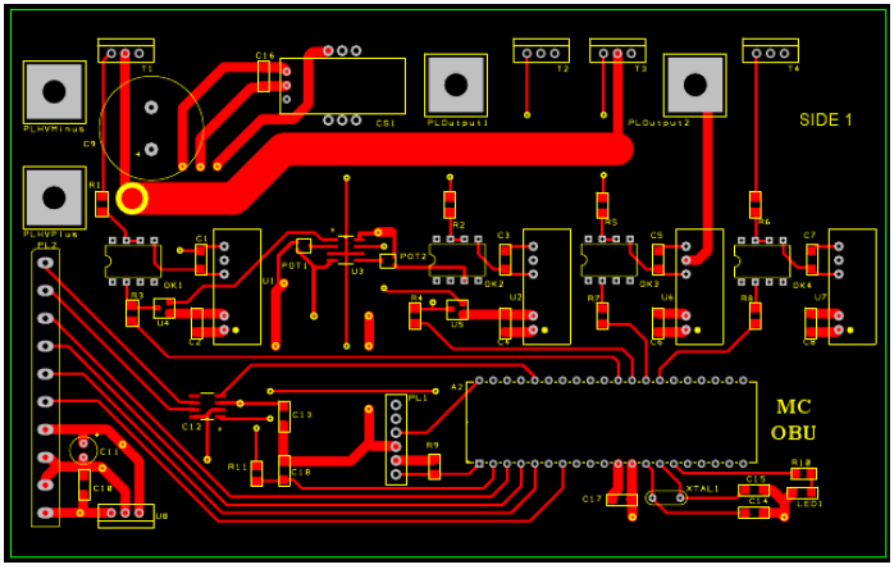

Figure 4.14: *The layout of the steering control board*

4.6 The Steering Control

4.6.1 The Hardware

To control the steering motor, a bespoke PCB has been designed. The final layout of the board is shown in Figure 4.14. The board presents a Microchip PIC18F4580 microcontroller, responsible for the position control, the CAN communication and the PWM.

Figure 4.15 shows the schematic of the board. It is possible to see how the circuit driving the MOSFETs is similar to the one implemented on the boards driving the traction motors (See Section 4.3). The motor has to be controlled in both directions, therefore a full H-bridge architecture is used. The four MOSFETs are on top of the PCB, together with the current sensor. This is clearly shown in Figure 4.14. The centre of the board is dominated by four blocks of components driving the gates of the MOSFETs.

The four big pads visible in Figure 4.14 are the connections for the 48 V supply and the motor terminals. Their size is so large because I designed the PCB to control currents up to 50 A. This would allow using the same board to control a variety of motors, although the steering motor on the quad bike can only withstand a maximum current of 3 A. On the left of Figure 4.14 there is a screw terminal to connect the CAN bus, four analog inputs and the power for the control electronics. Only one analog input is used, measuring the steering position through a potentiometer (see Section 4.2 for details). The control electronics of the board is powered by the same 12 V battery powering the CompactRIO. There is a regulator on-board which converts the 12 V coming

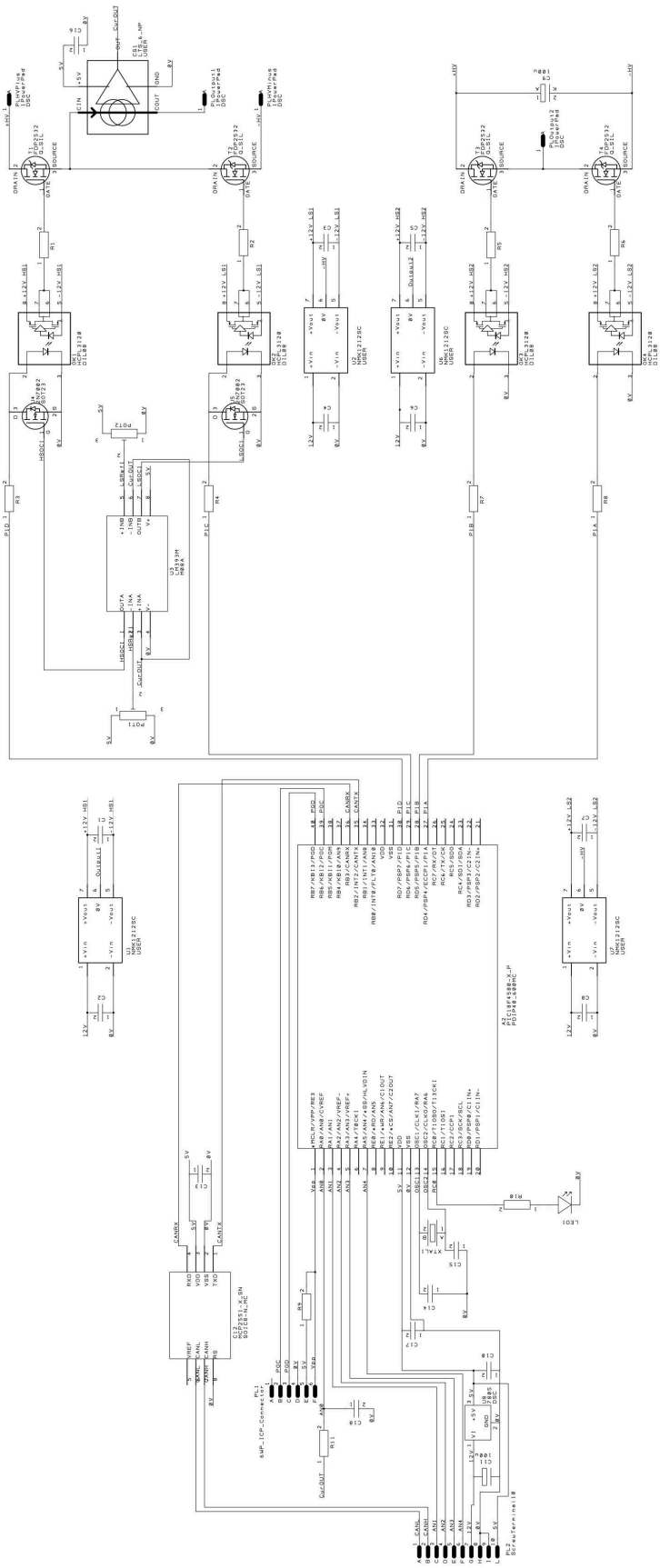

Figure 4.15: *The circuit diagram of the steering control board*

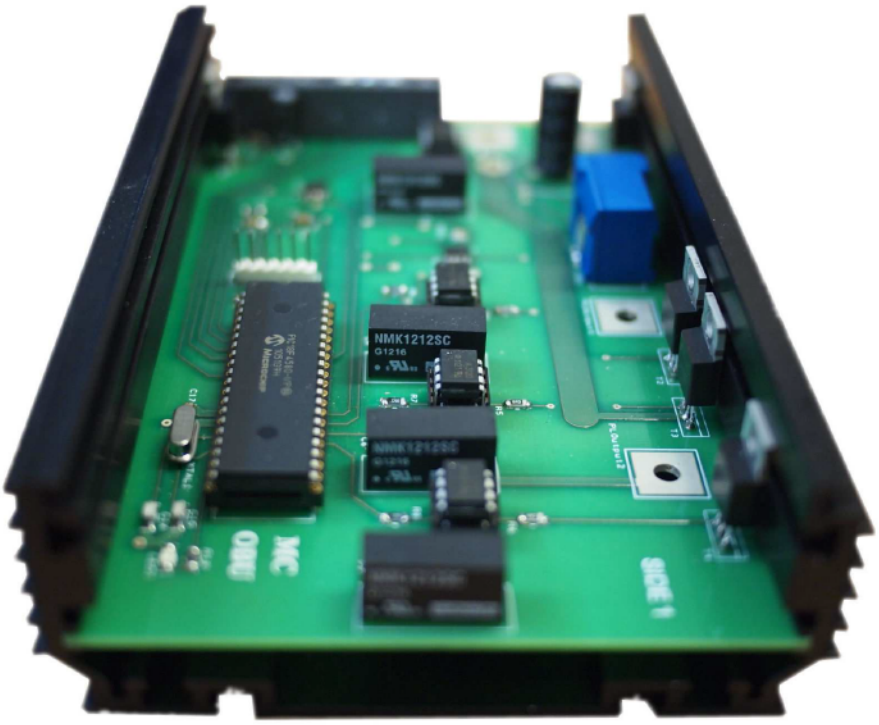

Figure 4.16: *The assembled steering control board, fitted into the protective box*

from the battery into the 5 V required to power the microcontroller. Close to the PIC18F4580 there is a small connector to flash the memory of the microcontroller.

As shown in Figure 4.16, the board is designed to slide into a protective box, which doubles as heat sink for the 5 V regulator and the four transistors driving the motor. The components are positioned at the sides of the board and are fixed to the box with bolts.

4.6.2 The Control Code

The control code has been written in C language and compiled using MikroC compiler for Microchip PIC microcontrollers. In this section I am going to omit any description of the structure of the code, focusing instead on the implementation of the control for the steering position. In general, a common approach to control the steering position is to establish a speed profile to reach the set position from the current position, and to control the motor speed so to follow the profile. Although polynomial trajectories are often used, when the maximum speed is a major constraint it is common to use a trapezoidal profile (Craig 2008; Spong, Hutchinson, and Vidyasagar 2005). In the last case, a maximum acceleration and a maximum deceleration are defined and they are always used to increase or reduce the speed. If the trajectory has to be executed in the shortest time possible, such as in the steering control of the

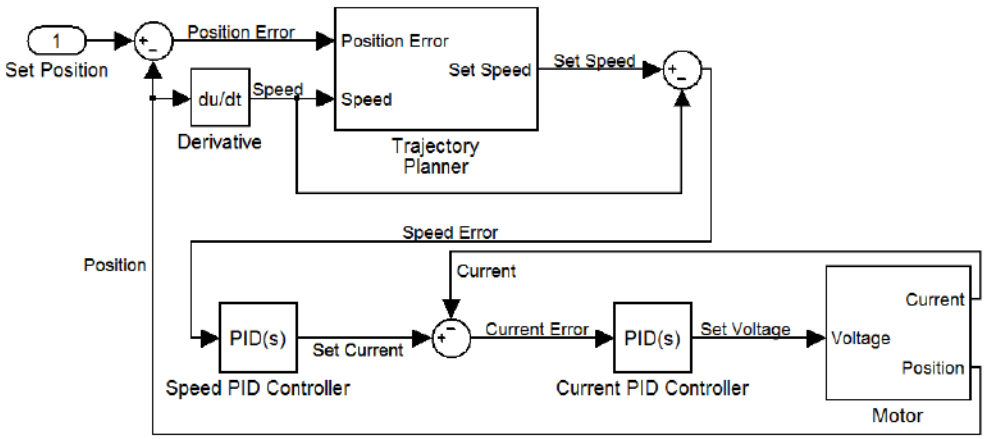

Figure 4.17: *A classic approach to the position control*

quad bike, the maximum acceleration is applied to attain the maximum speed towards the set position. The maximum speed is maintained until close to the target position and then the maximum deceleration is applied to reach the set position at zero speed, in the shortest time possible.

To follow the selected speed profile, the actual speed of the motor is measured and the voltage applied is controlled accordingly. This works because a variation in the motor voltage causes a variation in the current, which is roughly proportional to the torque generated by the motor. A change in the torque generated by the motor causes a change in the motor speed. In most cases the current cannot be a hidden variable in the control loop, because it could reach a value so high that components would start to fail. Therefore it has to be controlled together with the speed. This is usually done with two nested control loops: the inner one is the current loop while the external one is the speed loop. This is shown in Figure 4.17.

The approach finally used for the steering control of the quad bike is not the one shown in Figure 4.17, but a simplified version of it. One of the main reasons for this is the difficulty of accurately measuring the steering speed with the hardware on the quad bike. The potentiometer used to measure the steering column position, introduced in Section 4.2, completes one electrical turn for 136° of the steering column movement. Because the potentiometer is powered by 5 V, the conversion gain is $\approx$ 37 mV per degree. The analog-to-digital converters built into the microcontroller have a resolution of 10 bits over the voltage provided to the microcontroller (5 V). This translate into a resolution of $\approx$ 5 mV, or about one eighth of degree. It seems like a great spacial resolution, but it is actually quite poor to measure speed, because of the low speed of the motor. In fact, the maximum steering speed is 2.2 rpm, around 13° each second. When the motor is moving at maximum speed, it is possible to detect a variation in the motor position every 10 ms. Considering

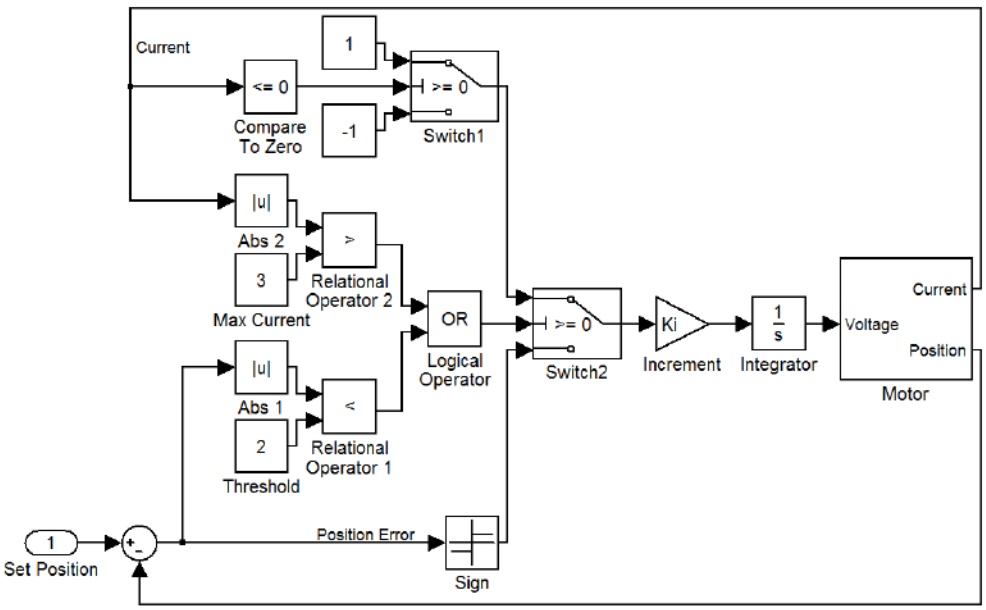

Figure 4.18: *The position control used for the steering*

the strong perturbations in the measurements, due to the vibrations and the high electromagnetic noise, it would require a few hundred milliseconds to reliably measure the steering speed. It would not be practical to control the speed with such a delay, therefore a control algorithm which does not use the motor speed has been developed. The control diagram is shown in Figure 4.18.

When the current is within the set limits and the position error is significant, a positive error causes the voltage to increase, which makes the motor turn forward and reduces the error. Similarly, a negative error causes the voltage to decrease. The increase rate is set by a control parameter, so only the sign of the position error affects the voltage. When the current exceeds the maximum allowed value, the voltage is decreased at the same rate, regardless of the sign of the position error. The same applies when the position error is within a narrow band around zero, so to reduce the current as soon as possible and stop the motor. The control code runs every millisecond, fast enough to suppress any critical overcurrent. This approach greatly simplifies the control scheme of Figure 4.17, in that there is no trajectory planning and only one parameter is needed for the tuning: the increment of the voltage applied. On the downside the performance is affected, with a slower response of the system and non-zero steady state error. Given the slow speed of the motor however, such loss in performance is not appreciable and the steady state error remains within a couple of degrees.

Besides controlling the steering position, the steering control board handles the communication with the CompactRIO via CAN bus. Table 4.2 shows the messages passing through the CAN bus. The steering control board receives a

Table 4.2: *Messages in the CAN bus*

ID(hex)	Function	Data Bytes	Frequency(Hz)
100	Set Steering Position (10 bits)	2	20
120	Actual Steering Position (10 bits)	2	20

message containing the set position and it responds with a message containing the actual steering position. The second information is useful because the load applied to the motor could prevent the motor moving. This could happen if there is a step on the side of the wheels, for example, and the only way to have a feedback about it, is to know the steering is stuck although the maximum torque is applied. This problem of possible sticking of the steering also explains why it is necessary to carefully limit the motor current: the motor could be stalled.

The bus loading can be calculated knowing that the overhead, using the Standard CAN format, is 44 bits for each message. For this reason, a message with two data bytes is composed by 60 bits, and because there are two messages transmitted 20 times per second, the overall data rate is 2400 bit/sec. On the quad bike a bit rate of 50 $kbit/sec$ is used, therefore the bus loading is merely 4.8% and there is plenty of room for additional messages.

4.7 Summary

In this chapter, the development of a remotely-controlled electric quad bike has been accurately described. The components utilised were listed in detail, so that anyone facing a similar design could take them as a reference. The design approach has been carefully presented for both the hardware and the software. Some of the technical problems encountered have been discussed together with the solution adopted.

The vehicle was required for a project involving several PhD students and my contribution was essential and prior. Despite the challenges proving to be harder than expected, adding a considerable delay over the estimated schedule, I managed to deliver the vehicle in full working condition by the end of my PhD. It is now ready to be used by the other members of the ITS project as a platform to build-up a fully functional self-driving vehicle. Their projects will cover the problems of wireless communication, scene understanding and trajectory planning, addressing safety as a primary requirement. Eventually, the vehicle will have to be able to stop itself during emergency situations, such as imminent collision or loss of communication. This was not a requirement for

my project and it is the reason why safety has only marginally been discussed in this chapter.

Chapter 5

Ground Characteristic Estimation

5.1 Introduction

The aim of this chapter is to propose a technique to estimate the friction characteristic of the road from the response of the wheel to the driving torque. The friction characteristic expresses the longitudinal tyre force as a function of the slip ratio, the relative difference of speed between the wheel and the vehicle (see Section 2.3). Strictly speaking, it is not a characteristic of the road and it also depends on the tyre used, the inflating pressure and the normal force applied to the ground. However, for a given configuration of the vehicle, the friction characteristic depends solely on the road. This information is important to tune systems like ASR and ABS, so they can provide the best performance while improving driving safety. The knowledge of the road characteristic could also enhance the functionality of ACC systems, which would be able to regulate the distance from the preceding car by considering the braking space required on every specific surface. The knowledge of the friction characteristic is particularly important for autonomous vehicles, which need to plan in advance the trajectories to follow.

This chapter will introduce a novel technique to estimate the derivative of the longitudinal tyre force with respect to the slip ratio as well as the value of the slip ratio, in order to reconstruct the full friction characteristic. My approach is designed for a vehicle powered by electric motors directly connected to the wheels. Using this configuration, the torque can be controlled quickly and precisely to every driven wheel. Moreover, the applied torque and the speed at each wheel can be easily measured by knowing the voltage applied to the motor terminals and the resulting motor current. My approach proposes to superpose a small cosinusoidal signal to the torque requested by the driver, in order to induce small oscillations in the wheel speed. The measurement of the wheel speed can be used to calculate the phase shift and the amplification between the oscillation in the torque and the resulting oscillations in the wheel speed. Comparing this information with the transfer function between the motor torque and the wheel speed, it is then possible to estimate the slip ratio and the derivative of the longitudinal tyre force with respect to the slip

ratio. My method is simple and cheap to implement in that it does not require any hardware in addition to a standard motor controller with in-built current sensor. Moreover, it is not particularly sensitive to any offset in the measurements because a finite impulse response filter is used to extract the spectral content of the wheel speed around the modulation frequency. This allows to filter out of the estimation process both low-frequency deviations and high-frequency noise. Similarly, my approach is not affected by external forces unless they oscillate around the modulation frequency, which is a quite uncommon situation.

This chapter expands the content of the article I published on the IEEE International Conference on Vehicular Electronics and Safety (ICVES) in July 2012 (Cecotti, Larminie, and Azzopardi 2012). In Section 5.2, the adopted vehicle-model of longitudinal acceleration will be introduced. Section 5.3 will analyse the different forces acting on the vehicle model, while Section 5.4 will introduce the transfer function between these forces and the wheel speed. In Section 5.5, my novel approach to the estimation of the slip ratio and the derivative of the longitudinal tyre force with respect to the slip ratio will be presented in details. In Section 5.6, the transfer function between motive force and wheel speed will be discussed and simplified by applying a few approximations. Finally, Section 5.7 will analyse the results of a Simulink simulation of my estimation method.

5.2 Vehicle Model for Longitudinal Acceleration

In general, the equations describing the dynamic behaviour of a four-wheeled vehicle can be very complicated and non-linear. In this chapter, the overall dynamic will be ignored and all the attention will go to the mathematical model perceived by each driven wheel. The overall force acting on the hub of a wheel is the result of a contribution of forces: the force generated at the interface with the ground (the tyre force) as well as several forces acting in other parts of the vehicle, which are distributed to the hub through the suspension. These forces are: the forces generated by the other wheels, the gravitational force, the inertia of the vehicle as well as any other force applied to the body of the vehicle, such as the air resistance. Their contribution can only be calculated by solving the complicated system of equations discussed in Chapter 3. This is not the aim of the current chapter, therefore I will make some simplification to the vehicle model in order to reduce it to the model of a single wheel.

First, I will assume the inertia that the driven wheel has to overcome in order to accelerate the vehicle is constant and defined by m. This is modelled as a mass located at the centre of the hub. It is a reasonable assumption and,

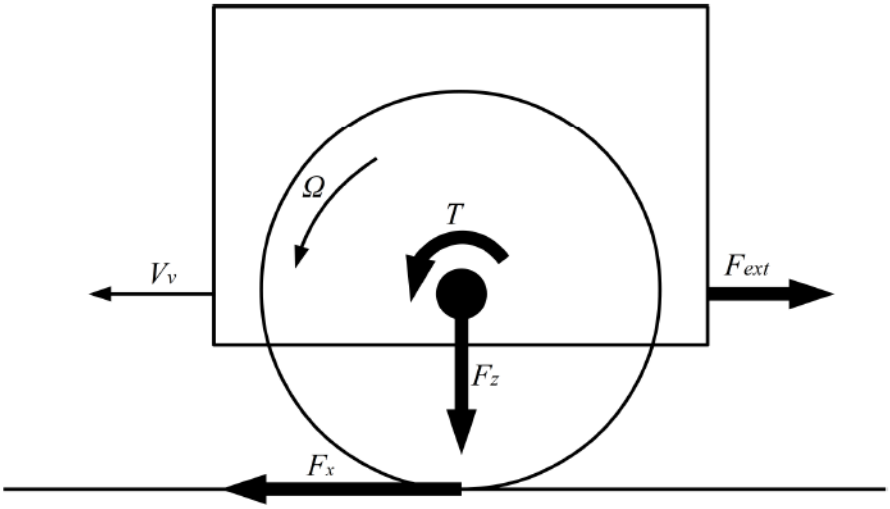

Figure 5.1: *"Single wheel" model of the vehicle; the wheel has a moment of inertia I_y^w and the vehicle has a total mass m*

for a vehicle with two driven wheels having a similar grip with the ground, the mass would be approximately half of the total mass of the vehicle. The approximation does not consider the moment of inertia of the undriven wheels, however this component usually represents less than 10% of the total inertia. Now that m has been defined, it is possible to isolate the inertial force $m\dot{V}_v$ from the longitudinal vehicle force F_X. Based on Equation 3.4, the difference between the longitudinal vehicle force and the inertial force is generally summarised by the external force F_{ext}. Figure 5.1 shows the "single wheel" model used in this chapter. The name of the model derives from the fact that it fully describes a wheel with a moment of inertia I_y^w, a mass m and an arbitrary torque T applied to it. It is important to notice that, by considering a single wheel, the longitudinal vehicle force F_X coincides with the longitudinal tyre force F_x.

The time derivative of the wheel angular speed Ω and the vehicle speed V_v are described by the Equations 5.1 and 5.2 respectively.

$$\dot{\Omega} = \frac{T - F_x R_e}{I_y^w} \tag{5.1}$$

$$\dot{V}_v = \frac{F_x - F_{ext}}{m} \tag{5.2}$$

It is appropriate to rearrange one of the two Equations 5.1 and 5.2 in order to have all the velocities (both linear and angular velocities) and all the forces

(both linear forces and moments of force) represented with the same units of measure. I decided to convert all the variables in Equation 5.1 into linear speeds and forces. Calling $\boldsymbol{V_w} = \Omega * R_e$ the **linear speed of the wheel**, $\boldsymbol{F_m} = \frac{T}{R_e}$ the total **motive force** and $\boldsymbol{M_w} = \frac{I_y^w}{{R_e}^2}$ the **equivalent wheel mass**, Equation 5.1 can be rewritten into Equation 5.3.

$$\dot{V_w} = \frac{F_m - F_x}{M_w} \tag{5.3}$$

From Equations 5.2 and 5.3 it is possible to define $\boldsymbol{F_d} = F_x - F_{ext}$ as the total **driving force** of the vehicle and $\boldsymbol{F_w} = F_m - F_x$ as the total **wheel force**. Their sum corresponds to the combination of forces applied to the vehicle.

In Section 1.3 and Section 2.3, the longitudinal tyre force has been presented as the product between the normal force F_z and the longitudinal friction coefficient μ_x. The latter is a function of the slip ratio, which in turn depends on the longitudinal speed of the vehicle and the angular speed of the wheel. The vehicle model should clearly express this dependencies and, with this purpose in mind, I will rearrange Equation 1.1 into Equation 5.4. Apart from the location of the terms, the second equation differs from the first one by the fact that the dependency between the longitudinal tyre force F_x and the slip ratio is implied, in order to match the simplified notation used in this chapter.

$$F_x = F_z \mu_x \left(\Lambda_t\right) \tag{5.4}$$

According to Equation 2.2, the slip ratio is differently defined for acceleration and braking. In this chapter only the acceleration case will be studied, the braking being analogous. It is important to notice that, because of the different definition of the slip ratio, the mathematical formulas further developed would be slightly different in the braking case. It is useful to write a simplified definition of the slip ratio for the acceleration case, by considering zero lateral slip and by introducing the linear speed of the wheel V_w. This allows to rewrite Equation 2.2 into Equation 5.5.

$$\Lambda_t = 1 - \frac{V_v}{V_w} \tag{5.5}$$

Now that the model is fully described it is possible to build a block diagram

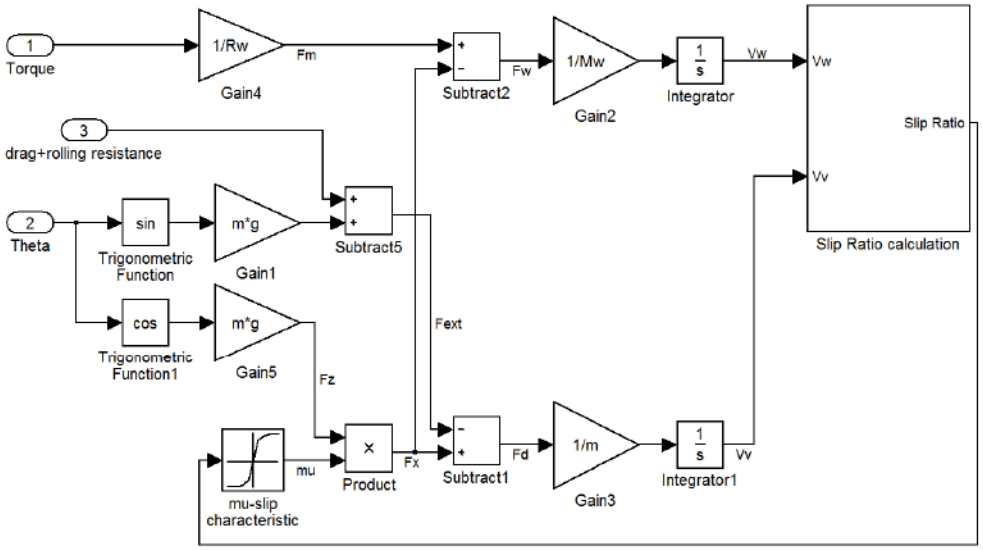

Figure 5.2: *The block diagram of the vehicle model, used to validate the estimation technique proposed in this thesis; the mu-slip characteristic is a look-up table which is unknown and it is the focus of the proposed estimation*

of it, as shown in Figure 5.2. To represent a general friction characteristic, I used a look-up table that associate a specific slip ratio to a friction coefficient. The slip ratio calculation is a direct implementation of Equation 5.5. The block diagram in Figure 5.2 has been used to validate the estimation technique proposed in this thesis, as well as to simulate the behaviour of a vehicle on a road with variable inclination. In particular, the normal force applied to the ground has been calculated as the normal component of the gravitational force due to the vehicle mass m. The external force acting on the vehicle has been calculated as the sum of three effects: the aerodynamic drag, the rolling resistance and the longitudinal component of the same gravitational force due to the vehicle mass m. It is important to notice that, in general, the normal force applied to the ground by any of the four wheels is about one fourth of the normal component of the gravitational force for the whole vehicle. However, the contribution of the gravitational force perceived by any driven wheel along the longitudinal direction is not necessarily one fourth the longitudinal component of the total gravitational force. This depends on the number of driven wheels and the grip they have with the ground, as two driven wheels with a good grip have to overcome each half of the total gravitational force of the car. If only one wheel has grip with the ground, this one has to overcome the total gravitational force by itself. This only to say that the model used in this chapter implies a good grip with the ground and four driven wheels sharing the normal load as well as the longitudinal component of the gravitational force. Finally, the mass m represents the vehicle mass associated to each wheel, about one fourth of the total vehicle mass.

5.3 Analysis of the Vehicle Model

Figure 5.2 shows very clearly how the only part of the vehicle model that is not mathematically described (a look-up table is used instead) is the friction characteristic. The aim of this chapter is to estimate the friction characteristic by using the knowledge of the transfer function between the motor torque and the wheel speed. In order to calculate this transfer function, it is therefore necessary to give a local description of the friction characteristic by using the variable η (the derivative of the friction characteristic by respect to the slip ratio), which has been introduced in Section 1.7 (Equation 1.2). Although valid only in the neighbourhood of the operating point, this variable gives a parametric description of the characteristic $\mu_x(\Lambda_t)$ that can be used to calculate the local relationship of any two variables in the system.

In this section I will analyse the vehicle model before and after the interaction with the ground, meaning that I will not consider the friction characteristic but only the slip ratio and the longitudinal tyre force generated. In Section 5.4 I will apply the Taylor approximation, considering only small variation from the operating point, in order to complete the vehicle model with the friction characteristic and to calculate the local relationship between the torque provided and the wheel speed. Because my approach does not requires any direct measurement of the vehicle speed, I will start by substituting it with a function of the wheel speed and the slip ratio. From Equation 5.5 I can isolate the vehicle speed V_v, as expressed by Equation 5.6.

$$V_v = (1 - \Lambda_t) V_w \tag{5.6}$$

I will now calculate the relationship between the slip ratio Λ_t and three forces acting on the vehicle model: the motive force F_m, the external force F_{ext} and the longitudinal tyre force F_x. The relationship between these forces and the time derivatives of wheel speed and vehicle speed are given by Equations 5.2 and 5.3. In order to find the relationship between the slip ratio and the time derivative of wheel speed and vehicle speed, I will calculate the time derivative of Equation 5.5, as expressed by Equation 5.7.

$$\dot{\Lambda}_t = \frac{V_v}{{V_w}^2}\dot{V}_w - \frac{1}{V_w}\dot{V}_v \tag{5.7}$$

In Equation 5.7 it is possible to remove the vehicle speed using Equation

5.6, and to remove the time derivative of wheel speed and vehicle speed using Equations 5.2 and 5.3. This leads to the relationship between slip ratio and the input forces of the model, which is expressed by Equation 5.8.

$$\begin{aligned}\dot{\Lambda}_t &= \frac{1-\Lambda_t}{V_w}\dot{V}_w - \frac{1}{V_w}\dot{V}_v \\ &= \frac{(1-\Lambda_t)(F_m - F_x)}{M_w V_w} - \frac{F_x - F_{ext}}{mV_w} \\ &= \frac{1-\Lambda_t}{M_w V_w}F_m + \frac{1}{mV_w}F_{ext} - \frac{m(1-\Lambda_t)+M_w}{mM_w V_w}F_x\end{aligned} \tag{5.8}$$

Looking at Equation 5.8 one can see that, for a fixed wheel speed, the slip ratio increases with the increase of the motive force or the external force. This is as expected because an additional torque will increase the shear stress in the tyre and therefore the slip ratio (See Chapter 2). An increase of the external force will instead slow down the vehicle, increasing the slip ratio again. It is also intuitive that an increase of the longitudinal tyre force, assuming no variations in the motive force, leads to a reduction in the slip ratio, because this situation can only corresponds to an increase in the grip with the ground (a change in the ground characteristics).

It is important to notice the different sensitivities of the slip ratio to the input forces. First, a variation in the slip ratio at a set wheel speed would require either more force or more time than the same variation at a lower speed. This is mainly because of the definition of slip ratio as a relative speed, so that obtaining the same variation in the slip ratio when the wheel speed is high requires one of the two speeds (the wheel speed or the vehicle speed) to change much more, in absolute term, than when the wheel speed is low. The rate of change of the two speeds is controlled by the three input forces of the vehicle model. For a given wheel speed, the slip ratio is controlled by the external force always with the same sensitivity, proportional to the mass of the vehicle (second term of Equation 5.8). This is because the external force acts directly on the vehicle, increasing or reducing its speed. The sensitivity to the motive force is proportional to the equivalent mass of the wheel but it also depends on the value of the slip ratio (first term of Equation 5.8). The higher the value of the slip ratio, the less control the motive force has over it, until is has no control at all. This is because the wheel can potentially accumulate a large amount of kinetic energy that needs to be reduced in order to gain a significant control of the slip ratio. The sensitivity of the slip ratio to the longitudinal tyre force is also dependent on the slip ratio (third term of Equation 5.8). However, the longitudinal tyre force always maintains some

control over the slip ratio, because it controls directly the acceleration of the vehicle. When the slip ratio is low, the longitudinal tyre force also controls the acceleration of the wheel and the control over the slip ratio increases.

5.4 Small-Signal Transfer Function

Equation 5.8 represents the mathematical relationship between the slip ratio and the three input forces: the motive force, the external force and the longitudinal tyre force. The latter is an input to the vehicle itself, however in my vehicle model I include the interaction with the ground through the friction characteristic $\mu_x(\Lambda_t)$. In this section I will demonstrate how to calculate the local relationship between any variable and the two input forces of my complete model: the motive force and the external force. In particular, the aim of this section is to understand the relationship between these forces and the wheel speed, in the neighbourhood of any operating point.

Given an operating point, the system will be linearised around it and the small-signal transfer function between the inputs and the outputs will be calculated. It is important for the transfer functions to depend only on measurable variables, apart from the slip ratio and the derivative of the longitudinal tyre force with respect to the slip ratio. These two will be estimated by comparing the actual transfer function, measured when the vehicle is running, with its mathematical description. To avoid confusion, the small-signal values will be written in lower case while the values representing the operating point around which the function has been linearised will keep their upper case. Just to recall the theory behind the linearization, it is the first-order approximation of the Taylor series. In general, a function $f(\Lambda_t, V_w, F_m, F_{ext}, F_x)$ can be linearized as shown in Equation 5.9.

$$\begin{aligned} f(\Lambda_t + \lambda_t, V_w + v_w, F_m + f_m, F_{ext} + f_{ext}, F_x + f_x) \approx f(\Lambda_t, V_w, F_m, F_{ext}, F_x) + \\ + \frac{\partial f}{\partial \Lambda_t}\lambda_t + \frac{\partial f}{\partial V_w}v_w + \frac{\partial f}{\partial F_m}f_m + \frac{\partial f}{\partial F_{ext}}f_{ext} + \frac{\partial f}{\partial F_x}f_x \end{aligned} \tag{5.9}$$

The partial derivatives in 5.9 are functions of the operating point and they are therefore constant for any given operating point. For this reason, Equation 5.9 represents a linear relationship among the small-signal values λ_t, v_w, f_m, f_{ext} and f_x. In general, it is always possible to arrange the function $f(\Lambda_t, V_w, F_m, F_{ext}, F_x)$ in order to have $f(\Lambda_t, V_w, F_m, F_{ext}, F_x) = 0$. In this case, the linearized equation presents the simple form expressed by Equation

5.10.

$$0 = \frac{\partial f}{\partial \Lambda_t}\lambda_t + \frac{\partial f}{\partial V_w}v_w + \frac{\partial f}{\partial F_m}f_m + \frac{\partial f}{\partial F_{ext}}f_{ext} + \frac{\partial f}{\partial F_x}f_x \tag{5.10}$$

In order to follow the linearization process step by step, I will rearrange Equation 5.8 into Equation 5.11.

$$0 = (1-\Lambda_t)\, mF_m + M_w F_{ext} - [m\,(1-\Lambda_t) + M_w]\, F_x - mM_w V_w \dot{\Lambda}_t \tag{5.11}$$

Now I can linearize Equation 5.11 around the operating point $[\Lambda_t, V_w, F_m, F_{ext}, F_x]$, as expressed by Equation 5.12.

$$\begin{aligned} 0 = (1-\Lambda_t)\, mf_m - mF_m\lambda_t + M_w f_{ext} + \\ - [m\,(1-\Lambda_t) + M_w]\, f_x + mF_x\lambda_t - mM_w V_w \dot{\lambda}_t - mM_w \dot{\Lambda}_t v_w \end{aligned} \tag{5.12}$$

After localizing the problem in the neighbourhood of the operating point, I can finally remove the longitudinal tyre force from Equation 5.12. This is possible because, in the neighbourhood of the operating point, I have a mathematical description of the friction characteristic provided by the parameter η. The small-signal value f_x can be calculated by linearizing Equation 5.4, as expressed by Equation 5.13.

$$f_x = \mu_x\,(\Lambda_t)\, f_z + \frac{d\mu_x}{d\Lambda_t}F_z\lambda_t \tag{5.13}$$

Because I assume the normal force applied to the tyre F_z to be constant, or at least not to vary substantially, the small-signal value f_z is zero. By considering this and by introducing η as defined in Equation 1.2, I obtain the simple relationship expressed by Equation 5.14.

$$f_x = \eta F_z \lambda_t \tag{5.14}$$

The large-signal value F_x can also be substituted from Equation 5.12, by

rearranging Equation 5.3 into Equation 5.15.

$$F_x = F_m - M_w \dot{V}_w \tag{5.15}$$

It is quite common to use Equation 5.15 to estimate the friction characteristic, by measuring in some way the slip ratio (Delli Colli, Tomassi, and Scarano 2006; Furukawa and Hori 2003; Hori, Toyoda, and Tsuruoka 1998; Sado, Sakai, and Hori 1999). This is usually done by approximating the vehicle speed with the speed of the slowest wheel during acceleration or the speed of the fastest wheel during braking. Sometimes an accelerometer is used, in order to distinguish the high-frequency accelerations of the wheels from the acceleration of the vehicle. In all of these cases, the value of η is calculated through online derivation, which is an operation particularly sensitive to the noise in the measurements. In this chapter I am going to propose a technique which estimates η without passing through the estimation of the coefficient of friction μ_x and the slip ratio Λ_t. In addition, my technique also provides an estimate of the slip ratio Λ_t. After substituting Equations 5.14 and 5.15 into Equation 5.12, I obtain the small-signal relationship between the speed of the wheel and the forces acting on the vehicle. This is expressed by Equation 5.16.

$$\begin{aligned} 0 = (1-\Lambda_t)\, m f_m + M_w f_{ext} + \\ - \left\{ \left[m\,(1-\Lambda_t) + M_w \right] \eta F_z + m M_w \dot{V}_w \right\} \lambda_t - m M_w V_w \dot{\lambda}_t - m M_w \dot{\Lambda}_t v_w \end{aligned} \tag{5.16}$$

In Equation 5.16 the small-signal value of the slip ratio is the only not measurable value, but I can substitute it with a function of the motive force and the wheel speed. This is done by linearizing Equation 5.15 and by substituting λ_t from Equation 5.14, as expressed by Equation 5.17.

$$\lambda_t = \frac{f_m - M_w \dot{v_w}}{\eta F_z} \tag{5.17}$$

By substituting Equation 5.17 into Equation 5.16 I obtain the relationship between the wheel speed and the two input forces of the vehicle model, as expressed by Equation 5.18.

$$mM_wV_w\ddot{v_w} + \left\{\left[m\left(1-\Lambda_t\right)+M_w\right]\eta F_z + mM_w\dot{V_w}\right\}\dot{v_w} - m\eta F_z\dot{\Lambda_t}v_w = \\ = mV_w\dot{f_m} + \left(\eta F_z + m\dot{V_w}\right)f_m - \eta F_z f_{ext} \tag{5.18}$$

Equation 5.18 shows that a complex relationship exists between the wheel speed and the input forces of the vehicle model. It is a differential equation of the second order and it would be impossible to use it in real life because of the noise in the measurements and the nonlinearities of the system. A simplification of the model is therefore required, in order to approximate the relationship expressed in Equation 5.18 with one of a smaller order. To do so I will analyse the system in the frequency domain, considering the Fourier transform of the small-signal variables. A different notation would need to be adopted for the Fourier transform and, in general, the capitalised form is used. In this situation, however, it is more important to differentiate between small-signal values and operating point, and the introduction of a further notation might generate confusion. For this reason, the Fourier transform of the small-signal values will also be written in lower case and the presence of the angular frequency ω or the imaginary constant $\boldsymbol{j}$ in the equations will make implicit their dependence on frequency instead of time. Whenever the distinction would appear less clear, the explicit notation $v_w(t)$ or $v_w(\omega)$ will be used. Equation 5.18 is expressed in the frequency domain by Equation 5.19.

$$\left\{(\boldsymbol{j}\omega)^2 mM_wV_w + \boldsymbol{j}\omega\left\{\left[m\left(1-\Lambda_t\right)+M_w\right]\eta F_z + mM_w\dot{V_w}\right\} - m\eta F_z\dot{\Lambda_t}\right\}v_w = \\ = \left(\boldsymbol{j}\omega mV_w + \eta F_z + m\dot{V_w}\right)f_m - \eta F_z f_{ext} \tag{5.19}$$

Because Equation 5.19 expresses a linear relationship, it is possible to separate the effect of the motive force from the effect of the external force on the wheel speed. In particular, the transfer function between the motive force and the wheel speed is expressed by Equation 5.20, while the transfer function between the external force and the wheel speed is expressed by Equation 5.21.

$$\frac{v_w}{f_m} = \frac{\boldsymbol{j}\omega mV_w + \eta F_z + m\dot{V_w}}{(\boldsymbol{j}\omega)^2 mM_wV_w + \boldsymbol{j}\omega\left\{\left[m\left(1-\Lambda_t\right)+M_w\right]\eta F_z + mM_w\dot{V_w}\right\} - m\eta F_z\dot{\Lambda_t}} \tag{5.20}$$

$$\frac{v_w}{f_{ext}} = -\frac{\eta F_z}{(j\omega)^2 m M_w V_w + j\omega \left\{ \left[m\left(1-\Lambda_t\right) + M_w \right] \eta F_z + m M_w \dot{V}_w \right\} - m\eta F_z \dot{\Lambda}_t} \tag{5.21}$$

5.5 Estimation Technique

Equations 5.20 and 5.21 represent transfer functions of a second-order system and both of them present two non-zero poles. The transfer function between the motive force and the wheel speed also presents one zero at the numerator. These parameters are dependent on the operating point. In particular, they are functions of the mechanical parameters of the vehicle m and M_w, the slip ratio Λ_t, the derivative of the longitudinal tyre force with respect to the slip ratio ηF_z, the time derivative of the slip ratio $\dot{\Lambda}_t$ and the wheel speed $\dot{V}_w$. The two derivatives $\dot{\Lambda}_t$ and $\dot{V}_w$ might look inappropriate for an operating point, but they are in fact the average derivative in any periodic oscillation of the small-signals, so they are unaffected by the small-signal variation. They can also be substituted with functions of F_m and F_{ext}, but this will make the equation unnecessarily complicated. Instead, I can measure the average derivative $\dot{V}_w$ and I can make some considerations over $\dot{\Lambda}_t$. First, assuming the wheel speed and the motive force to be known, it is necessary to measure only one among the vehicle acceleration, the external force and the time derivative, as the others can be calculated from the Equations 5.2 and 5.7. For instance, I could use an accelerometer along the longitudinal axis of the car (Fujimoto, Fujii, and Takahashi 2007) in order to obtain the time derivative of the slip ratio. This solution is outside the scope of my research, as I aim to present an estimation technique which works without any hardware in addition to the motor controller and its in-built current sensor. To do so, it is necessary to accept some compromises: I will therefore assume that the slip ratio does not increase noticeably during a modulation period, which means $\dot{\Lambda}_t \approx 0$. This is true whenever the motive force, the external force or the road surface are not changing appreciably during the modulation period. From now on, I will ignore the contribution of the external force to the wheel speed, assuming that the external forces are slow to change and their oscillation around the modulation frequency is negligible. Under the assumptions $\dot{\Lambda}_t \approx 0$, one of the two poles of the transfer functions approximates to zero and the transfer function between the motive force and the wheel speed can be simplified into Equation 5.22.

$$\frac{v_w}{f_m} = \frac{k_1}{j\omega} * \frac{1 - j\omega\frac{1}{z_1}}{1 - j\omega\frac{1}{p_1}} \tag{5.22}$$

$$k_1 = \frac{\eta F_z + m\dot{V}_w}{\left[m\left(1 - \Lambda_t\right) + M_w\right]\eta F_z + mM_w\dot{V}_w} \tag{5.23}$$

$$p_1 = -\frac{\left[m\left(1 - \Lambda_t\right) + M_w\right]\eta F_z + mM_w\dot{V}_w}{mM_wV_w} \tag{5.24}$$

$$z_1 = -\frac{\eta F_z + m\dot{V}_w}{mV_w} \tag{5.25}$$

In Equations 5.22, 5.23, 5.24 and 5.25, p_1 is the only non-zero pole of the transfer function, z_1 is the zero of the transfer function and k_1 is the gain. The new parameters of the transfer function are linked by Equation 5.26.

$$\frac{k_1 p_1}{z_1} = \frac{1}{M_w} \tag{5.26}$$

Looking at Equations 5.23, 5.24, 5.25 and 5.26, it is easy to see how Equation 5.22 depends on only two unmeasurable parameters: Λ_t and ηF_z. Λ_t gives information about the speed of the vehicle while ηF_z is an indicator of the torque margin between the current operating conditions and the maximum torque that can be transferred to the ground. The aim of my thesis is to estimate these parameters starting from the calculation of the perceived transfer function around the operating point. In order to clarify the dependence between the transfer function and the two parameters p_1 and z_1, it is useful to break down Equation 5.22 into its real and imaginary components, as shown in Equations 5.27 and 5.28.

$$\mathfrak{Re}\left[\frac{v_w}{f_m}\right] = \frac{1}{M_w} * \frac{z_1 - p_1}{\omega^2 + {p_1}^2} \tag{5.27}$$

$$\mathfrak{Im}\left[\frac{v_w}{f_m}\right] = -\frac{1}{\omega M_w} * \frac{z_1 p_1 + \omega^2}{\omega^2 + {p_1}^2} \tag{5.28}$$

For any modulation frequency ω, Equations 5.27 and 5.28 provide two constrains between the perceived transfer function around the operating point and its mathematical description, which depends on the operating point. In this case, the mathematical description of the transfer function is only dependent on two unknown parameters. Hence, these parameters can be calculated by analysing the response of the system at a single frequency.

While Equations 5.27 and 5.28 provide a mathematical relationship between the perceived transfer function and the parameters p_1 and z_1, it is still unclear how to calculate the perceived transfer function from the knowledge of the oscillation of torque applied to the wheels and the resulting oscillation in the wheel speed. The solution relies in the definition of the transfer function, which is the ratio between the Fourier transform (or the Laplace transform, depending on the definition) of the output signal (in this case, the wheel speed) and the Fourier transform of the input signal (in this case, the motive force). My approach is based on the superposition of a cosinusoidal signal to the torque demand set by the driver (or the computer controlling the vehicle, in case of an autonomous vehicle). Under this condition, the input signal of the system, the total motive force applied, is dependent on the torque demand set by the driver. Because any torque applied to the vehicle is well-known, it would potentially be possible to continuously calculate the Fourier transform of this signal. However, in order to simplify the maths behind my approach, I will assume that the torque demand set by the driver is a slow-changing signal, that has a negligible effect on the transfer function around the modulation frequency. Because I limit the analysis of the transfer function around the modulation frequency, I can approximate the input signal to the sole superposed oscillation, which is $f_m(t) = A_0 \cos(\omega_0 t)$. The output signal of the system is the measured wheel speed, which obviously is the result of both the superposed torque oscillation and the slow-changing torque demand set by the driver. The latter, however, will have negligible effects on the Fourier transform of the wheel speed, calculated around the modulation frequency $\frac{\omega_0}{2\pi}$. The real and the imaginary component of the perceived transfer function can be calculated according to the definition of the Fourier transform, as shown in Equation 5.29.

$$\frac{v_w(\omega_0)}{f_m(\omega_0)} = \frac{\int_{-\infty}^{\infty} v_w(t) * e^{-j\omega_0 t}\,\mathrm{d}t}{\int_{-\infty}^{\infty} f_m(t) * e^{-j\omega_0 t}\,\mathrm{d}t} \tag{5.29}$$

Because my approach is focused on the analysis of the transfer function calculated around the modulation frequency $\frac{\omega_0}{2\pi}$, and because the I have assumed a slow-changing offset of torque demand, I can consider both the motive force $f_m(t)$ and the measured wheel speed $v_w(t)$ as periodic functions, with period $T_0 = \frac{2\pi}{\omega_0}$. Being periodic, their ratio does not change if the integral is evaluated for a single period. Equation 5.29 can therefore be modified into Equation 5.30.

$$\begin{aligned}
\frac{v_w(\omega_0)}{f_m(\omega_0)} &= \frac{\int_{t-T_0}^{t} v_w(t) * e^{-j\omega_0 t}\,\mathrm{d}t}{\int_{t-T_0}^{t} f_m(t) * e^{-j\omega_0 t}\,\mathrm{d}t} \\
&= \frac{\int_{t-T_0}^{t} v_w(t) * \cos(\omega_0 t)\;\mathrm{d}t - j\int_{t-T_0}^{t} v_w(t) * \sin(\omega_0 t)\;\mathrm{d}t}{\int_{t-T_0}^{t} f_m(t) * \cos(\omega_0 t)\;\mathrm{d}t - j\int_{t-T_0}^{t} f_m(t) * \sin(\omega_0 t)\;\mathrm{d}t} \\
&= \frac{\int_{t-T_0}^{t} v_w(t) * \cos(\omega_0 t)\;\mathrm{d}t - j\int_{t-T_0}^{t} v_w(t) * \sin(\omega_0 t)\;\mathrm{d}t}{\int_{t-T_0}^{t} A_0\cos(\omega_0 t) * \cos(\omega_0 t)\;\mathrm{d}t - j\int_{t-T_0}^{t} A_0\cos(\omega_0 t) * \sin(\omega_0 t)\;\mathrm{d}t} \\
&= \frac{\int_{t-T_0}^{t} v_w(t) * \cos(\omega_0 t)\;\mathrm{d}t - j\int_{t-T_0}^{t} v_w(t) * \sin(\omega_0 t)\;\mathrm{d}t}{\frac{A_0 T_0}{2} + j0} \\
&= \frac{2\int_{t-T_0}^{t} v_w(t) * \cos(\omega_0 t)\;\mathrm{d}t}{A_0 T_0} - j\frac{2\int_{t-T_0}^{t} v_w(t) * \sin(\omega_0 t)\;\mathrm{d}t}{A_0 T_0}
\end{aligned} \tag{5.30}$$

Equation 5.30 shows that the real and the imaginary component of the transfer function can be calculated by simple integration along time of the

products between the measured wheel speed and two simple signals, a sine and a cosine, oscillating with period T_0. While Equation 5.30 is expressed in continuous time, it is possible to approximate the real and the imaginary component of the transfer function, using a discrete number of samples of the wheel speed v_w. This is necessary in order to compute their value with a discrete number of operation. By assuming the samples of the wheel speed to be equally spaced, I will define the sampling time T_s as the time interval between different samples. The sampling time T_s should precisely divide the modulation period T_0 into an integer number of intervals N_s. This is necessary in order to remove any spectral leakage generated by the proposed calculation, at least for what concerns the fundamental oscillation, the one that excites the system. Because of the non-linearity of the vehicle model, the frequency spectrum of the wheel speed might present other components, besides the fundamental one, but these will be of a secondary importance. T_s should be much smaller than T_0 (at least one tenth), in order to better approximate the continuous response of the system with its sampled measurements. Under these conditions, the real and the imaginary component of the perceived transfer function can be calculated according to Equations 5.31 and 5.32.

$$\mathfrak{Re}\left[\frac{v_w\left(\omega_0\right)}{f_m\left(\omega_0\right)}\right] = \frac{2\sum_{k=0}^{N_s-1} v_w\left(t-kT_s\right) * \cos\left(\omega_0\left(t-kT_s\right)\right)}{A_0 N_s} \tag{5.31}$$

$$\mathfrak{Im}\left[\frac{v_w\left(\omega_0\right)}{f_m\left(\omega_0\right)}\right] = -\frac{2\sum_{k=0}^{N_s-1} v_w\left(t-kT_s\right) * \sin\left(\omega_0\left(t-kT_s\right)\right)}{A_0 N_s} \tag{5.32}$$

From the measured real and imaginary components of the transfer function, it is possible to calculate the parameters p_1 and z_1 by inverting the system of Equations 5.27 and 5.28, as expressed by Equations 5.33 and 5.34.

$$p_1 = -\frac{\omega_0 M_w \mathfrak{Im}\left[\frac{v_w(\omega_0)}{f_m(\omega_0)}\right] + 1}{M_w \mathfrak{Re}\left[\frac{v_w(\omega_0)}{f_m(\omega_0)}\right]} \tag{5.33}$$

$$z_1 = \frac{\omega_0\left[\omega_0 M_w\left(\mathfrak{Im}^2\left[\frac{v_w(\omega_0)}{f_m(\omega_0)}\right] + \mathfrak{Re}^2\left[\frac{v_w(\omega_0)}{f_m(\omega_0)}\right]\right) + \mathfrak{Im}\left[\frac{v_w(\omega_0)}{f_m(\omega_0)}\right]\right]}{\mathfrak{Re}\left[\frac{v_w(\omega_0)}{f_m(\omega_0)}\right]} \tag{5.34}$$

Once p_1 and z_1 are calculated, it is possible to obtain the slip ratio and the derivative of the longitudinal tyre force with respect to the slip ratio by inverting the system of Equations 5.24 and 5.25, as expressed by Equations 5.35 and 5.36.

$$\Lambda_t = 1 + \frac{M_w}{m} - \frac{M_w}{m} * \frac{p_1 V_w + \dot{V}_w}{z_1 V_w + \dot{V}_w} \tag{5.35}$$

$$\eta F_z = -m\left(z_1 V_w + \dot{V}_w\right) \tag{5.36}$$

5.6 Analysis and Simplification of the Transfer Function

Now that a mathematical description of the estimation technique has been presented, it is useful to analyse this model to see if a reasonable approximation can lead to a simpler calculation. First, by multiplying numerator and denominator of Equation 5.25 by M_w and comparing it to Equation 5.24 it is possible to see how the zero of the transfer function is always smaller than its pole, in absolute value. This knowledge will allow approximation of the second-order system in Equation 5.22 to a first-order one.

5.6.1 High Frequency

Increasing the modulation frequency ω, the factor $1 - j\omega\frac{1}{z_1}$ tends to $-j\omega\frac{1}{z_1}$ faster than $1 - j\omega\frac{1}{p_1}$ tends to $-j\omega\frac{1}{p_1}$, because the zero is smaller than the pole. Therefore, if $\left|\frac{\omega}{z_1}\right| \gg 1$ the system can be described by a first-order transfer function, as expressed by Equation 5.37.

$$\frac{v_w}{f_m} \approx \frac{mV_w}{\left[m\left(1-\Lambda_t\right)+M_w\right]\eta F_z + mM_w\dot{V}_w} * \frac{1}{1 + j\omega\frac{mM_wV_w}{[m(1-\Lambda_t)+M_w]\eta F_z + mM_w\dot{V}_w}} \tag{5.37}$$

To give a numerical example of how large the modulation frequency ω should be to allow the previous approximation, I will assume the vehicle run-

ning on an horizontal surface, so that the normal force is equal to the mass times the gravitational acceleration g. In such case it should be $\omega \gg \frac{\dot{V}_w + g\eta}{V_w}$. On tarmac, μ_x can reach a peak value around 1, with the corresponding slip ratio around 0.2; this means the average η in condition of low slip ratio is around $\frac{1}{0.2} = 5$. Knowing the value of g around 10, the product $g\eta$ is in the order of 50 m/s^2 which corresponds to an acceleration of about 180 km/h in one second. This is much larger than any wheel acceleration can reasonably be, therefore the term $\dot{V}_w$ can be ignored. According to the previous assumption, to have $\left|\frac{\omega}{z_1}\right| \gg 1$ it would be necessary to have $\omega \gg \frac{50}{V_w}$. This correspond to a frequency of 10 Hz or larger for a wheel speed of 30 km/h.

If the frequency is so high that also $\left|\frac{\omega}{p_1}\right| \gg 1$ the system can be described with a single pole in 0, as expressed by Equation 5.38.

$$\frac{v_w}{f_m} \approx \frac{1}{j\omega M_w} \tag{5.38}$$

There is usually a factor of at least 10 between the mass of the vehicle m and the equivalent mass of the wheel M_w and in conditions of low slip ratio, this is the same factor between z_1 and p_1. According to the same assumptions made about the value of z_1, to have $\left|\frac{\omega}{p_1}\right| \gg 1$ it would be necessary to have $\omega \gg \frac{500}{V_w}$. This correspond to a frequency of 100 Hz or larger for a wheel speed of 30 km/h. It is important to notice that at such high frequency any information about the operating point is lost as the only inertia perceived from the motor is the moment of inertia of the wheel. If the aim is to estimate the operating point from the response of the wheel speed it is therefore necessary to operate at lower frequencies than this.

5.6.2 Low Frequency

Lowering the modulation frequency ω, the factor $1 - j\omega\frac{1}{p_1}$ tends to 1 faster than $1 - j\omega\frac{1}{z_1}$, because the zero is smaller than the pole. Eventually the frequency could be low enough that $1 \gg \left|\frac{\omega}{z_1}\right|$ so that the system can be described with a single pole in 0, as expressed by Equation 5.39.

$$\frac{v_w}{f_m} \approx \frac{\eta F_z + m\dot{V}_w}{j\omega\left\{\left[m\left(1-\Lambda_t\right)+M_w\right]\eta F_z + mM_w\dot{V}_w\right\}} \tag{5.39}$$

In Equation 5.39 one can identify the apparent inertia perceived at the wheel for low frequencies. This correspond to the term

$\frac{\eta F_z + m\dot{V}_w}{[m(1-\Lambda_t)+M_w]\eta F_z + mM_w\dot{V}_w}$. It is interesting to notice how the apparent inertia changes between the equivalent wheel mass M_w when the wheel is skidding on the ground (therefore $\Lambda_t = 1$) and the sum of the equivalent wheel mass and the vehicle mass m when there is complete adhesion with the ground (therefore $\Lambda_t = 0$) and the average wheel acceleration $\dot{V}_w$ is 0. This is intuitive because, when there is no friction with the ground, the torque provided to the wheel contributes only to increase its rotational speed, therefore only the inertia of the wheel is perceived. When there is full adhesion between the tyre and the ground, the vehicle accelerates together with the wheel and the inertia of both the body and the wheels is perceived. Equation 5.39 is often simplified under the assumption that $|\eta F_z| \gg \left|m\dot{V}_w\right|$, as expressed by Equation 5.40 (Hori, Toyoda, and Tsuruoka 1998).

$$\frac{v_w}{f_m} \approx \frac{1}{j\omega\left[m\left(1-\Lambda_t\right)+M_w\right]} \tag{5.40}$$

From Equation 5.40 it appears very clear that the apparent inertia changes between M_w and $(m + M_w)$, for different values of slip ratio. Its simple form is the main reason why Equation 5.40 is often used to estimate the slip ratio from the wheel response to a given torque. Please note that the approximation $|\eta F_z| \gg \left|m\dot{V}_w\right|$ does not hold when η is close to 0, which is when the maximum of the available longitudinal tyre force is applied to the ground. In that case, Equation 5.39 should be used instead. Another important remark is that both Equations 5.39 and 5.40 represent the transfer function between the motive force and the wheel speed and they ignore the contribution of the external force to the wheel speed. While for medium and high frequencies I previously ignored this contribution by assuming that most of the external forces acting on the vehicle are slow changing, it is not possible to ignore their effect at low frequencies.

5.6.3 High Frequency, Low Slip Ratio

Observing Equation 5.37 it is possible to make some considerations. First, the equation is always dependent on the slip ratio and the derivative of the longitudinal tyre force with respect to it, however these two variables are now combined into the term $\left[m\left(1-\Lambda_t\right)+M_w\right]\eta F_z$. There is now only one unknown parameter in Equation 5.37, therefore it is not necessary to compute both the real and the imaginary part of the transfer function to estimate it. The estimation process requires to consider only one among the real part, the imaginary part and the gain of the system at a given frequency. It could also use two of these data in order to reinforce the measurement against noise. This

approach would lead to much more accurate results than the approach that estimates two unknown parameters using both the real and the imaginary part of the transfer function, as the errors in both the measurements and the correlation between the calculations of the two parameters would negatively affect the results.

The real problem is that, if the slip ratio and the derivative of the longitudinal tyre force are combined into one term, now it is not possible to discern between the two! There is no solution to this problem, apart from making assumptions over the value of one of the two parameters. Just for the sake of the argument I will show how the transfer function changes for very small value of the slip ratio. If $1 \gg \Lambda_t$, then it is possible to approximate the term $(1 - \Lambda_t)$ with 1. Moreover, if the slip ratio is low the value of η is probably large enough that $|\eta F_z| \gg \left|m\dot{V}_w\right|$. By applying the previous approximations I obtain the transfer function expressed by Equation 5.41.

$$\frac{v_w}{f_m} \approx \frac{mV_w}{(m + M_w)\,\eta F_z} * \frac{1}{1 + j\omega \frac{mM_wV_w}{(m+M_w)\eta F_z}} \tag{5.41}$$

Equation 5.41 can be used to estimate the derivative of the longitudinal tyre force with respect to the slip ratio, for very low slip ratios. It is possible to simplify Equation 5.41 further by considering that in common road cars the equivalent wheel mass is negligible compared to the mass of the vehicle so $M_w + m \approx m$. By applying the previous approximation to Equation 5.41 I obtain the transfer function expressed by Equation 5.42.

$$\frac{v_w}{f_m} \approx \frac{V_w}{\eta F_z} * \frac{1}{1 + j\omega \frac{M_wV_w}{\eta F_z}} \tag{5.42}$$

Equation 5.42 holds well if the slip ratio is lower than 0.1 and it reflects an intuitive behaviour of the vehicle, already discussed in Section 1.7 as a simplified explanation of my estimation method. In fact, by assuming that small-signal variations in the wheel speed do not correspond to variations in the vehicle speed at high frequency (because of the large inertia of the vehicle, the speed of the vehicle can be considered constant), the small-signal value of the slip ratio would depend entirely on the wheel speed, as expressed by Equation 5.43.

$$\lambda_t \approx \frac{v_w}{V_w} \tag{5.43}$$

By applying Equation 5.43 to Equation 5.17 and calculating the Fourier transform I obtain exactly Equation 5.42. This is a very intuitive result and it could be used for a rough estimate of the derivative of the longitudinal tyre force although, if some assumption can be made over the slip ratio, it would be more accurate to use Equation 5.37 directly.

5.7 Simulation Results

The "Single wheel" vehicle model in Figure 5.2 has been used to simulate the proposed estimation algorithm in Simulink. The mechanical parameters used for the vehicle model are listed in Table 5.1. The model is set to run on a flat surface, with the vehicle gravitational force being the only force normal to the ground. A continuous torque of 200 Nm is provided to the wheels, while no external force is acting on the vehicle. Such configuration causes the slip ratio to set at a stable value, while the vehicle speed and the wheel speed are constantly increasing. In order to test the proposed approach, a cosinusoidal signal of 5 Nm of amplitude is superposed to the continuous torque. The estimation is tested using four different modulation frequencies: 2 Hz, 0.5 Hz, 0.2 Hz and 10 Hz. The results of the simulation are discussed in the following subsections.

Table 5.1: *Mechanical parameters used in simulation*

m	250 kg
I_y^w	1 $kg * m^2$
R_e	0.3 m

5.7.1 Modulation Frequency of 2 Hz

Figure 5.3 shows the motive force applied to the vehicle model, and the resulting increase of the wheel speed and the vehicle speed with the time. Figure 5.3 clearly shows the cosinusoidal oscillation (at a frequency of 2 Hz) of torque, superposed to its continuous value (200 Nm), although in the figure the torque is scaled to be represented as a motive force. The amplitude of the torque oscillation is 5 Nm, which translates into an oscillation of the motive force of approximately 16 N (5 Nm/R_e). The wheel speed and the vehicle speed seem to linearly increase with the time. In reality, they are also oscillating because of the oscillation in the motive force. However, the oscillation cannot be seen

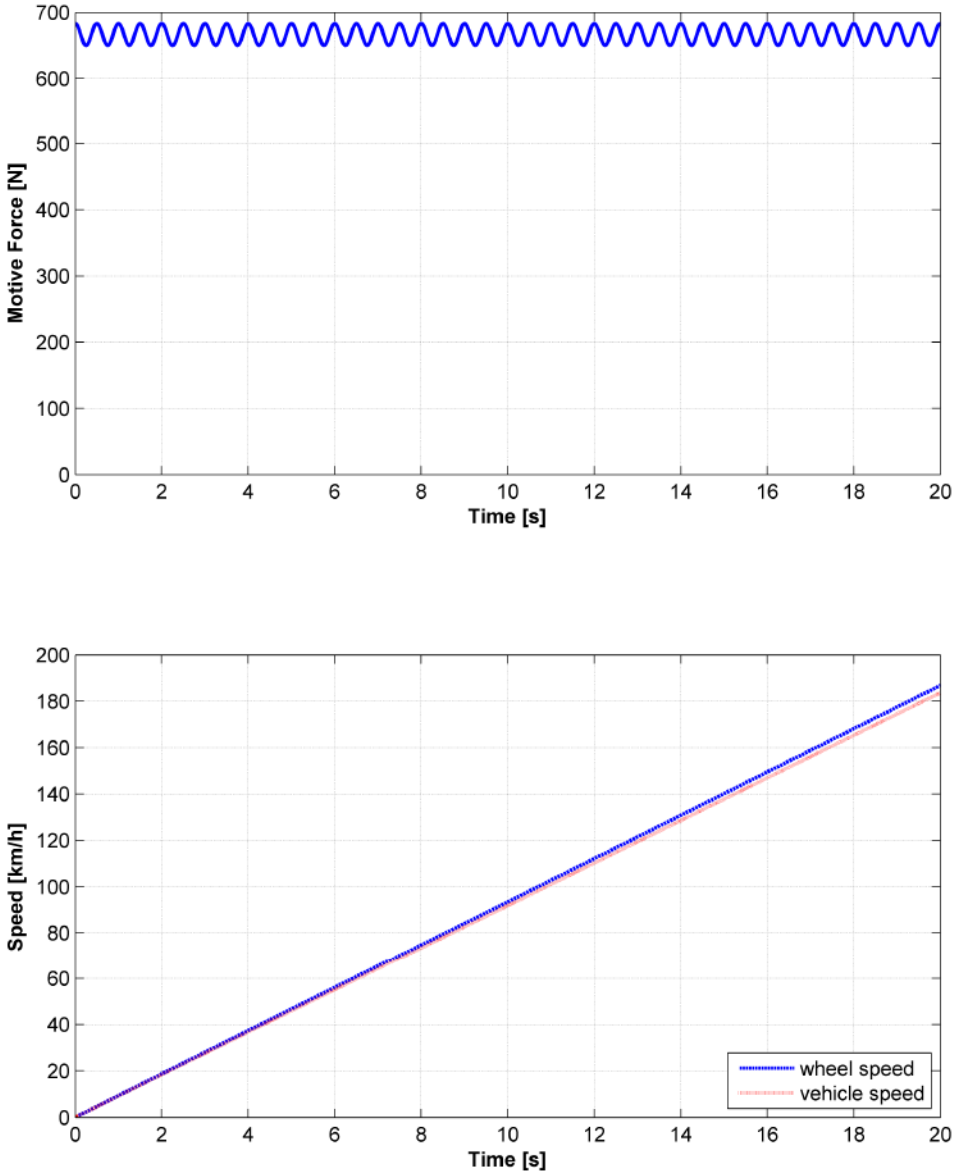

Figure 5.3: *The motive force causes a continuous increase of the wheel speed and the vehicle speed during the simulation time; both the speeds present a continuous oscillation around the modulation frequency, but this is not visible because of the scale of the plot*

at the scale of the plot in Figure 5.3. The difference in slope between the increase of the wheel speed and the increase of the vehicle speed is expression of the constant slip ratio, which corresponds to a constant relative difference between the two speeds.

Because the normal force is constant at $F_z = mg$, the projection of the operating point on the friction characteristic sets around a stable position as soon as the slip ratio Λ_t sets to a stable value. In short, both the targets of the estimation, Λ_t and ηF_z, reach a stable value after a quick transient

at the beginning of the simulation. It is important to notice that, according to Equations 5.24 and 5.25, the operating point around which the transfer function is linearised depends on the wheel speed. Because the wheel speed is continuously increasing, the operating point is also moving, together with p_1 and z_1. This is true regardless from the fact that the projection of the operating point on the friction characteristic reaches a stable position.

The oscillation superposed to the continuous motive force and the resulting oscillation in the wheel speed, filtered from the continuous component, are shown in Figure 5.4. These are the input and the output of the transfer function of the vehicle model, linearised around the operating point. The aim of the proposed approach is to use these two signals to estimate the pole p_1 and the zero z_1 of the transfer function. From them, and from the measure of the large-signal value of the wheel speed (ignoring the small-signal periodic variation), it will be possible to calculate the slip ratio Λ_t and the derivative of the longitudinal tyre force by respect to the slip ratio ηF_z, according to Equations 5.35 and 5.36.

It is worth spending a few words about the timing of the simulation. In order to evaluate the effects of measurement sampling on the estimation, I tried the proposed estimation algorithm at different rates of execution. First, I started with 1 ms, which is a value achievable by most of the cheapest microcontroller. In order to have a reliable simulation of the vehicle model (which is continuous in time) I decided to use a very short simulation step compared to the dynamics of the system, setting it to 10 μs. Using these settings and a modulation frequency of 2 Hz, I obtained the estimation of p_1 and z_1 which is shown in Figure 5.5.

The proposed estimation algorithm takes a whole modulation period to produce any meaningful result, because of the integrals in Equations 5.31 and 5.32. This is the reason why the estimation returns unacceptable values during the initial 0.5 s. It is also the reason behind the delay between the instantaneous parameters of the transfer function (the pole p_1 and the zero z_1) and their estimated counterpart. In fact, the estimation algorithm computes all the measurements of the wheel speed taken during the last modulation period, hence its output corresponds to something similar to an average of the instantaneous parameters of the transfer function during this time. Figure 5.5 shows that the estimation output lags behind the instantaneous values of the parameters by a little less than a modulation period (0.5 s), as expected. In order to reduce this delay, it is necessary to use a higher modulation frequency. Taking all of this into consideration, Figure 5.5 shows a reasonably accurate estimation of p_1 and z_1.

It is interesting to notice that Figure 5.5 shows a small oscillation in the

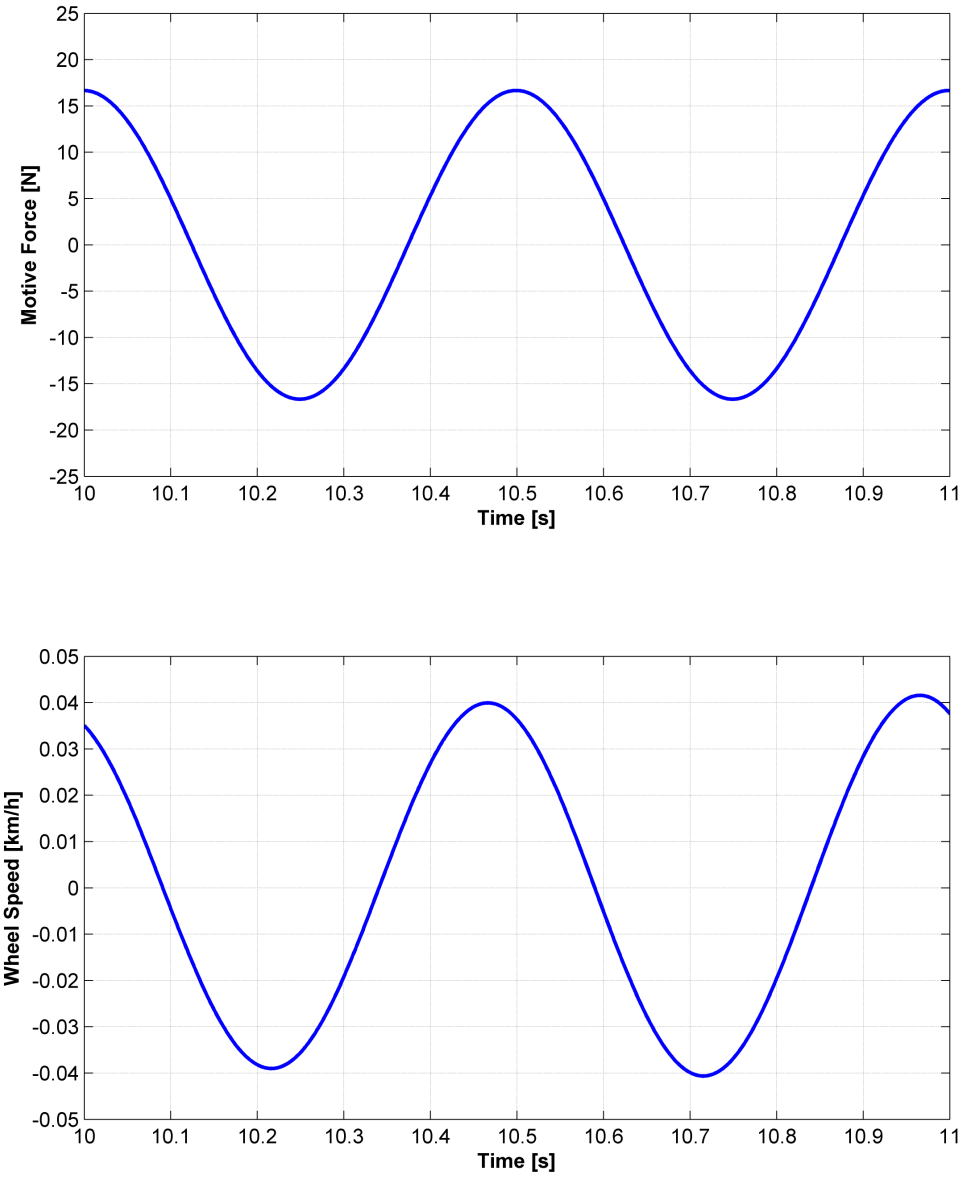

Figure 5.4: *Modulation of the motive force and resulting oscillation in the wheel speed; both these signals are filtered from the continuous component*

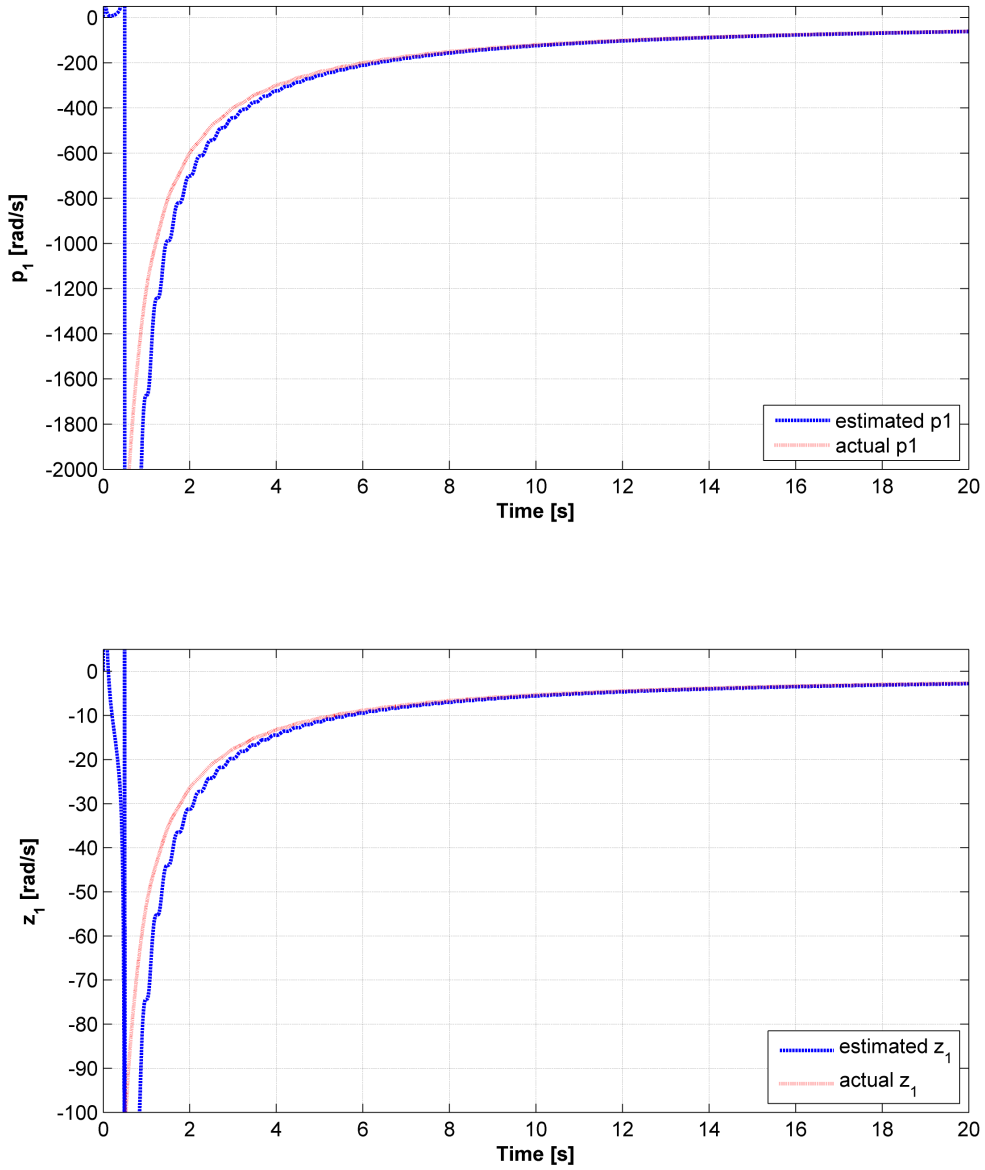

Figure 5.5: *Estimation of p_1 and z_1, using a modulation frequency of 2 Hz and a sampling period of 1 ms (500 samples per modulation period)*

estimated values, which is due to the oscillation in the operating point. Most of the equations derived in this chapter are based, in fact, on the assumption that it is possible to apply a small oscillation in a non-linear system and, if the oscillation is small enough, the latter would behave as a linear system. This is approximately true, but because of the oscillations in the input, the operating point will move a little and the transfer function will change slightly, which does not happen in linear systems. The result is that the final output of the estimation algorithm presents a small oscillation around the expected value, as shown in Figure 5.5.

Figure 5.6 shows the derivative of the longitudinal tyre force ηF_z and the slip ratio Λ_t, calculated from the estimated pole p_1 and the zero z_1 according to Equations 5.35 and 5.36. The oscillation in the estimated value is much more noticeable than it is for the pole p_1 and the zero z_1. This oscillation can be removed at the cost of adding another modulation period of delay to the estimation response. In fact, it is possible to average the output of the estimation during one modulation period, hence averaging the variations in the transfer function. The result of this operation is shown in Figure 5.7.

Figure 5.7 shows a good estimation of the derivative of the longitudinal tyre force; however, it shows an error in the estimation of the slip ratio that increases with the increase of the wheel speed. Given that the estimations of p_1 and z_1 look pretty accurate, this can only mean that the calculation of the slip ratio is particularly sensitive to very small errors in one of these two parameters. Looking at Equation 5.35, in fact, it is easy to see how a small error in the pole or in the zero of the transfer function would translate in a much bigger error in the slip ratio, if the wheel speed is sufficiently large.

To better understand the source of this problem, it is useful to zoom in on Figure 5.5, in order to better evaluate the errors in the estimations of p_1 and z_1, particularly for high values of wheel speed (corresponding to high values of simulation time). This is shown in Figure 5.8. The relative error cannot be evaluated at a single instant because, as I stated before, the estimation output is slightly late compared to the instantaneous parameters of the transfer function; however, it is possible to see that, while the estimation of p_1 is delayed by roughly 0.3 s, the estimation of z_1 is delayed by roughly 1 s. This means that there is indeed an error in the calculation, because whenever the pole is correctly estimated, the estimation of the zero presents an error that is close to 3.5% (0.1/2.8).

Is this error in the estimation caused by the approximation of the continuous system (the vehicle) with a discrete one, due to sampling? In order to answer this question, I have reduced the sampling period and the execution period (they are linked because the algorithm runs at every sampling event) of

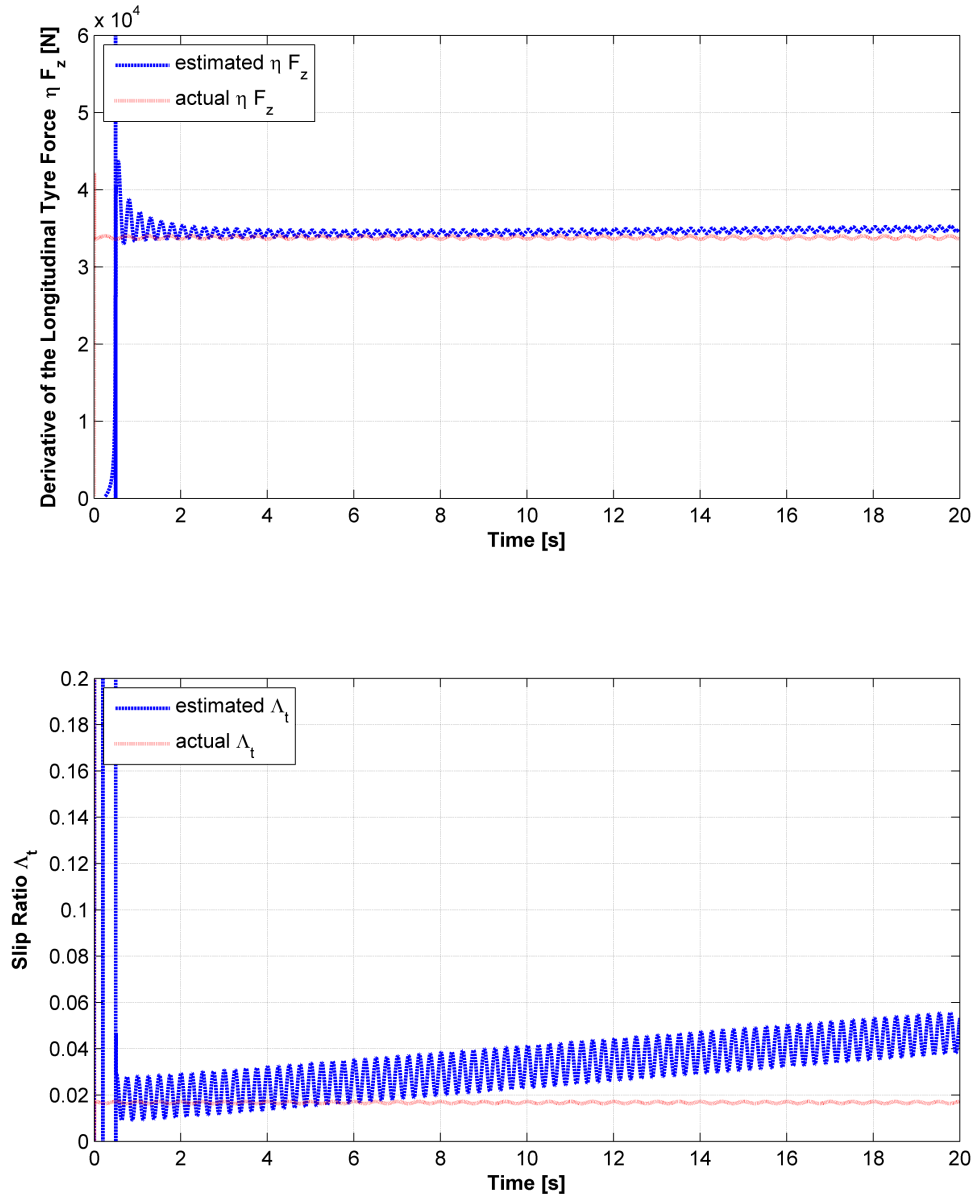

Figure 5.6: *Estimation of the derivative of the longitudinal tyre force ηF_z and the slip ratio Λ_t, using a modulation frequency of 2 Hz and a sampling period of 1 ms (500 samples per modulation period)*

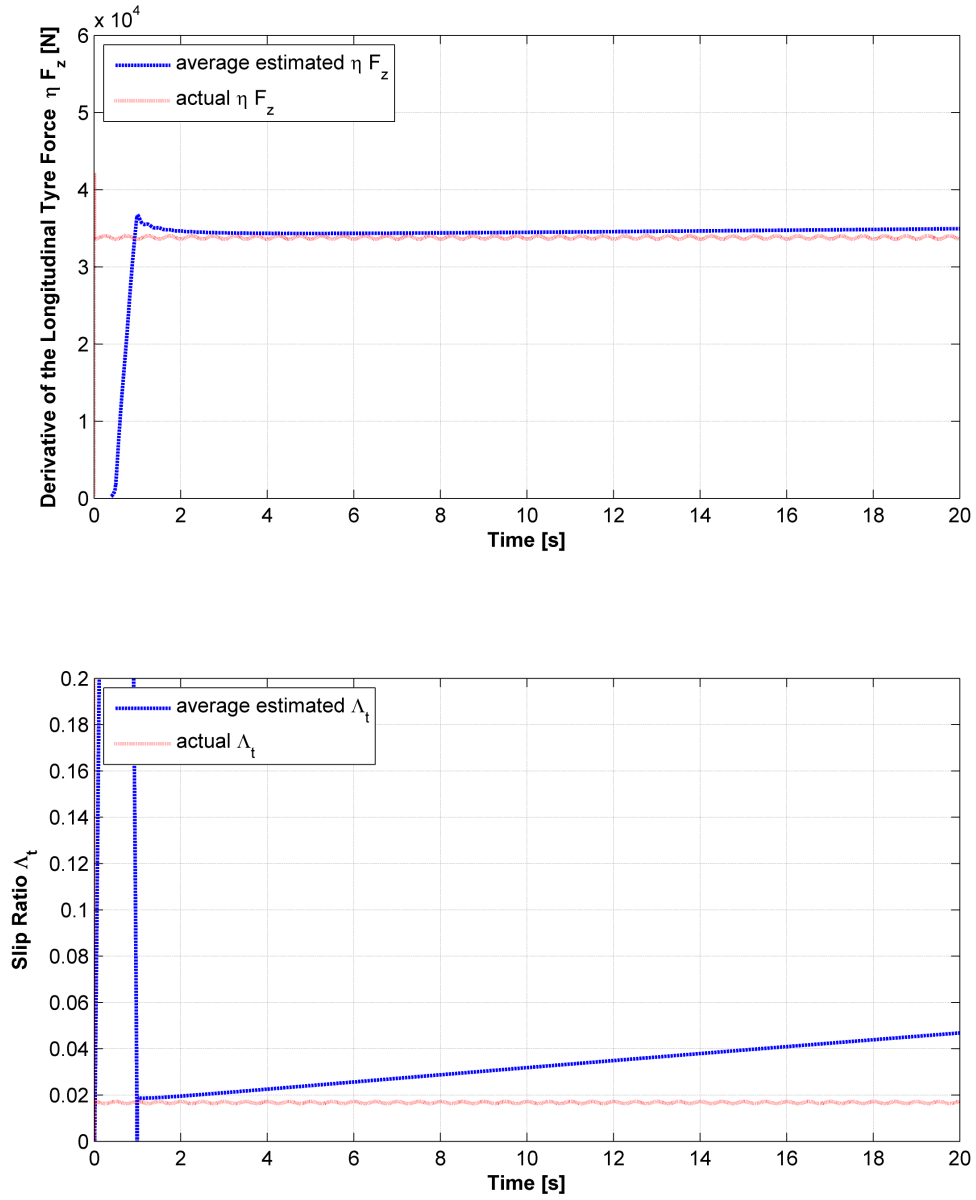

Figure 5.7: *Estimation of the derivative of the longitudinal tyre force ηF_z and the slip ratio Λ_t, averaged during a modulation period, using a modulation frequency of 2 Hz and a sampling period of 1 ms (500 samples per modulation period)*

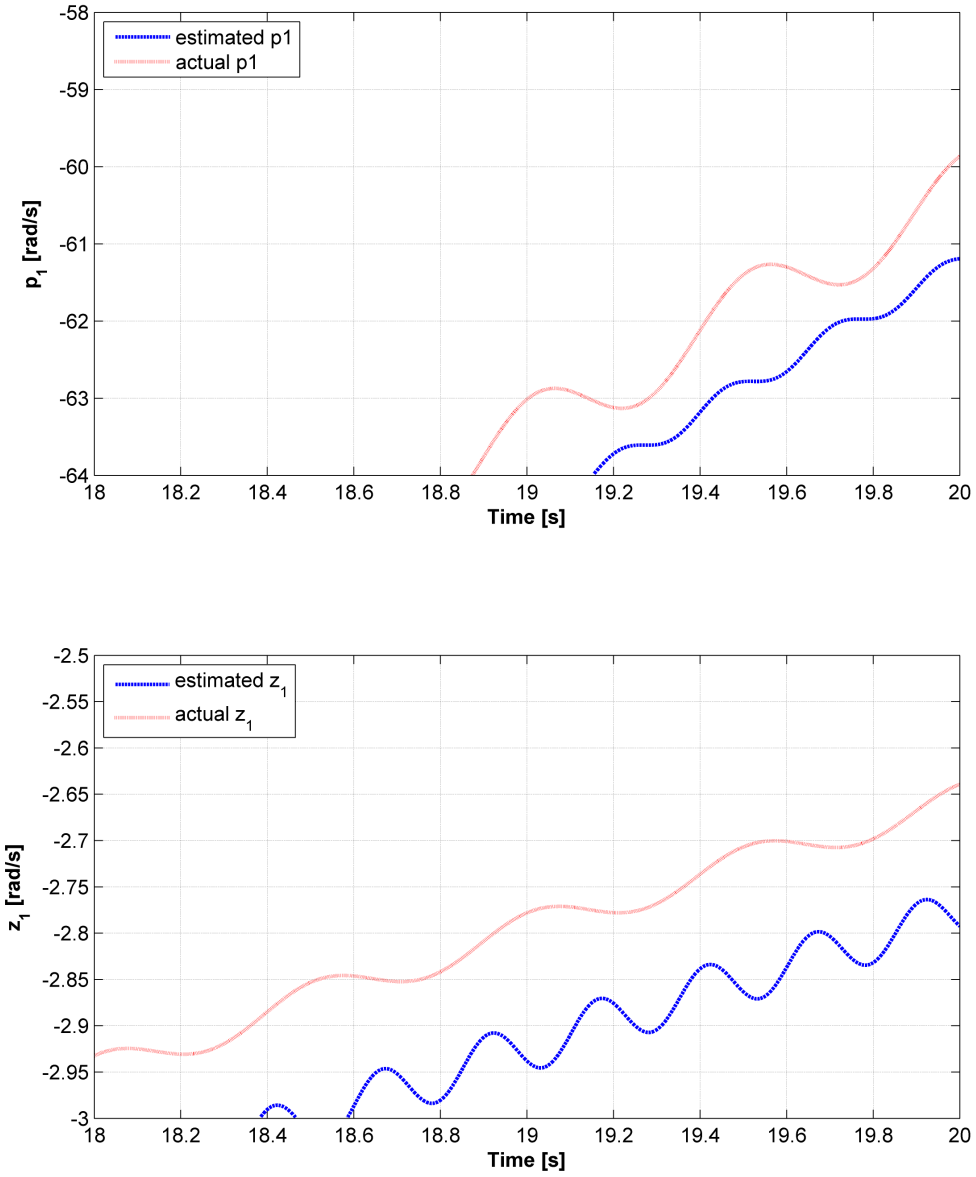

Figure 5.8: *Estimation of p_1 and z_1, using a modulation frequency of 2 Hz and a sampling period of 1 ms (500 samples per modulation period); zoom close to the final value of the estimated parameters, in order to evaluate the error in the estimation*

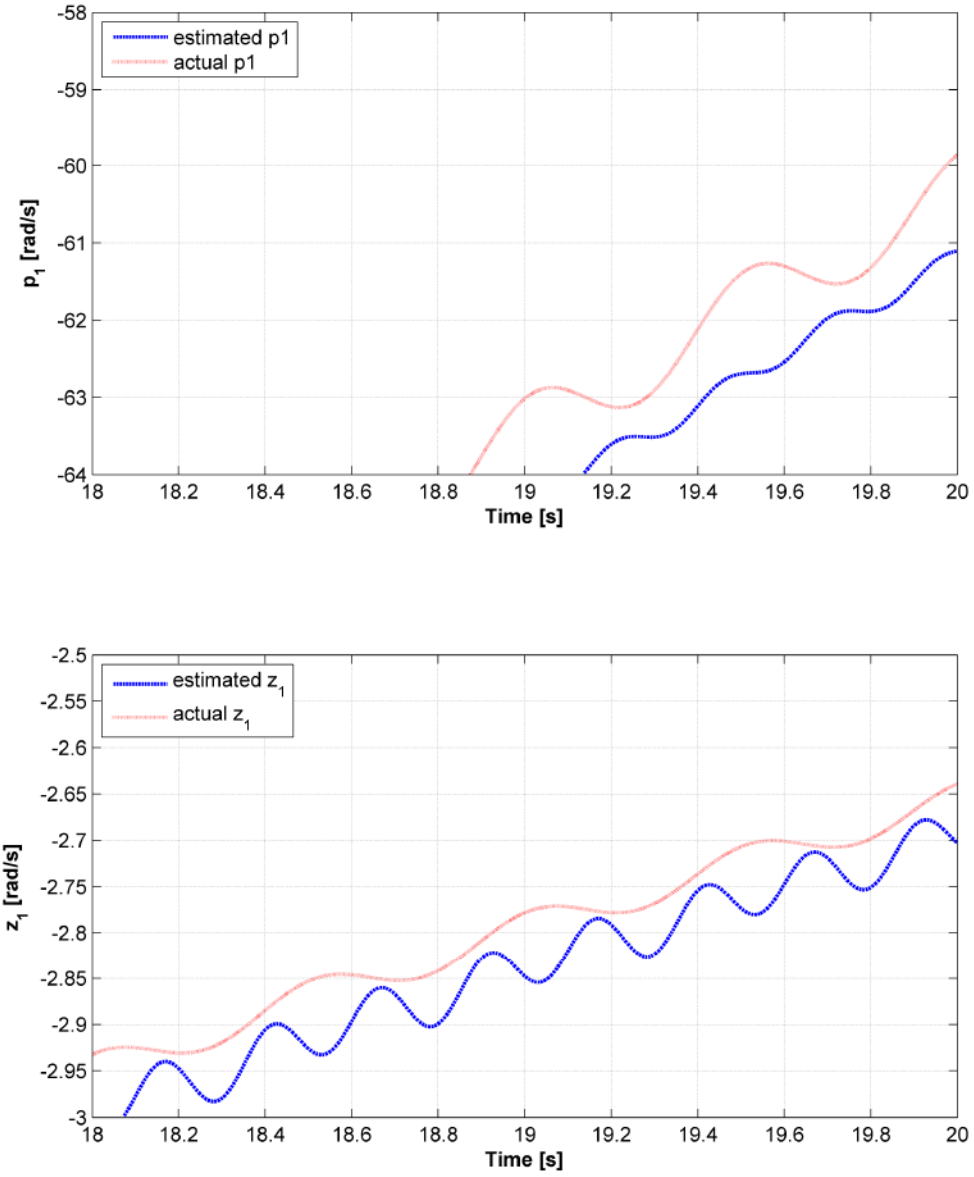

Figure 5.9: *Estimation of p_1 and z_1, using a modulation frequency of 2 Hz and a sampling period of 10 μs (50000 samples per modulation period); zoom close to the final value of the estimated parameters, in order to evaluate the error in the estimation*

the proposed estimation algorithm. I have tried with 10 μs, which is a value easily achievable by an FPGA. At the same scale of Figure 5.5, the results are visually identical and therefore I decided not to duplicate the figure; however, the enlarged plot (same scale of Figure 5.8) is shown in Figure 5.9.

In Figure 5.9 both the estimation of p_1 and the estimation of z_1 are delayed of roughly 0.3 s and the error in the estimation, if any, seems greatly reduced. This hypothesis is confirmed by the filtered (averaged in a modulation period) results of the calculation of ηF_z and Λ_t, which are shown in Figure 5.10. These

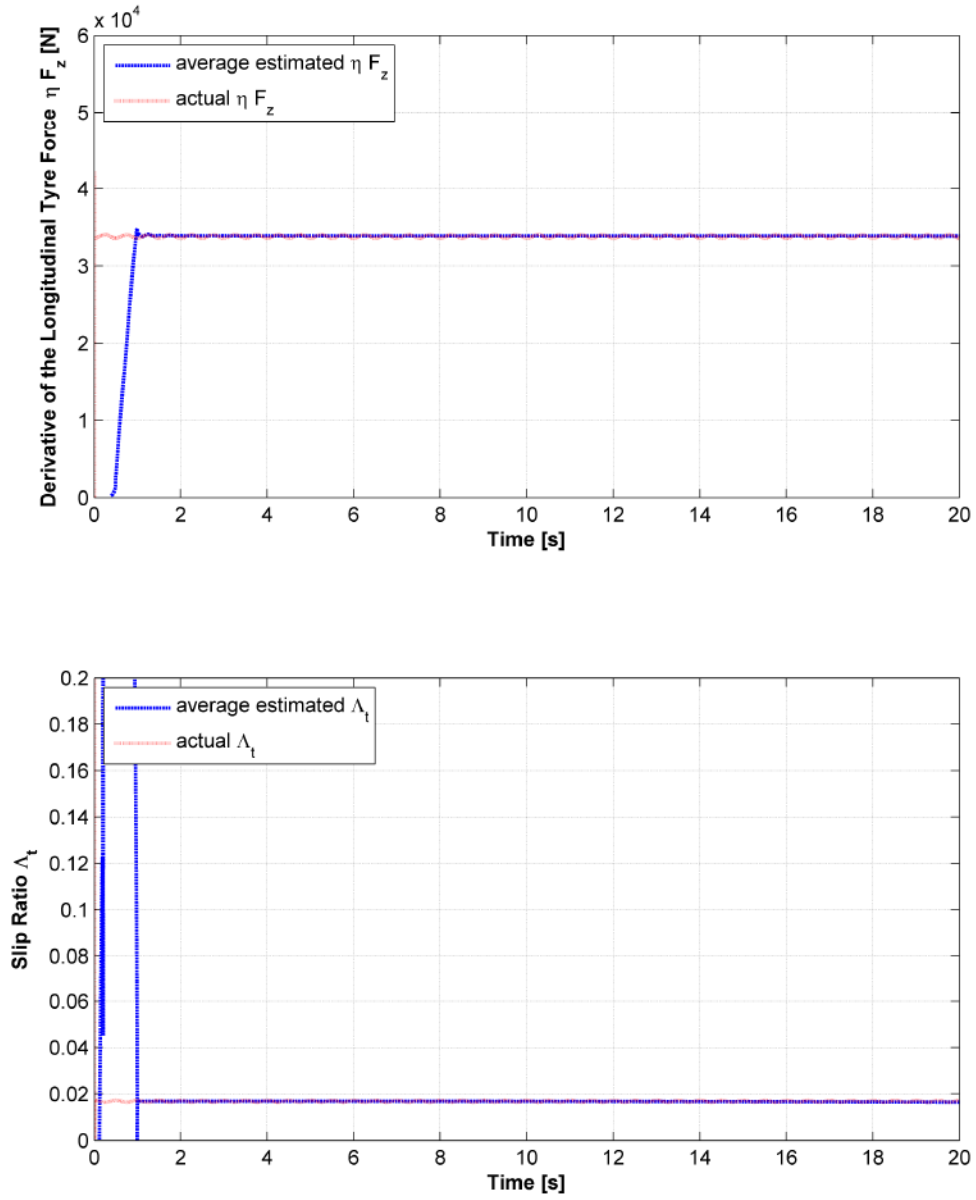

Figure 5.10: *Estimation of the derivative of the longitudinal tyre force ηF_z and the slip ratio Λ_t, averaged during a modulation period, using a modulation frequency of 2 Hz and a sampling period of 10 μs (50000 samples per modulation period)*

results appear now to be very accurate and usable.

5.7.2 Analysis of the Estimation Error

I have just demonstrated that it is possible to reduce the error in the estimation by increasing the sampling rate. Now I will focus on the causes of this error, in order to be able to assess the accuracy of any estimation and, maybe, to propose alternative ways to reduce the error. The error in the estimation of ηF_z and Λ_t is the result of three factors:

- The error in the calculation of the real and the imaginary part of the perceived transfer function of the system, due to the error in the measurements and the approximation in the calculation.
- The sensitivity of the calculation of the parameters p_1 and z_1 to the errors in the real and the imaginary part of the perceived transfer function.
- The sensitivity of the calculation of the parameters ηF_z and Λ_t to the errors in the parameters p_1 and z_1.

I have already discussed how the third factor of the list (the sensitivity of ηF_z and Λ_t to the errors in p_1 and z_1) has a major impact in the proposed simulation. In fact, even for a constant error in p_1 and z_1, the estimation of ηF_z and Λ_t worsen with the increase of the wheel speed (according to Equations 5.36 and 5.35).

The second factor of the list (the sensitivity of p_1 and z_1 to the errors in the real and the imaginary part of the perceived transfer function) has also an important effect on the estimation. However, according to Equations 5.33 and 5.34, the sensitivity does not vary with the operating point and it is only dependent on the mechanical parameters of the system and on the modulation frequency. Because of this, the only controllable way to keep this sensitivity low is to reduce the modulation frequency.

The first factor of the list (the generation of the error in the calculation of the real and the imaginary part of the perceived transfer function) is surely the most complicated to evaluate, particularly when measurement noise is affecting the calculation. In order to remove this source of variability, the proposed simulation does not include any simulation of the measurement noise. Other sources of error are the numerical representation of the variables (causing approximation errors in the calculation), the resolution of the samples (causing quantisation errors) and the number of samples per modulation period (causing discretisation errors). Given that the simulation uses 64-bit floating-point representation of the data, I will consider the errors in the calculation due to numerical approximation and the errors due to quantisation to be negligible. This will allow to focus on the most controllable source of error in the proposed algorithm: the discretisation. The discretisation is critical because the proposed algorithm operates by calculating the real and the imaginary part of the perceived transfer function, which are nothing but a different representation of the gain and the phase shift between the motive force and the wheel speed. When the changes in the gain or in the phase shift are minimal it is very difficult to detect them, unless a high number of samples per modulation period is used.

The results previously presented shows that 500 samples per modulation period (1 ms of sampling period with a modulation frequency of 2 Hz) are not always enough to produce an accurate estimation. The need for such a high number of samples is an indication of the high sensitivity of the proposed algorithm to discretisation, at least under specific conditions. I will now try to identify the critical conditions when this is true.

In Section 5.5 I proposed my estimation approach, which is based on the fact that the transfer function of the system vehicle-ground presents a pole in zero, a negative pole and a negative zero. The negative pole and the negative zero are essential to extract the two independent parameters ηF_z and Λ_t. However, in Section 5.6 I have demonstrated how, under specific conditions, the system behaves very similarly to a transfer function with only one pole and no zeros. If this was the case, the estimation of ηF_z and Λ_t using the proposed approach would require a very high accuracy in the calculations, given that the contribution of the zero would be minimal. The critical conditions are $\left|\frac{\omega}{z_1}\right| \gg 1$ or $1 \gg \left|\frac{\omega}{z_1}\right|$, which leave a limited choice of modulation frequencies that are suitable for the proposed approach. By defining an acceptance factor k, which depends on the acceptable error in the estimation, a suitable modulation frequency has to be chosen between $-\frac{z_1}{2\pi k}$ and $-\frac{z_1 k}{2\pi}$. Figure 5.11 shows the acceptable range of modulation frequencies for the proposed simulation, which varies with the time, considering an acceptance factor of 3. It is important to notice that an acceptance factor of 1 does not guarantee an error-free estimation, because the errors in the estimation always depend on the limited representation of the values, on the resolution of the samples, on the number of samples per modulation period and, mostly importantly, on the measurement noise generated by the physical system. Potentially, any modulation frequency would allow a precise estimation, if only the calculation are executed with a sufficient degree of precision and the measurement noise is sufficiently low.

It is useful to summarise the constraints on the choice of the modulation frequency used for the proposed estimation algorithm, as follows:

- The modulation frequency should be as low as possible, in order to reduce the sensitivity of the calculation of p_1 and z_1 to the errors in the real and the imaginary part of the perceived transfer function.

- The modulation frequency should be as close as possible to the value $-\frac{z_1}{2\pi}$, in order to excite the system vehicle-ground at the frequency where the parameters of the transfer function are more observable.

- The modulation frequency should be as high as possible, in order to provide information about the operating point with minimal delay (the delay

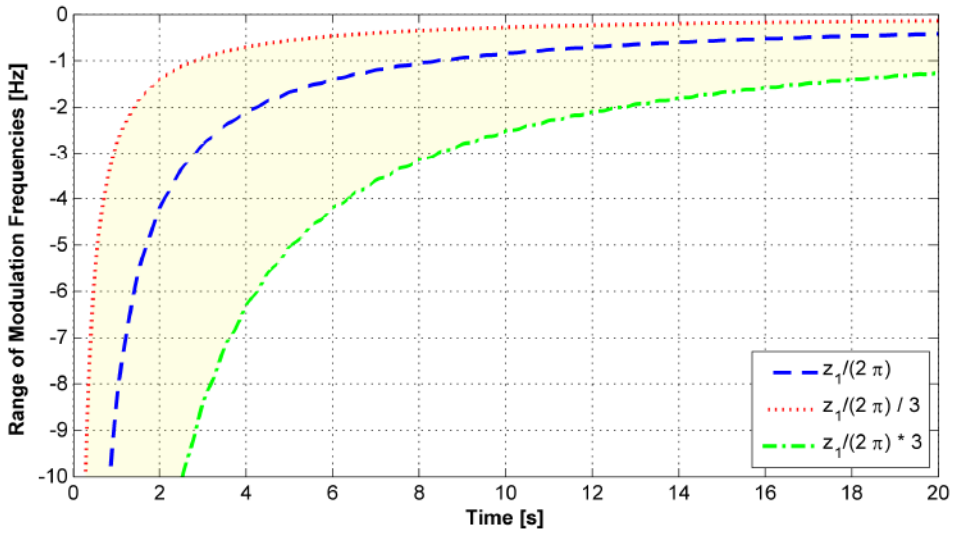

Figure 5.11: *Range of acceptable modulation frequencies, considering and acceptance factor of 3*

can be approximated with one or two modulation periods, depending on the desired accuracy in the estimation).

- The modulation frequency should be as high as possible, in order to complete a modulation period before allowing time for the operating point to change substantially. This would improve the performances of the proposed estimation algorithm during dynamic manoeuvres.

By looking at these constraints, it clearly appears that there is no such thing as an ideal frequency, but a compromise needs to be found based on the chosen computational unit, the operational point and the parameters of the system vehicle-ground. In order to validate the analysis carried over in this subsection, I will now present the results of the proposed simulation setup, while using different modulation frequencies: 0.5 Hz (the value corresponding to $-\frac{z_1}{2\pi}$ for high wheel-speed of the proposed simulation), 0.2 Hz (a value slightly lower, to see if the sensitivity of the calculation of p_1 and z_1 is more critical than the proximity to $\frac{z_1}{2\pi}$) and 10 Hz (to see the degradation in performance of the proposed algorithm at high frequencies).

5.7.3 Modulation Frequency of 0.5 Hz, 0.2 Hz and 10 Hz

In order to better compare the results of the simulation using different modulation frequencies, I decided to change the execution time of the proposed estimation algorithm to maintain a constant number of samples per execution period. It is in fact intuitive that computing the real and the imaginary part of the perceived transfer function (or, similarly, the gain and the phase shift

between the input and the output) using 5000 samples per modulation period for a modulation frequency of 0.2 Hz (corresponding to a sampling period of 1 ms) will provide better results than doing the same using 100 samples per modulation period for a modulation frequency of 10 Hz (always corresponding to a sampling period of 1 ms). It is less intuitive what will happen if the number of samples per modulation period is kept constant.

According to Figure 5.11, the modulation frequency that better highlights the contribution of all the parameters of the transfer function (the negative pole and the negative zero) is approximately 0.5 Hz. The results of the simulation, using a modulation frequency of 0.5 Hz and a sampling period of 4 ms (in order to have 500 samples per modulation period), are shown in Figures 5.12 and 5.13.

Figure 5.12 shows a lag of roughly 1 s between the estimation of p_1 and z_1 and their instantaneous value. This is to be expected because, as previously stated, the estimation algorithm computes all the measurements during the last modulation period (2 s for a modulation frequency of 0.5 Hz) and the output of the estimation is roughly an average of the expected output during that period. The estimation of p_1 and z_1 looks once again pretty accurate at this level of scale, although I have already discussed how minimal errors are sufficient to compromise the calculation of ηF_z and Λ_t.

Figure 5.13 shows the filtered (averaged in a modulation period) results of the calculation of ηF_z and Λ_t. The results shows a general improvement in the accuracy of the estimation, compared with the results obtained with a modulation frequency of 2 Hz and the same number of samples per period (see Figure 5.7). This proves that the errors in the estimation are reduced because the parameters of the transfer function are more observable (modulation frequency closer to $-\frac{z_1}{2\pi}$) and/or because the sensitivity of the calculation of p_1 and z_1 is reduced (lower modulation frequency). In order to determine which of these two is the most relevant factor, I will further reduce the modulation frequency, moving away from $-\frac{z_1}{2\pi}$. The results of the simulation, using a modulation frequency of 0.2 Hz and a sampling period of 10 ms (in order to have 500 samples per modulation period), are shown in Figures 5.14 and 5.15.

Figure 5.14 shows the estimation of p_1 and z_1. This is now lagging behind the instantaneous value of the parameters by approximately 2.5 s, which is consistent with the chosen modulation period of 5 s. Figure 5.15 shows a further improvement in the estimation of ηF_z and Λ_t, compared with the results obtained with a modulation frequency of 0.5 Hz and the same number of samples per period (see Figure 5.13). In particular, the estimation of the slip ratio Λ_t is more accurate for high values of the wheel speed, even considering that the lag of the estimation with 0.2 Hz is larger than the lag of the estimation

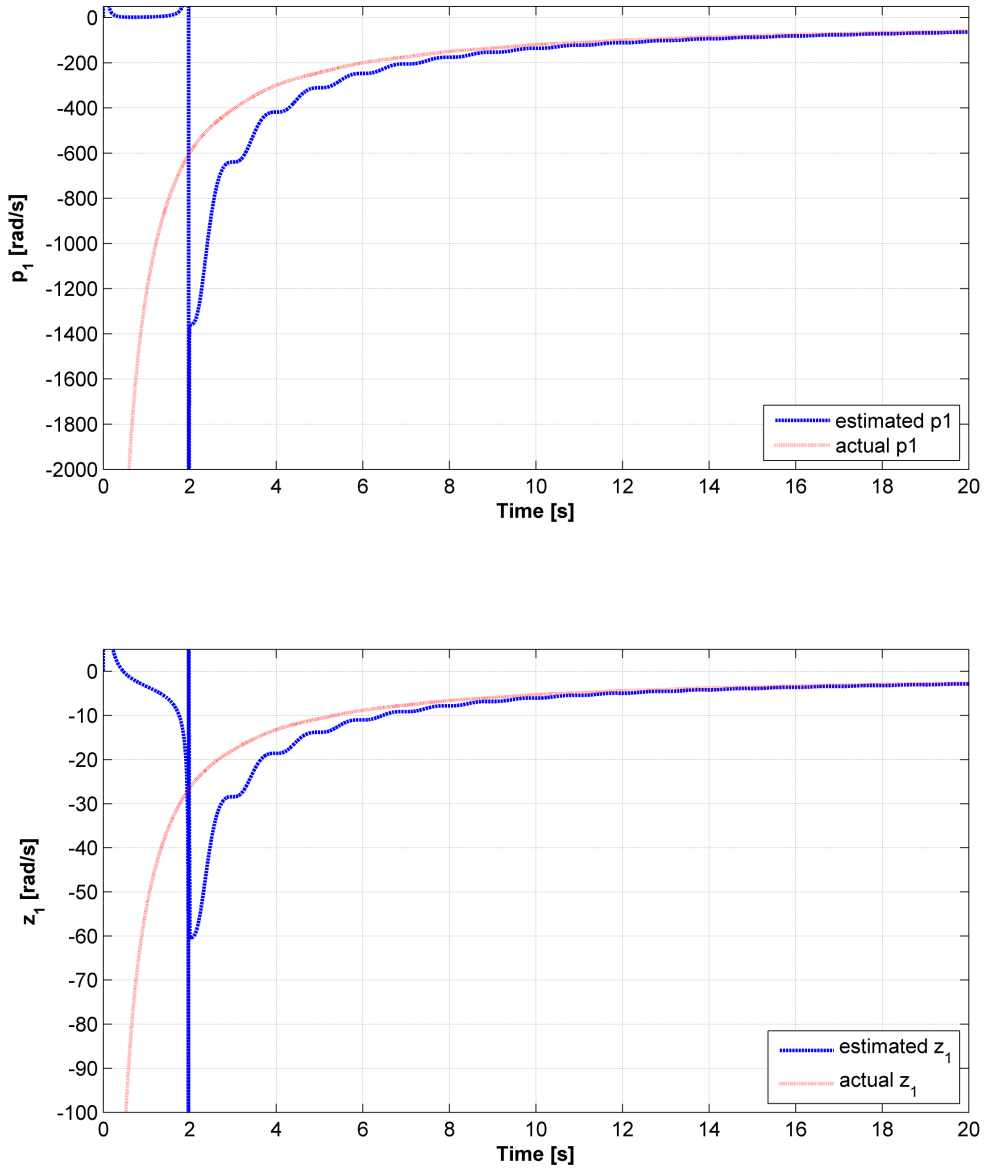

Figure 5.12: *Estimation of p_1 and z_1, using a modulation frequency of 0.5 Hz and a sampling period of 4 ms (500 samples per modulation period)*

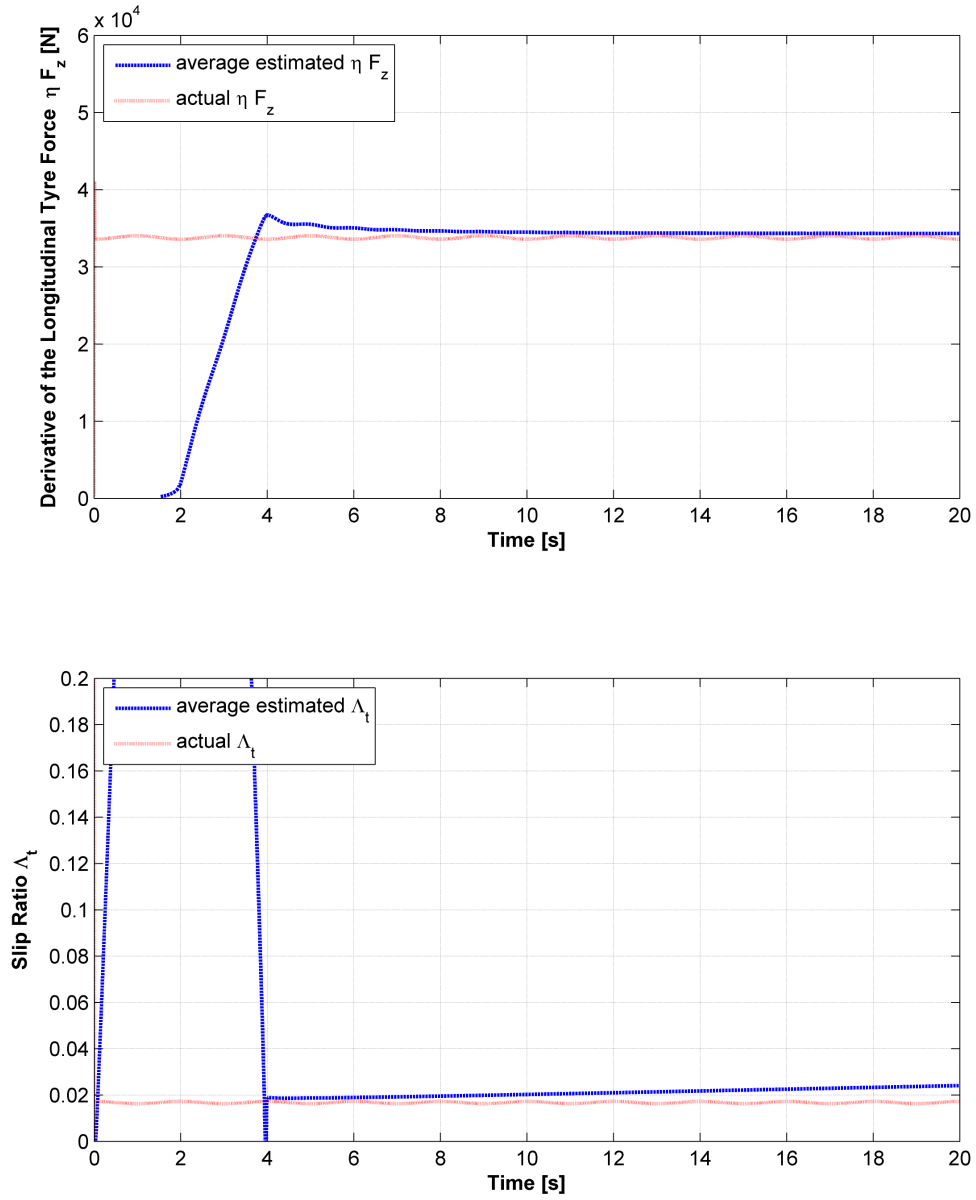

Figure 5.13: *Estimation of the derivative of the longitudinal tyre force ηF_z and the slip ratio Λ_t, averaged during a modulation period, using a modulation frequency of 0.5 Hz and a sampling period of 4 ms (500 samples per modulation period)*

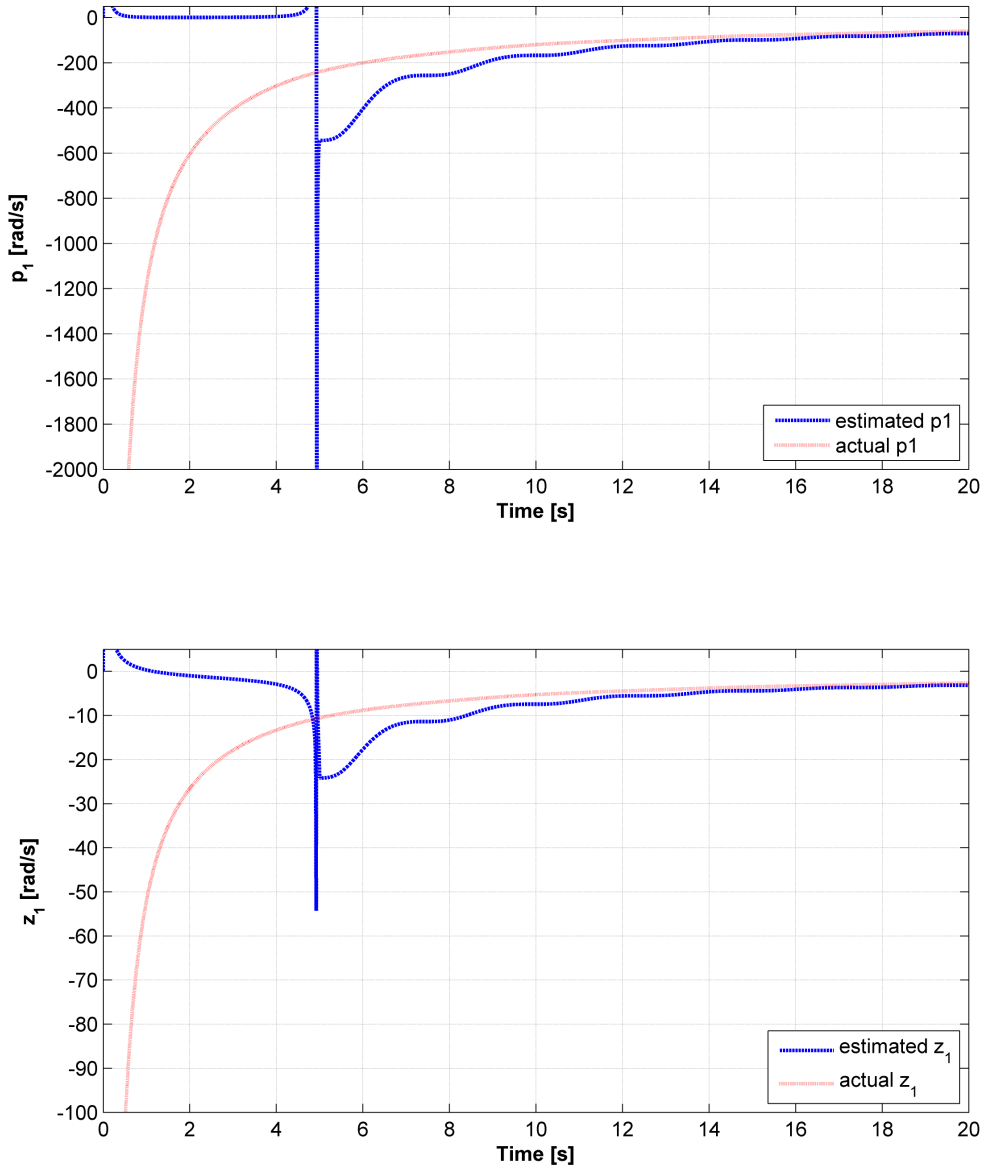

Figure 5.14: *Estimation of p_1 and z_1, using a modulation frequency of 0.2 Hz and a sampling period of 10 ms (500 samples per modulation period)*

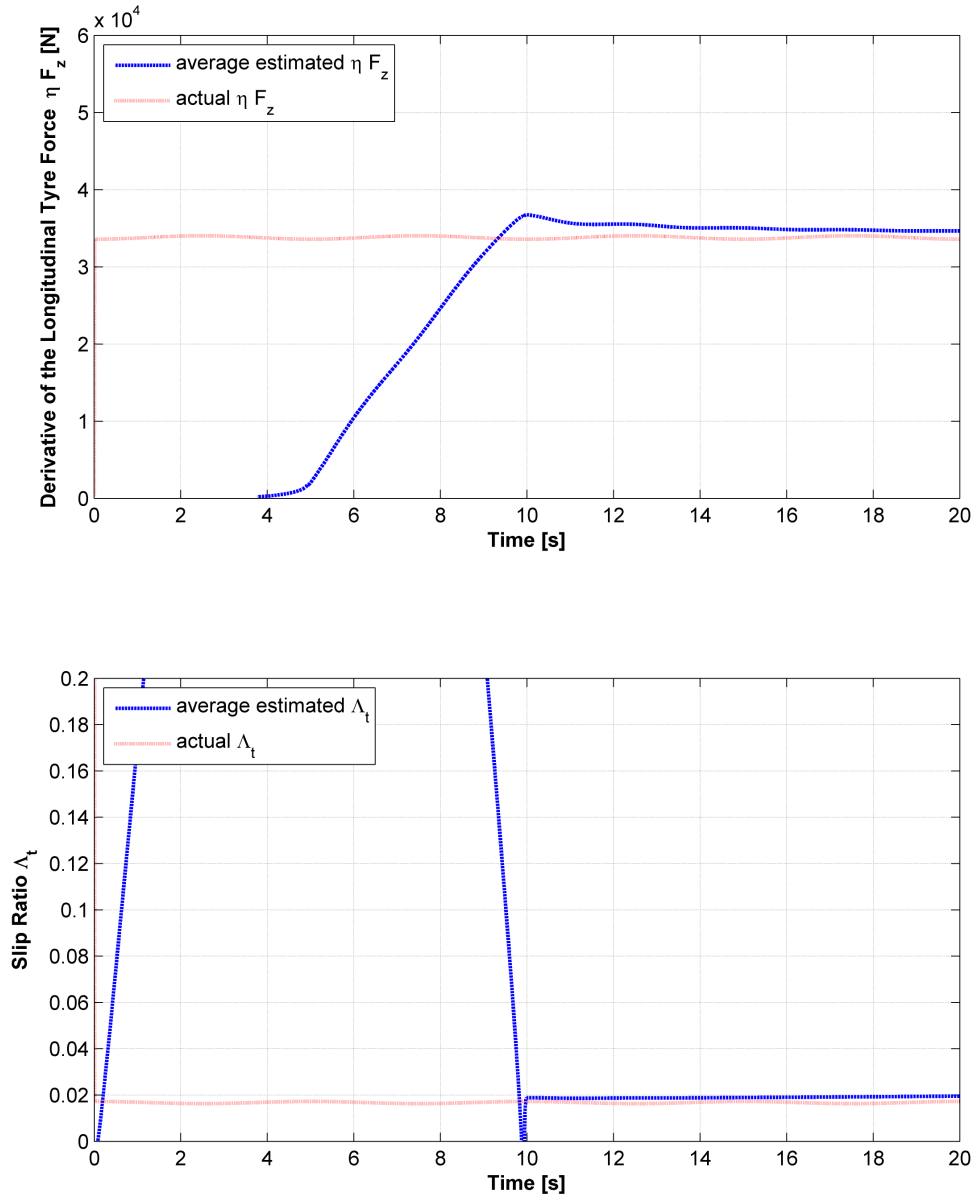

Figure 5.15: *Estimation of the derivative of the longitudinal tyre force ηF_z and the slip ratio Λ_t, averaged during a modulation period, using a modulation frequency of 0.2 Hz and a sampling period of 10 ms (500 samples per modulation period)*

with 0.5 Hz (therefore it is correct to compare the results of the estimation with 0.2 Hz at time 20 s with the results of the estimation with 0.5 Hz at time 14 s). This proves that using a modulation frequency slightly lower than $-\frac{z_1}{2\pi}$ does not compromise too much the observability of the parameters of the transfer function, but further reduces the sensitivity of the calculation of p_1 and z_1. This allows for an overall improvement of the estimation.

A modulation frequency of 0.2 Hz is not really practical for the proposed estimation, given that 5 s is a period too large to expect that the operating point would not move substantially during this time (the vehicle speed might vary; the throttle position, and so the torque applied, might vary; the ground conditions might vary). With this in mind, I decided not to present a simulation using an even lower modulation frequency. I believe this not to be necessary to prove that, by further lowering the modulation frequency, the accuracy of the proposed estimation will eventually deteriorate. It is in fact intuitive that, with a modulation frequency low enough, the motive force would vary so slowly that the system would effectively be in steady state. Under these conditions, the phase shift between the motive force and the wheel speed would basically be zero, and the only observable parameter would be the gain between the two oscillations. There is no mathematical operation that allows for an estimation of two parameters when only one parameter is observable; therefore the estimation of ηF_z and Λ_t would be impossible.

Instead of pushing the modulation frequency to extremely low values, I believe it is more interesting to show the results of a simulation using a more practical modulation frequency, such as 10 Hz. The results of this simulation, using a sampling period of 200 μs in order to have 500 samples per modulation period, are shown in Figures 5.16 and 5.17.

Figure 5.16 shows almost no lag between the estimation of p_1 and z_1 and their instantaneous value. Actually, there is a lag of roughly 0.1 s, as expected given the modulation frequency of 10 Hz. The estimation of p_1 and z_1 looks once again pretty accurate at this level of scale. As Figure 5.17 shows, however, there are substantial errors in the calculation of ηF_z and Λ_t, revealing that there are indeed errors in the estimation of p_1 and z_1. These errors are even larger than the ones resulting from using a modulation frequency of 2 Hz and a sampling period of 1 ms (as shown in Figure 5.8). While the estimation of ηF_z presents a relative error of roughly 14%, the estimation of Λ_t is completely off-target, with a relative error of more than 600%.

These results prove once again that choosing a modulation frequency significantly higher than the value $-\frac{z_1}{2\pi}$ increases the sensitivity of the proposed estimation to any error in the measurements. In this case, the errors in the

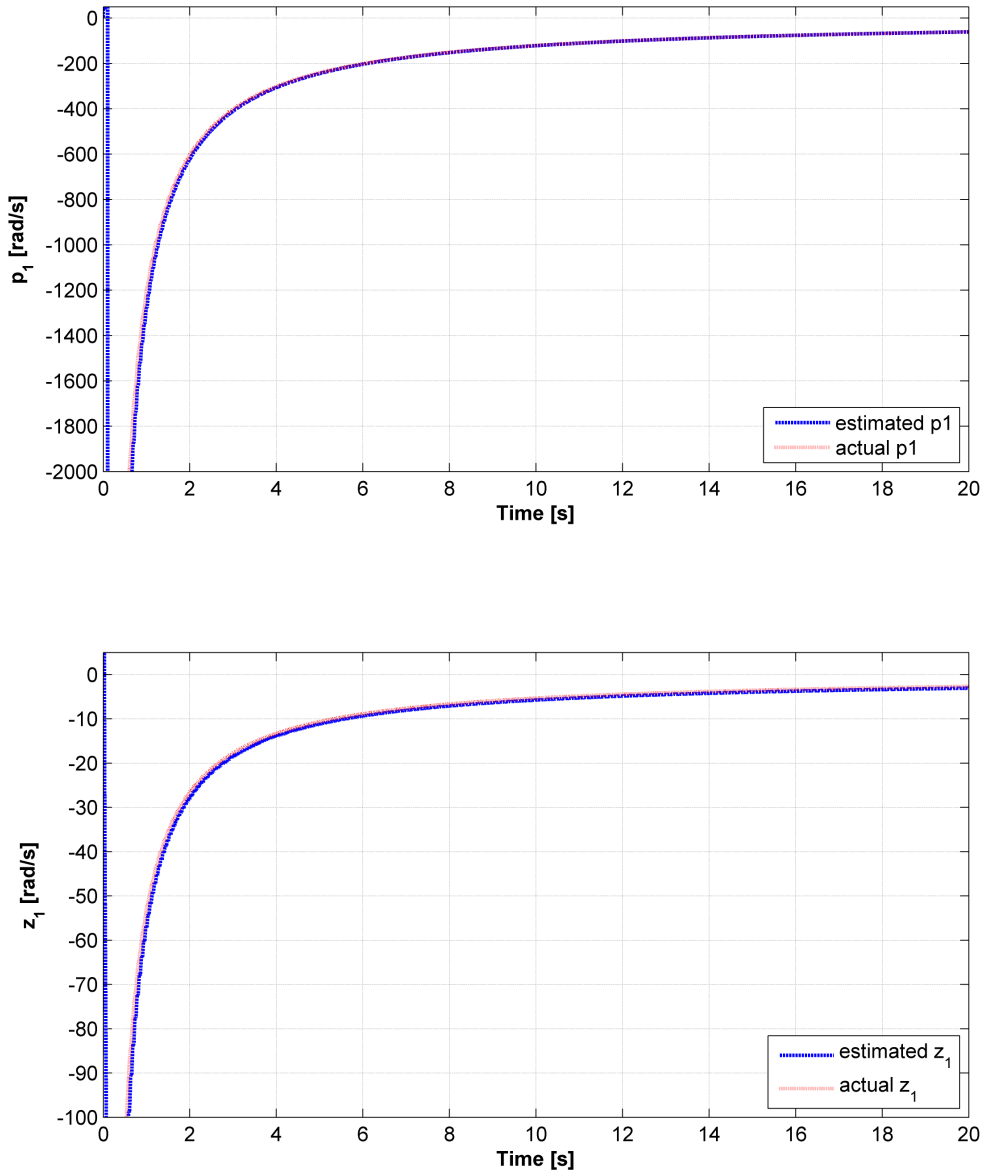

Figure 5.16: *Estimation of p_1 and z_1, using a modulation frequency of 10 Hz and a sampling period of 200 μs (500 samples per modulation period)*

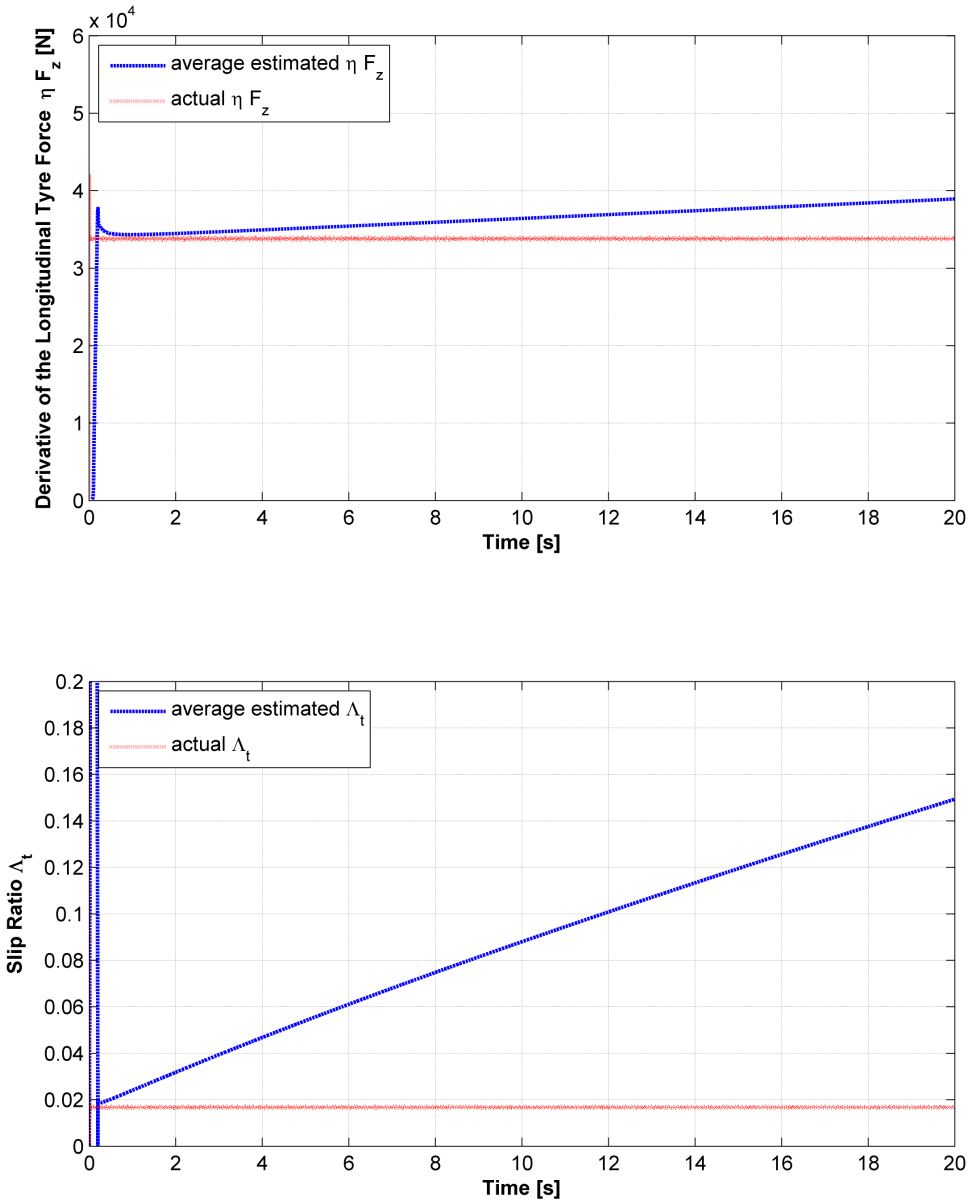

Figure 5.17: *Estimation of the derivative of the longitudinal tyre force ηF_z and the slip ratio Λ_t, averaged during a modulation period, using a modulation frequency of 10 Hz and a sampling period of 200 μs (500 samples per modulation period)*

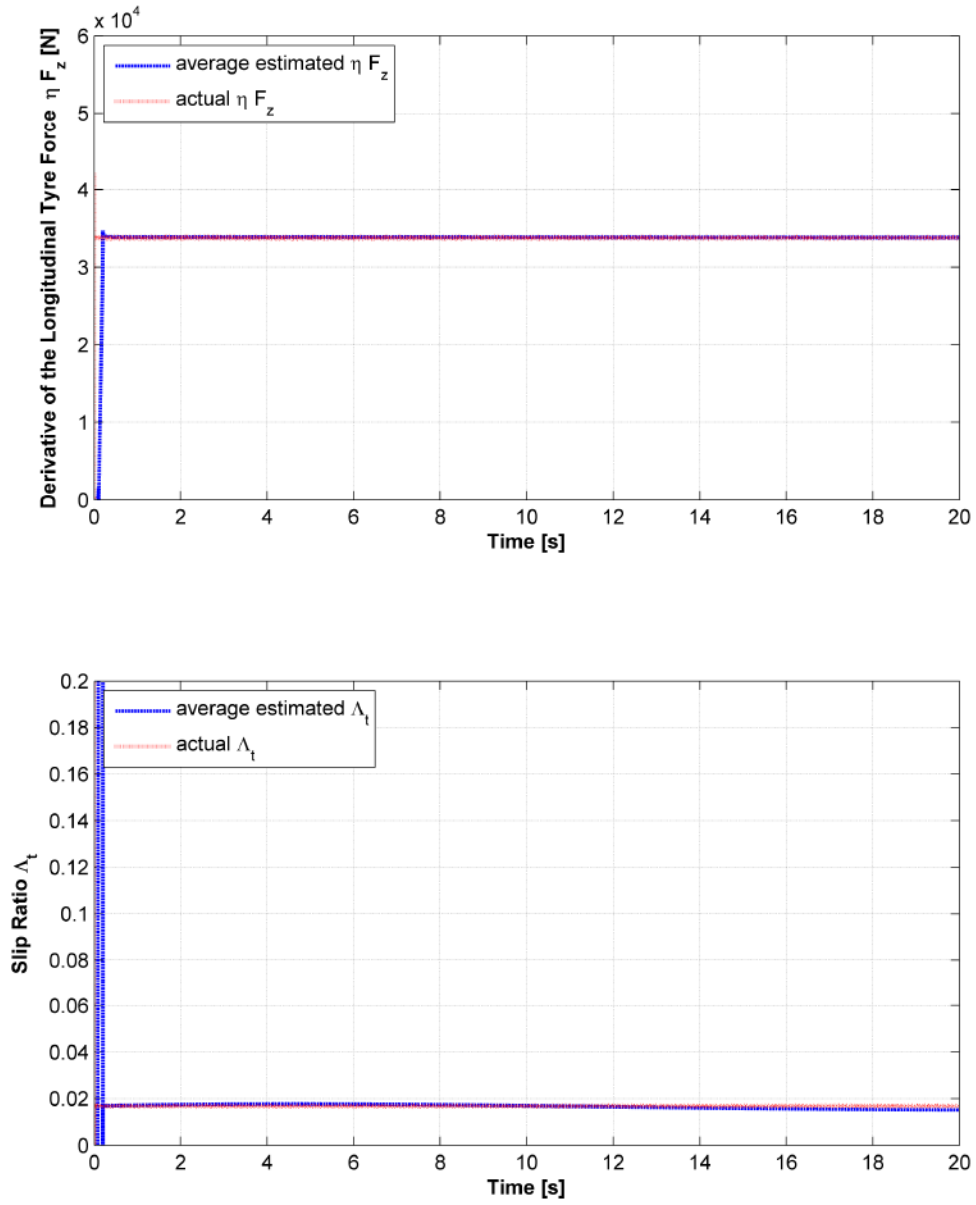

Figure 5.18: *Estimation of the derivative of the longitudinal tyre force ηF_z and the slip ratio Λ_t, averaged during a modulation period, using a modulation frequency of 10 Hz and a sampling period of 10 μs (10000 samples per modulation period)*

measurements are due to the sampling rate of the algorithm. In fact, by increasing the sampling rate from 500 samples to 10000 samples per modulation period, the problem is easily fixed. Figure 5.18 shows the filtered (averaged in a modulation period) results of the estimation of ηF_z and Λ_t, using a modulation frequency of 10 Hz and a sampling period of 10 μs (in order to have 10000 samples per modulation period). As anticipated, the results show a high level of accuracy.

5.8 Limitations of the Proposed Approach

The results of the simulation, presented in Section 5.7, proves that the theory behind the proposed estimation has solid mathematical basis. However, they also show a high sensitivity of the proposed approach to minimal errors in any step of the estimation (measurement and calculation). This is, in my view, the major obstacle towards a practical implementation in automotive environments, where measurement noise is an important factor to be considered. The best way to verify the practicality of the proposed approach would be to first test it on an over-specified electric vehicle, carefully designed to minimised electrical noise, with uniform tyre tread (slick tyres), using state-of-the-art electric motors (high resolution position sensor, negligible cogging torque) and motor controllers (very high PWM frequency - 20 kHz and above - to minimise torque ripple, potentially using an FPGA to minimise the execution period of the torque control and the proposed estimation algorithm - around 10 μs). If encouraging results are obtained, it would then be possible to downgrade the vehicle to use more ordinary (and less expensive) components.

The choice of the modulation frequency is another problem that needs to be carefully addressed for a robust implementation of the proposed algorithm. The results presented in Section 5.7 are encouraging in this regard, because they prove that the estimation of z_1 provides fundamental information about the dynamics of the system vehicle-ground at the current operating point, which can be used to select a suitable modulation frequency. In addition, the estimation of z_1 does not appear to be nearly as sensitive as the estimation of ηF_z and Λ_t to the errors in measurements and calculations. This suggests that a rough estimate of z_1 can be obtained by using a pre-defined modulation frequency. Based on the estimated z_1, the modulation frequency could then be tuned to a more suitable value, which in turn will improve the accuracy of the estimation. It would therefore be possible to establish a cyclic process where the latest value of the estimation of z_1 is always used to refine the current modulation frequency.

The proposed approach is based on the assumption that the friction characteristic between the tyre and the ground does not vary with the excitation frequency of the system. In reality, the friction characteristic is usually measured in steady-state conditions, and it could well vary considerably with the modulation frequency. This is surely true at very high frequency, where the variations in the tread (tread pattern) and in the ground (mineral aggregate in asphalt concrete) cannot be ignored. How this affects the proposed estimation approach has to be investigated.

Even if the proposed model of the vehicle-ground proves to be a reliable

model, the proposed estimation approach relies on two operational constraints:

- The operating point $(\Lambda_t, V_w, F_m, F_{ext}, F_x)$, which is the target of the estimation, should not vary considerably during a modulation period. This is the critical requirement that allows to approximate the system vehicle-ground with a linear system.
- The time derivative of the slip ratio should be, on average during a modulation period, equal to zero ($\dot{\Lambda}_t \approx 0$). This assumption was introduced in Section 5.5, in order to simplify the transfer function of the system vehicle-ground.

The results presented in Section 5.7 prove already that the proposed estimation algorithm is fairly robust against changes in the wheel speed V_w (in the simulation, the vehicle is under constant acceleration), with the estimation returning an operating point which is roughly the average of the operating points during a modulation period. This variation in the wheel speed does not compromise the estimation of ηF_z and Λ_t, which in the simulation are constant for every operating point. The second constraint ($\dot{\Lambda}_t \approx 0$) is a stronger requirement than the small variation of the operating point. If the slip ratio varies during a modulation period, the estimation will produce an error in the calculations (due to the fact that the formulas derived in Section 5.5 are based on the assumption that $\dot{\Lambda}_t \neq 0$) that adds to the error due to the non-linearity of the system (when $\dot{\Lambda}_t \neq 0$, the operating point is moving). Because the variation of the slip ratio can be caused by measurable variables (the motive force F_m) as well as unmeasurable variables (the external force F_{ext} or the longitudinal tyre force F_x, which is dependent on the ground conditions), it is not possible to avoid the situations in which the proposed estimation will not produce reliable results. Nonetheless, it is necessary to detect these situations, in order to be able to ignore the results of the estimation. A possible solution would be to monitor the total harmonic distortion of the system. In fact, in systems that are perfectly linear, any sinusoidal input produces a purely sinusoidal output at the same frequency (the phase and the amplitude might vary, depending on the transfer function), without generating content at other spectral frequencies. This means that the more the oscillation in the wheel speed is close to a pure sinusoid, the more the system vehicle-ground behaves as a linear system, the less the operating point is moving (including the slip ratio) and the more reliable the results of the proposed estimation algorithm would be.

5.9 Summary

Exploiting the characteristics of the electric motors, it has been shown how a simple motor controller can obtain information about the environment without

requiring additional hardware, simply analysing the motor response. A novel method to estimate both the slip ratio and the derivative of the longitudinal tyre force with respect to the slip ratio has been proposed. These parameters are needed to characterise appropriately the road surface, to detect the approaching of the maximum longitudinal tyre force and to control the slip ratio at the optimal value, improving the performance during acceleration and deceleration of the vehicle. In addition, the knowledge of the grip offered by the road can be integrated with other information, for example the distance to the preceding vehicle or the direction of the road, to assist the driver in avoiding dangerous situation.

Although cheap to implement and robust against changes in the external force, the proposed method presents some characteristics which require further investigation. In particular, the sensitivity to the noise in the measurements and the uncertainty in the parameters of the model needs to be analysed. The method has to be validated on a real vehicle in order to evaluate the limitations in the practical implementation. Finally, while the proposed method has been designed for autonomous vehicles, it would be useful to study how the vibrations generated by the cosinusoidal signal of torque would affect the comfort of passengers. This was not the focus of this thesis and it could be the subject of future work.

Chapter 6

Conclusions

6.1 The Experience

This thesis summarises all my experiences as PhD student. It reveals my personal development through a mixture of literature review, practical considerations, software and hardware design, mathematical modelling and proposition of novel approaches. The most important topic presented is the estimation of the grip with the ground, using only information that is typically available to the vehicle supervisory unit. Because my approach relies on the knowledge of the torque applied to the driven wheels, it is particularly focused on electric vehicles. I have presented a general framework to estimate the grip with the ground, so that anyone interested in this topic could use my thesis as a starting point, to develop techniques that are not necessarily related to the proposed approach. For completeness, I have tried to cover all the aspects of this topic, acknowledging when some of them could not be covered exhaustively. I did my best to clearly state the limitations of my design and my approach, the gaps in my review, and I have never spared suggestions for future investigations and developments. I would obviously have liked to do more, in order to validate the whole framework, but I had to respect the time constraint of a PhD project. My wish is that some people could resume my work where I have left it, and so I hope with this thesis to have managed to write down all the information in my possession that could encourage and facilitate their task.

The thesis starts by introducing the ITS project, that provided the objectives and the funding for my PhD (see Chapter 1). The aim of the ITS project is to train PhD students around the development of an autonomous electric vehicle. My contribution was crucial to the project, as I had to do all the work involved with making the vehicle go, be steerable, and be able to carry the vision equipment to be used by others. As result I have developed useful skills in dealing with design, component integration, project management, time and cost constraints. Such an exciting project provided me with the motivation needed to push the development of the vehicle. Starting from an electronic background, I became interested in computer vision and vehicle dynamics, mostly because of the regular discussions with my colleagues. The clear target of the project helped in maintaining the focus of my research on practical problems and realistic implementations. I believe my contribution has been determinant to the project in a very tangible way. The quad bike

is currently ready to be controlled from a remote server, as requested by the computer vision group. It also offers all the performances needed to test my approach to the grip estimation. Given what I started with (discussed in Chapter 4), I consider my experience quite successful and I am really satisfied with the overall outcome.

6.2 The Content

The main focus of this thesis is the estimation of the grip between the tyre and the ground, using information normally available in a production electric vehicle. The focus on electric vehicles is important because it implies the knowledge of the torque applied to every wheel (see Chapter 1). I presented an extensive review of the relevant publications, clearly identifying the gap that my research would cover. In order to provide the basic theory behind the grip between the tyre and the ground, I reviewed the most influential sources in the field of tyre mechanics (see Chapter 2). From this review, a strong similarity emerged between the longitudinal and the lateral mechanics of the tyre. In addition, I provided evidence of the close relationship between the generated longitudinal tyre force and the normal force applied to the ground. While my research focuses on the estimation of the longitudinal tyre force, I have briefly summarised all the considerations that I addressed over the years to the estimation of the normal force (see Chapter 3).

I proposed a novel technique to estimate the longitudinal tyre force (see Chapter 5), which does not require any hardware in addition to a standard motor controller with in-built current sensor. This is included in the basic hardware for any production electric vehicle. Unlike most of the previous research, my novel approach provides a continuous estimation of the longitudinal tyre force, which allows the detection of changes in the road condition. This approach is not sensitive to slow changing forces such as the gravitational force or the aerodynamic drag, nor it is particularly sensitive to high frequency noise, given that it focuses on the behaviour of the vehicle around a specific frequency. While most of the previous research provides better results in highly dynamic conditions, such as braking and strong accelerations, my approach provides better results in steady state. This is because it relies on the assumption $\dot{\Lambda}_t \approx 0$ made in Section 5.5. The ideal application of the technique proposed in this thesis would be the continuous monitoring of the road condition during smooth driving. Because of traffic and road regulations, smooth driving is much more common than aggressive driving, and my approach would cover a large number of driving scenarios (notably the high speed driving typical of motorways).

In addition to the achievements relating to the estimation of the grip with the ground, I provided an insight into the development of a vehicle, carried out by me for the ITS project (see Chapter 4). The aim was to build a vehicle to be used as a platform to test my techniques of grip estimation, together with the techniques of visual localisation, path planning and dynamic control that were developed by my colleagues. I have successfully delivered a vehicle capable of all this, although the various techniques have not been tested so far, mainly because I was the first PhD student to start on the project, and the others who will use the vehicle are following behind. In this thesis I discussed the design, the choice of components, the challenges faced, the performances offered as well as the limitations of the system. This information is essential for my colleagues who will need to carry on from where I left. Moreover, it will be very useful for anyone interested in developing a similar vehicle. In the context of my thesis, the whole development of the vehicle was focused on the delivery of capabilities for the estimation of the grip with the ground. I provide an insight into the practical challenges for the implementation of the proposed techniques, suggesting the sensors to use as well as suitable approximations to adopt (such as using the motor current to approximate the motor torque).

6.3 Future Work

During the whole thesis I have suggested further developments to my work. In this section I will try to summarise the most important ones. The most relevant to my research is surely the experimental validation of the proposed estimation of the grip with the ground. As extensively discussed, I have developed a vehicle with this purpose; however, the development took so long that I have been unable to validate the proposed approach during my PhD. One of the main objectives of my thesis was to gather all the information needed for someone else to carry on with the validation, using the vehicle that I developed. On this topic, the remaining tasks that need to be tackled are:

- The proposed algorithm has to be coded to be executed on the motor controller on the vehicle (the CompactRIO).
- The two traction motors have to be instrumented with a torque sensor on a test bench, in order to calibrate the conversion between motor current and motor torque.
- The vehicle has to be instrumented with speed sensors on the rear wheels, in order to calibrate the estimation of the wheel speed at different operating conditions (the estimation has only been calibrated with the vehicle lifted from the ground, at steady state and with very low torque applied).

- The mechanical parameters of the vehicle have to be measured. In particular, it is essential to evaluate the mass distribution of the vehicle, the moment of inertia of each wheel together with the moment of inertia of the rotor in the traction motor connected to it.

- The experimental environment needs to be prepared. First of all, a suitable area for the test has to be identified. This area should be at least the size of 4 by 1.5 m and it should be flat, in order to remove the need for a continuous estimation of the normal force. Ideally, a wooden board should be used as ground surface, because it would guarantee the uniformity of friction coefficient. In addition, the wooden board could be polished or painted to reduce the friction, in order to allow the vehicle to reach a wide range of values of slip ratio (possibly skidding), despite the low torque available.

- The coefficient of friction between the surface chosen for the test and the tyres of the vehicle has to be measured using a technique that is as different as possible (not relying on the same assumptions) to the proposed estimation technique. A possible solution would be to lock two wheels of the vehicle and to drag the vehicle over the chosen surface by using an electric hoist, while measuring the force applied by the electric hoist through a force gauge. The electric hoist would allow to keep a constant speed and the speed could be varied by changing the voltage provided to the electric hoist (within the allowed limits). However, an electric hoist with a suitable speed range has to be first identified.

- The speed of the vehicle has to be measured using a technique that does not rely on the estimation of the slip ratio, but that is accurate enough to allow for the calculation of the slip ratio, given the measurement of the wheel speed. A possible solution would be to use a laser rangefinder, pointed at the front of the vehicle.

In my opinion these steps, together with the analysis of the experimental results, could easily take another year or much longer, depending on the quality targets.

The analysis of a suitable technique for the estimation of the normal force is a required step to present an effective estimation of the ground grip in all driving conditions (particularly off-road). In Chapter 3 I proposed some solutions, but they all need further investigation and validation. A major objective would be to integrate the estimation of the normal force with the estimation of the longitudinal tyre force, to cover driving scenarios when longitudinal and vertical dynamics are tightly coupled (in general, whenever the wheels hit an

obstacle the vehicle slows down longitudinally but this is only critical when large obstacles are in the way).

I have previously highlighted the similarities between longitudinal and lateral mechanics of the tyres (see Chapter 2). I believe that the same approach proposed in this thesis about the estimation of the longitudinal friction between the tyre and the ground can be extended to estimate the lateral friction between the two. This research area is largely unexplored, however it could lead to a great improvement in the lateral stability of the vehicle. A related work would be to analyse the longitudinal friction characteristic and the lateral friction characteristic for several kinds of surfaces and tyres, in order to establish if it is possible to infer the loss of friction in one direction from the loss of friction in another direction and, if it is, to quantify it.

In the context of autonomous guidance, a future development would be to correlate the information of the ground grip with the appearance of the road. Most of the autonomous vehicles use cameras to understand the environment surrounding them. The visual information could be integrated with the results of the proposed estimation technique, which provides continuous feedback about the grip with the ground, in order to learn the grip offered by a surface based on its appearance. This implementation would allow forecasting of the changes in grip as far as the field of view of the camera goes. Optimal trajectories could then be calculated in order to give, at one and the same time, the best possible performance and safety.

References

A123 Website. URL: http://www.a123systems.com (visited on 02/01/2013).

Akiba, Toru et al. (2007). "A Study of Novel Traction Control Method for Electric Motor Driven Vehicle". In: *Power Conversion Conference (PCC)* 6, pp. 699–704.

Alvarez, Luis (1999). "Adaptive emergency braking control in automated highway systems". In: *38th IEEE Conference on Decision and Control*. December. IEEE, pp. 3740–3745.

Bolton, William (1998). *Control engineering*. Longman, p. 397.

Bose, B.K. (Dec. 1997). *Power electronics and variable frequency drives: technology and applications*. 8. IEEE, pp. 903–908.

Canudas De Wit, Carlos and Roberto Horowitz (1999). "Observers for Tire/road Contact Friction using only wheel angular velocity information". In: *38th Conference on Decision and Control*. December, pp. 3932–3937.

Canudas De Wit, Carlos and Panagiotis Tsiotras (1999). "Dynamic Tire Friction Models for Vehicle Traction Control". In: *38th Conference on Decision and Control*. December, pp. 3746–3751.

Cecotti, Marco, James Larminie, and Brian Azzopardi (2012). "Estimation of Slip Ratio and Road Characteristics by Adding Perturbation to the Input Torque". In: *IEEE International Conference on Vehicular Electronics and Safety (ICVES)*, pp. 31 –36.

Chan, C C and Y S Wong (2004). "The State of the Art of Electric Vehicles Technology". In: *International Power Electronics and Motion Control Conference (IPEMC)*, pp. 46–57.

Chen, Yan and Junmin Wang (Mar. 2011). "Adaptive Vehicle Speed Control With Input Injections for Longitudinal Motion Independent Road Frictional Condition Estimation". In: *IEEE Transactions on Vehicular Technology* 60.3, pp. 839–848.

Chenglin, Liao et al. (2009). "Modeling and Simulation of Traction Control of Hybrid Electric Vehicle". In: *International Conference on Mechatronics and Automation (ICMA)* I, pp. 3252–3256.

Craig, John J. (2008). *Introduction to Robotics: Mechanics and Control*. 3rd ed. Prentice Hall, p. 408.

Dahl, P R (1968). *A Solid Friction Model*. Tech. rep. Space and Missile System Organization.

DARPA Grand Challenge Website. URL: http://www.darpa.mil/grandchallenge/index.asp (visited on 02/10/2010).

Delli Colli, Vincenzo, Giovanni Tomassi, and Maurizio Scarano (May 2006). "" Single Wheel " Longitudinal Traction Control for Electric Vehicles". In: *IEEE Transactions on Power Electronics* 21.3, pp. 799–808.

Dow Kokam Batteries Website. URL: `http://www.dowkokam.com` (visited on 02/01/2013).

Duleep, Gopalakrishnan et al. (2011). *Impacts of Electric Vehicles - Assessment of electric vehicle and battery technology*. Tech. rep. April. European Commission.

Ehsani, Mehrdad, Yimin Gao, and Ali Emadi (2009). *Modern Electric, Hybrid Electric, and Fuel Cell Vehicles: Fundamentals, Theory, and Design*. 2nd ed. CRC Press, p. 557.

Ervin, Robert D., Charles C. Macadam, and Paul S. Fancher (1975). *The Longitudinal Traction Characteristics of Truck Tires as Measured on Dry Pavements*. Tech. rep. February. Highway Safety Research Institute.

Fancher, P. S. et al. (1970). *Experimental Studies of Tire Shear Force Mechanics*. Tech. rep. Highway Safety Research Institute.

Foito, Daniel, Manuel Guerreiro, and Armando Cordeiro (2008). "Anti-Slip Wheel Controller Drive for EV using Speed and Torque Observers". In: *18th International Conference on Electrical Machines (ICEM)*, pp. 1–5.

Fonda, Albert G (Jan. 1956). "Tyre Tests and Interpretation of Experimental Data". In: *Institution of Mechanical Engineers: Automobile Division*.

Fujimoto, Hiroshi, Kiyoshi Fujii, and Naoki Takahashi (2007). "Vehicle Stability Control of Electric Vehicle with Slip-ratio and Cornering Stiffness Estimation". In: *IEEE International Conference on Advanced Intelligent Mechatronics* 1, pp. 1 –6.

Fujimoto, Hiroshi et al. (2004). "Motion Control and Road Condition Estimation of Electric Vehicles with Two In-wheel Motors". In: *IEEE International Conference on Control Applications* 2, pp. 1266 –1271.

Furukawa, Kimihisa and Yoichi Hori (2003). "Recent Development of Road Condition Estimation Techniques for Electric Vehicle and their Experimental Evaluation using the Test EV "UOT March and I and II"". In: *29th Annual Conference of the IEEE Industrial Electronics Society (IECON)*. 2. IEEE, pp. 925 –930.

Germann, S, M Wurtenberger, and A Daiss (1994). "Monitoring of the friction coefficient between tyre and road surface". In: *Third IEEE Conference on Control Applications*. Vol. 0, pp. 613–618.

GM Powertrain Website. URL: `http://gmpowertrain.com` (visited on 02/01/2013).

Grahn, Pia and Lennart Söder (2011). "The Customer Perspective of the Electric Vehicles Role on the Electricity Market". In: *8th International Conference on the European Energy Market (EEM)*. May, pp. 141–148.

Grünig, Max et al. (2011). *Impacts of Electric Vehicles - Assessment of the future electricity sector*. Tech. rep. European Commission.

Gustafsson, Fredrik (1998). "Monitoring Tire-Road Friction Using The Wheel Slip". In: *IEEE Control System Magazine*, pp. 42–49.

Hall, Jim and David E Davis (Apr. 1965). "What Makes Cars Handle ?" In: *Car & Driver* April.

Hallowell, Stephen J and Laura R Ray (2003). "All Wheel Driving Using Independent Torque Control of Each Wheel". In: *Proceedings Of The American Control Conference*, pp. 0–5.

Hodkinson, Ron and John Fenton (2001). *Lightweight Electric/Hybrid Vehicle Design*. Butterworth-Heinemann Ltd.

Hori, Yoichi (Oct. 2004). "Future Vehicle Driven by Electricity and Control - Research on Four-Wheel-Motored". In: *IEEE Transactions on Industrial Electronics* 51.5, pp. 954–962.

Hori, Yoichi, Yasushi Toyoda, and Yoshimasa Tsuruoka (Sept. 1998). "Traction Control of Electric Vehicle : Basic Experimental Results Using the Test EV "UOT Electric March"". In: *IEEE Transactions on Industry Applications* 34.5, pp. 1131–1138.

Howell, David (2012). "Plenary : Battery R & D Activities". In: *DOE Vehicle Technologies Program Annual Merit Review*.

Husain, Iqbal (2010). *Electric and Hybrid Vehicles: Design Fundamentals*. CRC Press, p. 501.

Jalili-kharaajoo, Mahdi and Farhad Besharati (2003). "Sliding Mode Traction Control of an Electric Vehicle with Four Separate Wheel Drives". In: *IEEE Conference on Emerging Technologies and Factory Automation (ETFA)*, pp. 1–6.

Khan, Iftikhar (2006). "Emerging Technologies in Automobiles". In: *International Conference on Emerging Technologies* November, pp. 368–377.

Khatun, P et al. (2003). "Application of Fuzzy Control Algorithms for Electric Vehicle Antilock Braking / Traction Control Systems". In: *IEEE Transactions on Vehicular Technology* 52.5, pp. 1356–1364.

Koehn, Philip and Michael Eckrich (2004). "Active Steering - The BMW Approach Towards Modern Steering Technology". In: *SAE World Congress*. Vol. 2004. 724. SAE International.

Larminie, James and John Lowry (2003). *Electric Vehicle Technology Explained*. Wiley, p. 296.

Li, L., F.Y. Wang, and Q. Zhou (Mar. 2006). "Integrated Longitudinal and Lateral Tire/Road Friction Modeling and Monitoring for Vehicle Motion Control". In: *IEEE Transactions on Intelligent Transportation Systems* 7.1, pp. 1–19.

Liu, Chia-Shang and Huei Peng (Jan. 1996). "Road Friction Coefficient Estimation For Vehicle Path Prediction". In: *Vehicle System Dynamics* 25, pp. 413–425.

Liu, Xiaoxing et al. (2005). "Optimal Traction Control for EV utilizing Fast Torque Response of Electric Motor". In: *31st Annual Conference of IEEE Industrial Electronics Society (IECON)*, p. 6.

Milliken, W. F. and D. L. Milliken (1995). *Race car vehicle dynamics*. Society of Automotive Engineers, Warrendale, Pa., p. 918.

Müller, Steffen, Michael Uchanski, and Karl Hedrick (2003). "Estimation of the Maximum Tire-Road Friction Coefficient". In: *Journal of Dynamic Systems, Measurement and Control* 125.4, p. 607.

National Highway Traffic Safety Administration (1981). *Mechanics of Pneumatic Tires*. Ed. by Samuel Kelly Clark. U.S. Government Printing Office, p. 931.

Nishira, Hikaru, Taketoshi Kawabet, and Seiichi Shin (1999). "Road Friction Estimation Using Adaptive Observer with Periodical sigma-modification". In: *IEEE International Conference on Control Applications*, pp. 662–667.

Norton, Robert (Jan. 2008). *Design of Machinery: An Introduction to the Synthesis and Analysis of Mechanisms and Machines*. McGraw-Hill Higher Education, p. 825.

Oxford Brookes ITS Website. URL: `http://tech.brookes.ac.uk/research/intelligent-transport-systems` (visited on 02/10/2010).

Pacejka, Hans B (2005). *Tire and Vehicle Dynamics, 2nd edition*. Vol. 2. 1940. SAE International, p. 642.

Peng, Xu et al. (2009). "Anti-slip Regulation of Electric Vehicle Without Speed Sensor". In: *IEEE International Symposium on Industrial Electronics (ISIE)* ISlE, pp. 222–227.

Pusca, Remus et al. (2002). "Modeling and Simulation of a Traction Control Algorithm for an Electric Vehicle with Four Separate Wheel Drives". In: *IEEE 56th Vehicular Technology Conference (VTC)*, pp. 1671–1675.

Ray, Laura R (Mar. 1995). "Nonlinear state and tire force estimation for advanced vehicle control". In: *IEEE Transactions on Control Systems Technology* 3.1, pp. 117 –124.

Sado, Hideo, Shinichiro Sakai, and Yoichi Hori (1999). "Road Condition Estimation for Traction Control in Electric Vehicle". In: *IEEE International Symposium on Industrial Electronics (ISIE)* 2, pp. 973–978.

Sakai, H. (1981). "Theoretical and experimental studies on the dynamic properties of tires". In: *International Journal of Vehicle Design* 2.1.

Sakai, Shinichiro, Hideo Sado, and Yoichi Hori (Mar. 1999). "Motion Control in an Electric Vehicle with Four Independently Driven In-Wheel Motors". In: *IEEE Transactions on Mechatronics* 4.1, pp. 9–16.

Savaresi, Sergio M. and Mara Tanelli (2010). *Active Braking Control Systems Design for Vehicles*. Springer, p. 256.

Shino, Motoki et al. (2000). "Traction Control of Electric Vehicles Considering Vehicle Stability". In: *6th International Workshop on Advanced Motion Control*, pp. 311–316.

Shuang, Gao et al. (2007). "Skid Steering in 4 Wheel Drive Electric Vehicle". In: *7th International Conference on Power Electronics and Drive Systems (PEDS)*, pp. 1548–1553.

Spong, Mark W., Seth Hutchinson, and M. Vidyasagar (2005). *Robot Modeling and Control*. 1st ed. Wiley, p. 496.

Sweeting, W. J., a. R. Hutchinson, and S. D. Savage (Sept. 2011). "Factors affecting electric vehicle energy consumption". In: *International Journal of Sustainable Engineering* 4.3, pp. 192–201.

Thomas, George (2000). "Overview of Storage Development DOE Hydrogen Program". In: *DOE Hydrogen Program Annual Review*.

US EPA Fuel Economy Ratings. URL: `http://www.fueleconomy.gov` (visited on 02/01/2013).

Vehicle Dynamics Standards Committee (2008). *Vehicle Dynamics Terminology*. Tech. rep. SAE International, p. 73.

Wansart, Joerg and Eckehard Schnieder (Apr. 2010). "Modeling market development of electric vehicles". In: *IEEE International Systems Conference*. IEEE, pp. 371–376.

Wong, Jo Yung (2008). *Theory of ground vehicles*. John Wiley and Sons, p. 560.

Wu, Fengjiang et al. (2006). "Suppression of Gate Oscillation of Power MOSFET with Bridge Topology". In: *6th World Congress on Intelligent Control and Automation*. Ieee, pp. 8196–8200.

YASA Motors Website. URL: `http://www.yasamotors.com/` (visited on 02/01/2013).

Yin, Dejun, Sehoon Oh, and Yoichi Hori (June 2009). "A Novel Traction Control for EV Based on Maximum Transmissible Torque Estimation". In: *IEEE Transactions on Industrial Electronics* 56.6, pp. 2086–2094.

Zhang, Jianlong, Chengliang Yin, and Jianwu Zhang (2006). "Use of Fuzzy Controller for Hybrid Traction Control System in Hybrid Electric Vehicles". In: *IEEE International Conference on Mechatronics and Automation*, pp. 1351–1356.

Index